

Supporting Information for

**Tuning the Diiron Core Geometry in Carboxylate-Bridged Macrocyclic Model Complexes
Affects their Redox Properties and Supports Oxidation Chemistry**

*Fang Wang[†], Sabine Becker[†], Mikael A. Minier[†], Andrei Loas[†], Megan N. Jackson[†], and Stephen
J. Lippard^{*†}*

[†]Department of Chemistry, Massachusetts Institute of Technology, Cambridge, Massachusetts
02139, United States

1. Materials and Methods.

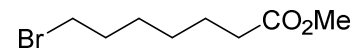
General. Reagents were purchased from commercial sources and used as received. Solvents were saturated with argon, purified by the passage through two columns of activated alumina, and stored over 3 Å molecular sieves inside an MBraun dry box. Reaction mixtures were monitored by thin-layer chromatography (TLC) on pre-coated, aluminum-backed silica gel 60 F254 plates. Column chromatography was performed in all cases on silica gel 60 (230-400 mesh). $\text{H}_2\text{F}_2\text{PIM}$,¹ 2-benzhydrylbenzoic acid,² 2-allylbenzaldehyde,³ and $[\text{Fe}_2(\text{Mes})_4]$ (Mes = 2,4,6-trimethylphenyl)⁴ were prepared according to published procedures. 4-Nitrophenylboronic acid pinacol ester was purchased from commercial sources or synthesized according to a published procedure.⁵ All manipulations of air sensitive compounds were performed in an MBraun dry box.

Instrumentation

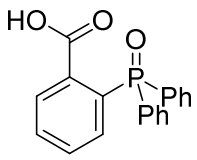
A ThermoNicolet Avatar 360 spectrometer was used to collect FT-IR spectra and the data were processed with the OMNIC software. Melting points were determined in air using an automated Stanford Research Systems OptiMelt instrument. NMR spectra were recorded on a 400 MHz Bruker AVANCE-400 NMR spectrometer. ^1H and ^{13}C chemical shifts are reported in ppm relative to SiMe_4 ($\delta = 0.00$ ppm). ^1H and $^{13}\text{C}\{^1\text{H}\}$ NMR spectra were referenced internally to residual solvent peaks. ^{19}F spectra were referenced externally to CFCl_3 (0.00 ppm). ^{31}P NMR spectra were referenced externally to 85% H_3PO_4 (0.00 ppm). Low-resolution ESI-MS spectra were obtained with an Agilent 1100 series LC/MSD mass spectrometer using MeOH as the carrier solvent. High-resolution ESI-MS spectra were collected on a Bruker Daltonics APEXIV 4.7 Tesla Fourier Transform Ion Cyclotron Resonance Mass Spectrometer at the MIT Department of Chemistry Instrumentation Facility.

2. Synthetic procedures.

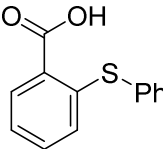
Methyl 7-bromoheptanoate

 To a solution of 7-bromoheptanoic acid (3.15 g, 15.0 mmol) in MeOH (45 mL) was added SOCl₂ (2.67 g, 1.63 mL, 7.5 mmol) in a dropwise manner. The reaction mixture was stirred at room temperature for two hours. The solution was concentrated to give the crude product as a brown liquid (3.31 g, 99%), which was used directly in the next step without further purification. ¹H NMR (400 MHz, CDCl₃) δ 3.67 (s, 3H), 3.40 (t, *J* = 6.8 Hz, 2H), 2.31 (t, *J* = 7.5 Hz, 2H), 1.86 (quintet, *J* = 6.8 Hz, 2H), 1.64 (quintet, *J* = 7.4 Hz, 2H), 1.51 – 1.41 (m, 2H), 1.41 – 1.30 (m, 2H).

2-(Diphenylphosphoryl)benzoic acid

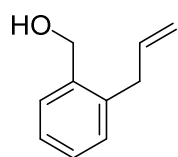
 To a solution of 2-(diphenylphosphanyl)benzoic acid (306 mg, 1.0 mmol) in CH₂Cl₂ (2 mL) was added H₂O₂ (50 wt%, 114 μL, 2.0 mmol). The reaction was kept at room temperature with stirring overnight. A portion of FeCl₃ (~5 mg) was added to the reaction mixture to decompose the excess H₂O₂. Water (20 mL) was added to the reaction mixture. The mixture was extracted with CH₂Cl₂ (20 × 5 mL). The organic layer was dried over Na₂SO₄ and filtered. The filtrate was concentrated to ca. 15 mL. Colorless crystals formed and were collected by suction filtration (231 mg, 72%). ¹H NMR (400 MHz, DMSO-*d*₆) δ 7.88 (ddd, *J* = 7.6, 3.9, 1.3 Hz, 1H), 7.70 (tt, *J* = 7.6, 1.4 Hz, 1H), 7.62 (tdd, *J* = 7.5, 2.1, 1.4 Hz, 1H), 7.58 – 7.45 (m, 11H). ³¹P NMR (162 MHz, DMSO-*d*₆) δ 29.0.

2-(Phenylthio)benzoic acid

 This compound was synthesized according to a published procedure.⁶ A mixture of thiophenol (1.16 mL, 1.26 g, 11.4 mmol), 2-bromobenzoic acid (1.77 g, 8.8 mmol), K₂CO₃ (1.21 g, 8.8 mmol), Cu powder (51 mg, 0.8 mmol), Cu₂O (38 mg,

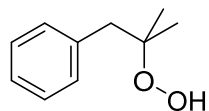
0.4 mmol), and 2-ethoxyethanol (3 mL) was heated to 130 °C for four hours. The reaction was cooled to room temperature and the solvent was removed under vacuum. The residue was mixed with H₂O (30 mL) and treated with decolorizing charcoal. The mixture was filtered through Celite. The filtrate was acidified with 2 M HCl to pH = 5 to give a precipitate. The solid was isolated by suction filtration and dissolved in 5% Na₂CO₃ aq. (100 mL). The solution was filtered through Celite and subjected to precipitation by acidifying with 2 M HCl to pH = 5. The precipitate was collected by suction filtration to give a grey solid (1.55 g, 76%). ¹H NMR (400 MHz, CDCl₃) δ 8.15 (d, *J* = 6.9 Hz, 1H), 7.59 (dd, *J* = 6.4, 2.9 Hz, 2H), 7.48 – 7.43 (m, 3H), 7.29 (t, *J* = 7.4 Hz, 1H), 7.16 (t, *J* = 7.4 Hz, 1H), 6.82 (d, *J* = 8.1 Hz, 1H). ¹H NMR spectroscopic data are consistent with a previous report.⁶ Mp = 169.0-172.5 °C.

(2-Allylphenyl)methanol



To a solution of 2-allylbenzaldehyde (146 mg, 1.0 mmol) in EtOH (2 mL) was added NaBH₄ (18.9 mg, 0.5 mmol) at 0 °C. The reaction was gradually warmed to room temperature and stirred overnight. The solvent was evaporated under vacuum. The crude product was purified by column chromatography (hexanes:ethyl acetate = 4:1) to give a colorless liquid (114 mg, 77%). ¹H NMR (400 MHz, CDCl₃) δ 7.39 (m, 1H), 7.30 – 7.26 (m, 1H), 7.26 – 7.19 (m, 2H), 6.01 (ddt, *J* = 17.0, 10.1, 6.3 Hz, 1H), 5.08 (dq, *J* = 10.1, 1.6 Hz, 1H), 5.01 (dq, *J* = 17.1, 1.8 Hz, 1H), 4.71 (s, 2H), 3.48 (dt, *J* = 6.2, 1.5 Hz, 2H). ¹H NMR spectroscopic data are consistent with a previous report.³

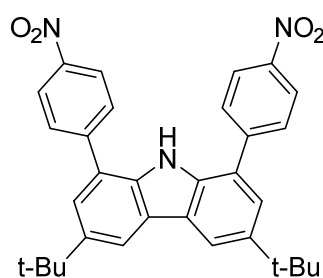
2-Methyl-1-phenylprop-2-yl hydroperoxide (MPPH)



MPPH was prepared based on modified published procedures.⁷⁻⁸ H₂O₂ (50 wt%, 2.45 g, 36 mmol) and conc. H₂SO₄ (82 μL) were mixed at 0 °C. 2-Methyl-1-phenyl-prop-2-yl alcohol (901 mg, 6.0 mmol) was added to the above mixture at 0 °C.

The reaction mixture was heated at 40 °C for 12 h. Distilled water (9 mL) was added to the reaction mixture at room temperature. The mixture was extracted with pentane (9 mL). The organic layer was dried over MgSO₄ and filtered. The filtrate was stored at -40 °C to give a white precipitate. The liquid was decanted. The solid was dissolved in pentane and colorless needles of MPPH were obtained by slow evaporation. CAUTION: Previous report noticed that distillation of the MPPH/ether solution resulted in an explosion!⁷ The crystals were washed with a small amount of pentane. This procedure was repeated two more times to give colorless needles (647 mg, 65%). ¹H NMR (400 MHz, CDCl₃) δ 7.32 – 7.27 (m, 2H), 7.25 – 7.20 (m, 3H), 2.89 (s, 2H), 1.22 (s, 6H). ¹H NMR spectroscopic data are consistent with a previous report (OOH proton was not observed).⁸ Mp = 43.1-44.7 °C.

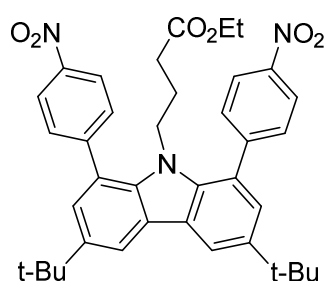
3,6-Di-*tert*-butyl-1,8-bis(4-nitrophenyl)-9*H*-carbazole (2)



4-Nitrobenzeneboronic acid pinacol ester (500 mg, 2.0 mmol) and 1,8-dibromo-3,6-di(*tert*-butyl)carbazole³ (350 mg, 0.8 mmol), and K₂CO₃ (498 mg, 3.6 mmol) were added to a mixture of THF (27 mL) and deionized H₂O (9 mL). The mixture was degassed at room temperature for 30 min. (Ph₃P)₄Pd (92 mg, 0.08 mmol) was added and the reaction was heated to reflux under N₂ atmosphere for 12 h. The reaction mixture was quenched with HCl aq. (2 M) and extracted with CH₂Cl₂ (4 × 20 mL). The combined organic phase was dried over Na₂SO₄. The solvent was removed under reduced pressure and the crude product was purified by column chromatography (hexanes:CH₂Cl₂ = 8:1 to 4:1) to give the titled product as a bright orange solid (350 mg, 84%). ¹H NMR (400 MHz, CDCl₃) δ 8.41 – 8.36 (m, 4H), 8.20 (dd, *J* = 1.8, 0.4 Hz, 2H), 8.13 (br, 1H), 7.86 – 7.79 (m, 4H), 7.51 (d, *J* = 1.8 Hz, 2H), 1.51 (s, 18H). ¹³C{¹H} NMR (101 MHz, CDCl₃) δ 147.2, 146.3, 144.1, 135.6, 129.0, 124.8, 124.7, 124.6, 122.4, 117.5, 35.1,

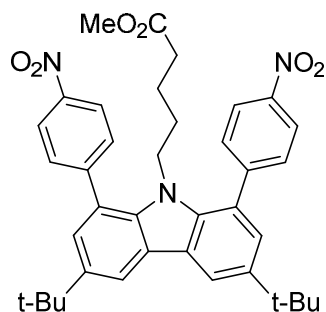
32.1. ESI-MS(+) m/z calculated for $C_{32}H_{31}N_3O_4^-$ ($[M]^-$) = 521.2, found 521.2. Mp (decomp.) = 343.6 °C.

Ethyl 4-(3,6-di-*tert*-butyl-1,8-bis(4-nitrophenyl)-9*H*-carbazol-9-yl)butanoate (3a)



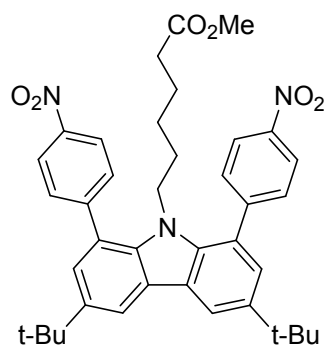
3,6-Di-*tert*-butyl-1,8-bis(4-nitrophenyl)-9*H*-carbazole (1.04 g, 2.0 mmol) and NaH (58 mg, 2.4 mmol) were weighed into a Schlenk flask in a glove box. The flask was removed from the glove box and anhydrous DMF (50 mL) was added under a N_2 flow. The reaction solution turned dark blue and was kept at room temperature with stirring for one hour. Ethyl 4-bromobutanoate (344 μ L, 468.9 mg, 2.4 mmol) was then added and the reaction mixture was kept at 80 °C with stirring for three hours to produce a clear brown solution. The reaction was quenched with HCl aq. (2 M) under N_2 . To the reaction mixture was added H_2O (200 mL), which resulted in the precipitation of a large amount of yellow solid. The solid was collected by suction filtration, washed with water, and air dried. The crude product was purified by column chromatography (CH_2Cl_2 :hexanes = 1:1 to 1:0) to afford **3a** as a yellow solid (725 mg, 57%). The reaction is particularly sensitive to moisture and should be performed under rigorously anhydrous conditions. 1H NMR (400 MHz, $CDCl_3$) δ 8.38 – 8.33 (m, 4H), 8.18 (d, J = 1.9 Hz, 2H), 7.81 – 7.73 (m, 4H), 7.34 (d, J = 1.9 Hz, 2H), 3.84 (q, J = 7.1 Hz, 2H), 3.37 (pseudo t, J = 7.4 Hz, 2H), 1.50 (s, 18H), 1.24 (t, J = 7.5 Hz, 2H), 1.07 (m, 5H). ^{13}C { 1H } NMR (101 MHz, $CDCl_3$) δ 172.1, 147.8, 147.1, 144.2, 138.8, 129.9, 126.8, 126.7, 124.5, 123.9, 117.1, 60.4, 46.1, 34.9, 32.0, 30.4, 23.3, 14.1. ESI-MS(+) m/z calculated for $C_{38}H_{42}N_3O_6^+$ ($[M+H]^+$) = 636.3, found 636.4. Mp = 241.2-244.5 °C.

Methyl 5-(3,6-di-*tert*-butyl-1,8-bis(4-nitrophenyl)-9*H*-carbazol-9-yl)pentanoate (**3b**)



3,6-Di-*tert*-butyl-1,8-bis(4-nitrophenyl)-9*H*-carbazole (1.04 g, 2.0 mmol) and NaH (58 mg, 2.4 mmol) were weighed into a Schlenk flask in a glove box. The flask was removed from the glove box and anhydrous DMF (50 mL) was added under a N₂ flow. The reaction solution turned dark blue and was stirred at room temperature for one hour. Methyl 5-bromopentanoate (344 μL, 469 mg, 2.4 mmol) was then added to the reaction mixture and the reaction was stirred at 80 °C for three hours to lead to a clear brown solution. The reaction was worked up as described above for **3a**. The crude product was purified by column chromatography (CH₂Cl₂:hexanes = 1:1 to 1:0) to give **3b** as a yellow solid (1.22 g, 96%). ¹H NMR (400 MHz, CDCl₃) δ 8.37–8.32 (m, 4H), 8.15 (d, *J* = 1.9 Hz, 2H), 7.74–7.71 (m, 4H), 7.29 (d, *J* = 2.0 Hz, 2H), 3.48 (s, 3H), 3.32–3.26 (m, 2H), 1.68 (t, *J* = 7.3 Hz, 2H), 1.48 (s, 18H), 0.79–0.70 (m, 2H), 0.60–0.53 (m, 2H). ¹³C{¹H} NMR (101 MHz, CDCl₃) δ 173.1, 147.9, 147.1, 143.9, 138.6, 130.0, 126.7, 126.4, 124.4, 123.8, 117.0, 51.4, 46.3, 34.8, 32.9, 32.0, 27.5, 21.2. ESI-MS(+) *m/z* calculated for C₃₈H₄₂N₃O₆⁺ ([M+H]⁺) = 636.3, found 636.5. Mp = 277.9–279.2 °C.

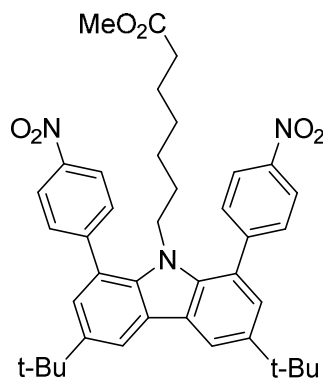
Methyl 6-(3,6-di-*tert*-butyl-1,8-bis(4-nitrophenyl)-9*H*-carbazol-9-yl)hexanoate (**3c**)



3,6-Di-*tert*-butyl-1,8-bis(4-nitrophenyl)-9*H*-carbazole (1.04 g, 2.0 mmol) and NaH (58 mg, 2.4 mmol) were weighed into a Schlenk flask in a glove box. The flask was removed from the glove box and anhydrous DMF (50 mL) was added under a N₂ flow. The reaction turned dark blue and was stirred at room temperature for one hour. Methyl 6-bromohexanoate (380 μL, 502 mg, 2.4 mmol) was then added to the reaction mixture

followed by stirring at 80 °C for three hours to lead to a clear brown solution. The reaction was worked up as described above for **3a**. The crude product was purified by column chromatography (CH₂Cl₂:hexanes = 1:1 to 1:0) to give **3c** as a yellow solid (1.16 g, 89%). ¹H NMR (400 MHz, CDCl₃) δ 8.37 – 8.31 (m, 4H), 8.16 (d, *J* = 2.0 Hz, 2H), 7.76 – 7.70 (m, 4H), 7.30 (d, *J* = 2.0 Hz, 2H), 3.55 (s, 3H), 3.28 (pseudo t, *J* = 7.7 Hz, 2H), 1.84 (t, *J* = 7.6 Hz, 2H), 1.48 (s, 18H), 0.96 (quintet, *J* = 7.6 Hz, 2H), 0.73 (quintet, *J* = 7.5 Hz, 2H), 0.25 (quintet, *J* = 7.7 Hz, 2H). ¹³C{¹H} NMR (101 MHz, CDCl₃) δ 173.6, 148.0, 147.1, 143.9, 138.7, 130.0, 126.7, 126.5, 124.4, 123.8, 117.0, 51.5, 46.5, 34.9, 33.6, 32.0, 27.6, 25.4, 24.0. ESI-MS(+) *m/z* calculated for C₃₉H₄₄N₃O₆⁺ ([M+H]⁺) = 650.3, found 650.4. Mp = 223.6-227.6 °C.

Methyl 7-(3,6-di-*tert*-butyl-1,8-bis(4-nitrophenyl)-9*H*-carbazol-9-yl)heptanoate (3d)

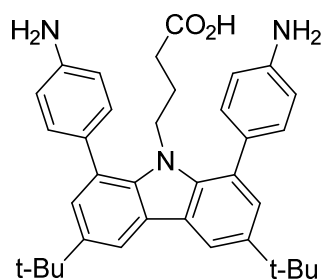


3,6-Di-*tert*-butyl-1,8-bis(4-nitrophenyl)-9*H*-carbazole (261 mg, 0.5 mmol) and NaH (14.4 mg, 2.4 mmol) were weighed into a Schlenk flask in a glove box. The flask was removed from the glove box and anhydrous DMF (12 mL) was added under a N₂ flow. The reaction solution turned dark blue and was allowed to stir at room temperature for one hour. Methyl 7-bromoheptanoate (167 mg, 0.75 mmol) was

then added to the reaction mixture and the reaction was stirred at 80 °C for three hours to give a clear brown solution. The reaction was worked up as described above for **3a**. The crude product was purified by column chromatography (CH₂Cl₂:hexanes = 1:1 to 1:0) to give **3d** as a yellow solid (312 mg, 94%). ¹H NMR (400 MHz, CDCl₃) δ 8.36 – 8.31 (m, 4H), 8.16 (d, *J* = 2.0 Hz, 2H), 7.76 – 7.70 (m, 4H), 7.30 (d, *J* = 2.0 Hz, 2H), 3.60 (s, 3H), 3.27 (pseudo t, *J* = 7.6 Hz, 2H), 1.97 (t, *J* = 7.5 Hz, 2H), 1.48 (s, 18H), 1.16 (quintet, *J* = 7.5 Hz, 2H), 0.69 (pseudo tt, *J* = 7.7 Hz, 4H), 0.24 (quintet, *J* = 7.4 Hz, 2H). ¹³C{¹H} NMR (101 MHz, CDCl₃) δ 174.0, 148.1, 147.1,

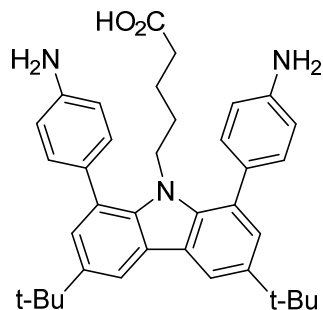
143.9, 138.8, 130.0, 126.7, 126.5, 124.4, 123.8, 117.0, 51.6, 46.8, 34.9, 33.7, 32.0, 28.2, 27.7, 25.5, 24.4. ESI-MS(+) m/z calculated for $C_{40}H_{46}N_3O_6^+$ ($[M+H]^+$) = 664.3, found 664.9. Mp = 225.1-227.7 °C.

4-(1,8-Bis(4-aminophenyl)-3,6-di-*tert*-butyl-9H-carbazol-9-yl)butanoic acid (4a)



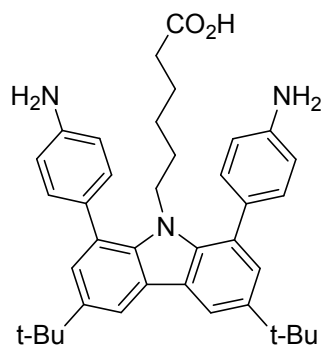
A solution of **3a** (655 mg, 1.03 mmol) in EtOH/H₂O/NaOH (100 mL/20 mL/2.0 g) was heated to reflux for two hours. The reaction was cooled to room temperature and EtOH was removed under vacuum. The reaction mixture was neutralized with HCl aq. (2 M) and extracted with CH₂Cl₂ (4 × 40 mL). The combined organic layer was dried over Na₂SO₄ and the solvent was removed under vacuum. The crude product was obtained as a white solid and used directly in the next step without further purification. The carbazole derivative was mixed with N₂H₄ aq. (70 wt%, 0.82 mL, 16.6 mmol) and Pd/C (10 wt%, 29 mg) at room temperature. The reaction mixture was then heated to reflux overnight. Pd/C was removed by suction filtration through Celite. EtOH was removed under vacuum. The crude product was purified by column chromatography (CH₂Cl₂:MeOH = 95:5 to 8:1) to give an off-white powder (326 mg, 58%). ¹H NMR (400 MHz, CD₃OD) δ 8.06 (d, J = 2.0 Hz, 2H), 7.28 – 7.20 (m, 6H), 6.80 (d, J = 8.4 Hz, 4H), 3.52 (pseudo t, J = 7.4 Hz, 2H), 1.43 (s, 18H), 1.22 (t, J = 7.9 Hz, 2H), 1.03 (quintet, J = 7.3 Hz, 2H). ¹³C {¹H} NMR (101 MHz, CD₃OD) δ 176.6, 147.8, 143.8, 139.9, 132.0, 131.0, 128.4, 127.5, 127.1, 116.4, 115.6, 45.3, 35.4, 32.4, 31.7, 25.0. ESI-MS(+) m/z calculated for $C_{36}H_{42}N_3O_2^+$ ($[M+H]^+$) = 548.3, found 548.4. Mp = 212.2-215.8 °C.

5-(1,8-Bis(4-aminophenyl)-3,6-di-*tert*-butyl-9H-carbazol-9-yl)pentanoic acid (**4b**)



A solution of **3b** (12.1 mg, 1.91 mmol) in EtOH/H₂O/NaOH (185 mL/37 mL/3.7 g) was heated to reflux for two hours. The reaction was worked up as described above for **4a**. The crude product was obtained as a white solid and was used directly in the next step without further purification. The carbazole derivative was mixed with N₂H₄ aq. (70 wt%, 2.41 mL, 30.8 mmol) and Pd/C (10 wt%, 54 mg) at room temperature. The reaction mixture was then heated to reflux overnight. The reaction was worked up as described above for **4a**. The crude product was purified by column chromatography (CH₂Cl₂:MeOH = 95:5 to 8:1) to give an off-white powder (716 mg, 67%). ¹H NMR (400 MHz, CDCl₃) δ 8.04 (d, *J* = 2.0 Hz, 2H), 7.31 – 7.27 (m, 4H), 7.24 (d, *J* = 2.0 Hz, 2H), 6.77 – 6.71 (m, 4H), 4.02 (br, 3H, overlapping with H₂O), 3.48 (pseudo t, *J* = 7.9 Hz, 2H), 1.73 (t, *J* = 7.5 Hz, 2H), 1.46 (s, 18H), 0.83 (quintet, *J* = 7.3 Hz, 2H), 0.69 (quintet, *J* = 7.5 Hz, 2H). ¹³C{¹H} NMR (101 MHz, CDCl₃) δ 178.4, 145.4, 142.4, 138.4, 131.7, 130.4, 126.8, 126.4, 125.5, 115.0, 114.8, 44.7, 34.7, 33.2, 32.1, 27.9, 21.3. ESI-MS(+) *m/z* calculated for C₃₇H₄₄N₃O₂⁺ ([M+H]⁺) = 562.3, found 561.4. Mp = 257.2-260.1 °C.

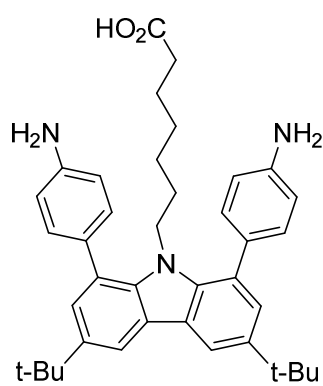
6-(1,8-Bis(4-aminophenyl)-3,6-di-*tert*-butyl-9H-carbazol-9-yl)hexanoic acid (**4c**)



A solution of **3c** (1.16 g, 1.79 mmol) in EtOH/H₂O/NaOH (180 mL/36 mL/3.6 g) was heated to reflux for two hours. The reaction was worked up as described above for **4a**. The crude product was obtained as a white solid and was used directly in the next step without further purification. The carbazole derivative was mixed with N₂H₄ aq. (70 wt%, 1.40 mL, 28.6 mmol) and Pd/C (10 wt%, 52 mg) at room temperature. The reaction was

worked up as described above for **4a**. The crude product was purified by column chromatography (CH₂Cl₂:MeOH = 95:5 to 8:1) to give an off-white powder (928 mg, 90%). ¹H NMR (400 MHz, CDCl₃) δ 8.07 (d, *J* = 1.6 Hz, 2H), 7.30 (pseudo d, *J* = 8.0 Hz, 4H), 7.25 (m, 2H), 6.74 (pseudo d, *J* = 8.1 Hz, 4H), 4.70 (s, 5H), 3.48 (pseudo t, *J* = 8.0 Hz, 2H), 1.99 (t, *J* = 7.4 Hz, 2H), 1.47 (s, 18H), 1.06 (quintet, *J* = 7.7 Hz, 2H), 0.82 (quintet, *J* = 7.7 Hz, 2H), 0.40 (quintet, *J* = 7.6 Hz, 1H). ¹³C {¹H} NMR (101 MHz, CDCl₃) δ 178.7, 145.1, 142.2, 138.2, 132.0, 130.4, 126.8, 126.3, 125.3, 115.1, 114.8, 44.9, 34.7, 34.2, 32.1, 28.1, 25.7, 24.2. ESI-MS(+) *m/z* calculated for C₃₈H₄₆N₃O₂⁺ ([M+H]⁺) = 576.4, found 576.5. Mp = 223.6-227.6 °C.

7-(1,8-Bis(4-aminophenyl)-3,6-di-*tert*-butyl-9H-carbazol-9-yl)heptanoic acid (**4d**)

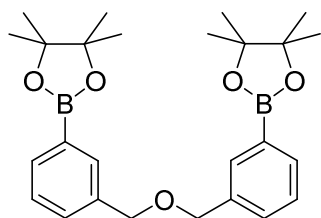


A solution of **3d** (312 mg, 0.47 mmol) in EtOH/H₂O/NaOH (45 mL/9.4 mL/0.94 g) was heated to reflux for two hours. The reaction was worked up as described above for **4a**. The crude product was obtained as a white solid and was used directly in the next step without further purification. The carbazole derivative was mixed with N₂H₄ aq. (70 wt%, 0.37 mL, 7.5 mmol) and Pd/C (10 wt%, 13 mg) at

room temperature. The reaction mixture was then heated to reflux overnight. The reaction was worked up as described above for **4a**. The crude product was purified by column chromatography (CH₂Cl₂:MeOH = 95:5 to 8:1) to give an off-white powder (230 mg, 83%). ¹H NMR (400 MHz, CD₃OD) δ 8.05 (d, *J* = 2.0 Hz, 2H), 7.28 – 7.21 (m, 6H), 6.87 – 6.81 (m, 4H), 3.52 (pseudo t, *J* = 7.9 Hz, 2H), 2.03 (t, *J* = 7.5 Hz, 2H), 1.48 (s, 18H) 1.21 (quintet, *J* = 7.6 Hz, 2H), 0.75 (pseudo quintet, *J* = 7.8 Hz, 4H), 0.34 (quintet, *J* = 7.6 Hz, 2H). ¹³C {¹H} NMR (101 MHz, CDCl₃) δ 178.3, 144.9, 142.3, 138.3, 132.2, 130.4, 126.8, 126.3, 125.4, 115.3, 114.8, 45.1, 34.7,

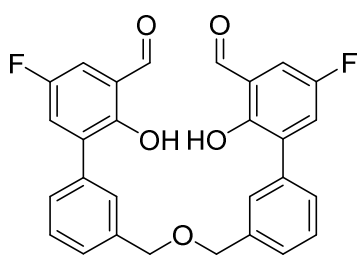
34.1, 32.1, 28.1, 27.8, 25.8, 24.8. ESI-MS(+) m/z calculated for $C_{39}H_{48}N_3O_2^+$ ($[M+H]^+$) = 590.4, found 590.4. Mp = 232.6-237.5 °C.

((Oxybis(methylene))bis(3,1-phenylene))diboronic acid pinacol ester



3,3'-(Oxybis(methylene))bis(bromobenzene) (6.47 g, 18.2 mmol), KOAc (5.17 g, 52.7 mmol), bis(pinacolato)diboron (10.1 g, 40.0 mmol), and $PdCl_2(dppf) \cdot CH_2Cl_2$ (742 mg, 0.91 mmol) were mixed in degassed THF (100 mL). The reaction was heated at 80 °C under N_2 atmosphere for 24 h. The reaction mixture was poured into water (400 mL) and extracted with CH_2Cl_2 (30×5 mL). The organic layer was dried over Na_2SO_4 and filtered. The solvents were removed under reduced pressure. The crude product was purified by column chromatography (hexanes:ethyl acetate = 4:1) to give a white solid (7.78 g, 95%). 1H NMR (400 MHz, $CDCl_3$) δ 7.78 (s, 2H), 7.74 (pseudo d, $J = 7.3$ Hz, 2H), 7.50 (dt, $J = 7.6, 1.5$ Hz, 2H), 7.37 (t, $J = 7.5$ Hz, 2H), 4.56 (s, 4H), 1.35 (s, 12H). $^{13}C\{^1H\}$ NMR (101 MHz, $CDCl_3$) δ 137.6, 134.3, 134.2, 130.9, 127.9, 127.7, 83.8, 72.3, 24.9. ESI-MS(+) m/z calculated for $C_{26}H_{36}B_2NaO_5^+$ ($[M+Na]^+$) = 473.3, found 473.3. Mp = 86.1-89.5 °C.

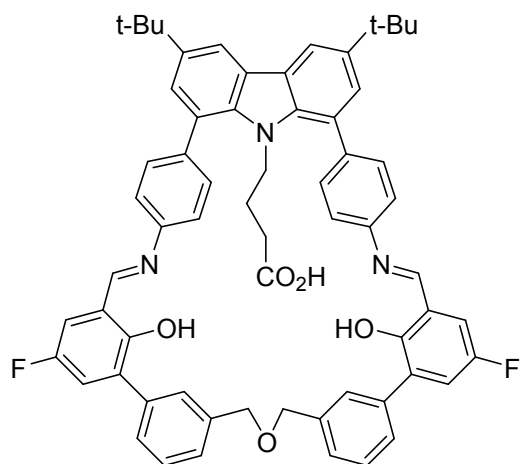
3',3'''-(Oxybis(methylene))bis(5-fluoro-2-hydroxy-[1,1'-biphenyl]-3-carbaldehyde) (5)



((Oxybis(methylene))bis(3,1-phenylene))diboronic acid pinacol ester (1.43 g, 5.0 mmol), 3-bromo-5-fluoro-2-hydroxybenzaldehyde (2.63 g, 12.0 mmol),⁹ and K_2CO_3 (3.11 g, 22.5 mmol) were mixed in THF/ H_2O (3:1, 180 mL). The mixture was degassed at room temperature for 30 min. $(Ph_3P)_4Pd$ (578 mg, 0.5 mmol) was added and the reaction was heated to reflux under N_2 atmosphere for 12 h. The reaction was cooled to room temperature and extracted with CH_2Cl_2 (30×3 mL). The organic layer was dried over Na_2SO_4

and filtered. The solvents were removed under reduced pressure. The crude product was purified by column chromatography (hexanes:ethyl acetate = 8:1) to give a slightly yellow solid (878 mg, 37%). ¹H NMR (400 MHz, CDCl₃) δ 11.30 (d, *J* = 0.4 Hz, 2H), 9.90 (s, 2H), 7.60 (td, *J* = 1.7, 0.6 Hz, 2H), 7.53 (dt, *J* = 7.4, 1.7 Hz, 2H), 7.45 (dt, *J* = 7.5, 3.8 Hz, 1H), 7.41 (dt, *J* = 7.6, 1.6 Hz, 1H), 7.37 (ddd, *J* = 9.0, 3.1, 0.5 Hz, 2H), 7.25 (dd, *J* = 7.2, 3.1 Hz, 2H), 4.66 (s, 4H). ¹⁹F NMR (376 MHz, CDCl₃) δ -123.4 (t, *J* = 8.0 Hz). NMR spectroscopic data are consistent with a previous report.⁹ Mp = 169.0-172.5 °C.

H₃PIMIC3

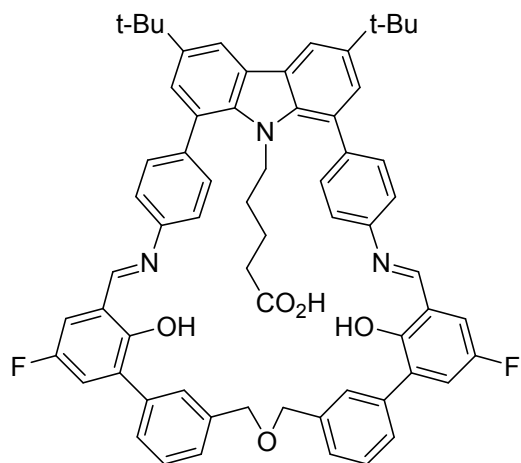


To a solution of **4a** (165 mg, 0.30 mmol) and bis(carbaldehyde) (141 mg, 0.30 mmol) in anhydrous MeCN-CH₂Cl₂ (225 mL/9 mL) was added trifluoroacetic acid (180 μL, 2.4 mmol) under N₂ atmosphere. An orange material formed after 30 min. The reaction mixture was stirred overnight. The solid was isolated by centrifugation (4000 rpm, 10 min). The solid was

then mixed with acetonitrile (25 mL) and sonicated for 10 min. Acetonitrile was removed from the mixture by centrifugation (4000 rpm, 10 min). This process was repeated 3 times. The product was dried under vacuum to give an orange solid (185 mg, 63%). The material was used directly in the metalation reaction. Analytically pure material was obtained by column chromatography (hexanes:ethyl acetate = 1:1). ¹H NMR (400 MHz, CDCl₃) δ 8.67 (s, 2H), 8.09 (d, *J* = 1.8 Hz, 2H), 7.72 (s, 2H), 7.59 (d, *J* = 8.4 Hz, 4H), 7.52 – 7.43 (m, 4H), 7.41 – 7.31 (m, 8H), 7.21 (dd, *J* = 9.1, 3.1 Hz, 2H), 7.09 (dd, *J* = 8.0, 3.1 Hz, 2H), 4.64 (s, 4H), 3.01 (t, *J* = 7.4 Hz, 2H), 1.49 (d, *J* = 7.2 Hz, 18H), 1.20 (d, *J* = 7.7 Hz, 2H), 0.88 (quintet, *J* = 7.7 Hz, 2H). ¹⁹F NMR (376

MHz, CDCl₃) δ -125.3 (t, J = 8.5 Hz, 2F). ¹³C{¹H} NMR (101 MHz, CDCl₃) δ 178.0 (s), 160.9 (s), 155.5 (d, J = 237.3 Hz), 155.2 (s), 146.2 (s), 144.0 (s), 139.8 (s), 139.6 (s), 138.2 (s), 136.7 (s), 131.6 (d, J = 6.9 Hz), 130.3 (s), 129.5 (s), 128.9 (s), 128.2 (s), 127.3 (s), 126.7 (s), 126.2 (s), 125.5 (s), 121.6 (s), 121.1 (d, J = 23.5 Hz), 119.2 (d, J = 7.6 Hz), 116.3 (d, J = 22.9 Hz), 116.0 (s), 73.1 (s), 45.4 (s), 34.8 (s), 32.1 (s), 30.5 (s), 23.2 (s). IR (KBr): ν 3032, 2963, 2898, 2863, 1709, 1623, 1584, 1472, 1450, 1429, 1355, 1312, 1282, 1243, 1204, 1108, 992, 871, 854, 785, 759, 694, 672, 530 cm⁻¹. ESI-MS(+) m/z calculated for [M+H]⁺ = 986.4, found 986.4. DART-HRMS(+) m/z calculated for C₆₄H₅₈F₂N₃O₅⁺ ([M+H]⁺) = 986.4339, found 986.4338. Mp (decomp.) = 287.9 °C.

H₃PIMIC4

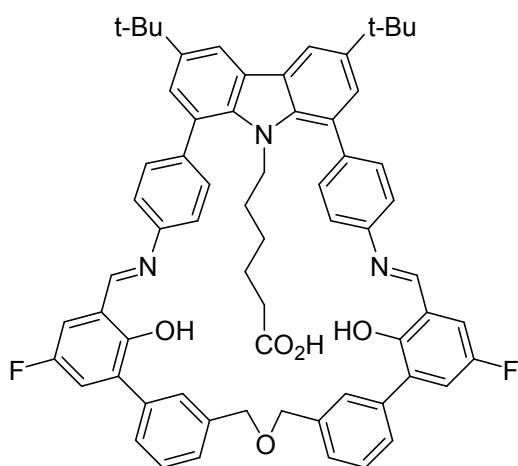


To a solution of **4b** (112 mg, 0.20 mmol) and bis(carbaldehyde) (95 mg, 0.20 mmol) in anhydrous MeCN-CH₂Cl₂ (150 mL/6 mL) was added trifluoroacetic acid (120 μ L, 1.6 mmol) under N₂ atmosphere. An orange material formed after 30 min. The reaction mixture was stirred overnight. The reaction was worked up as described above for H₃PIMIC3. The

product was dried under vacuum to give an orange solid (140 mg, 70%). The material was used directly in the metalation reaction. Analytically pure material was obtained by column chromatography (hexanes:ethyl acetate = 1:1). ¹H NMR (400 MHz, CDCl₃) δ 8.66 (s, 2H), 8.09 (d, J = 1.9 Hz, 2H), 7.59 (s, 2H), 7.53 (pseudo d, J = 8.2 Hz, 4H), 7.46 – 7.28 (m, 12H), 7.16 (dd, J = 9.0, 3.0 Hz, 2H), 7.06 (dd, J = 7.9, 3.1 Hz, 2H), 4.51 (s, 4H), 2.92 (t, J = 6.4 Hz, 2H), 1.68 (t, J = 6.7 Hz, 2H), 1.49 (s, 18H), 0.56 (s, 2H). ¹⁹F NMR (376 MHz, CDCl₃) δ -125.4 (t, J = 8.4 Hz,

2F). $^{13}\text{C}\{^1\text{H}\}$ NMR (101 MHz, CDCl_3) δ 178.9, 160.7, 155.4 (d, $J = 237.0$ Hz), 155.1, 146.2, 143.6, 139.8(6), 139.7(9), 138.1, 136.6, 131.6 (d, $J = 6.9$ Hz), 130.3, 129.4, 128.8, 128.2, 127.2, 126.6, 126.2, 125.4, 121.5, 121.0 (d, $J = 23.5$ Hz), 119.2 (d, $J = 7.6$ Hz), 116.3 (d, $J = 23.0$ Hz), 115.9, 72.9, 45.6, 34.9, 33.1, 32.1, 27.3, 21.1. IR (KBr): ν 3041, 2958, 2924, 2863, 1705, 1619, 1584, 1467, 1450, 1419, 1363, 1316, 1282, 1260, 1204, 1187, 1109, 996, 875, 836, 785, 741, 702, 672, 534 cm^{-1} . ESI-MS(+) m/z calculated for $[\text{M}+\text{H}]^+ = 1000.4$, found 1001.1. DART-HRMS(+) m/z calculated for $\text{C}_{65}\text{H}_{60}\text{F}_2\text{N}_3\text{O}_5^+$ ($[\text{M}+\text{H}]^+$) = 1000.4496, found 1000.4518. Mp (decomp.) = 301.0 $^\circ\text{C}$.

H₃PIMIC5

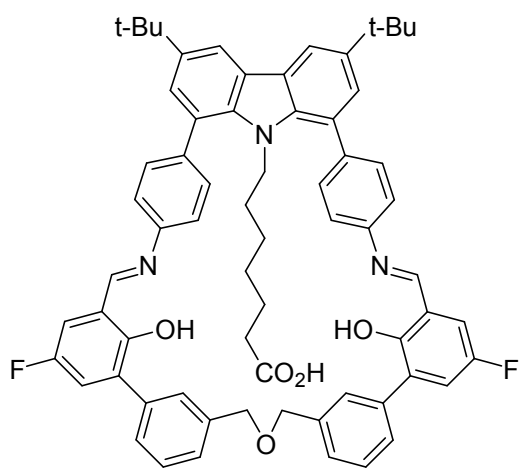


To a solution of **4c** (115 mg, 0.20 mmol) and bis(carbaldehyde) (95 mg, 0.20 mmol) in anhydrous $\text{MeCN-CH}_2\text{Cl}_2$ (150 mL/6 mL) was added trifluoroacetic acid (120 μL , 1.6 mmol) under a N_2 atmosphere. An orange material formed after 30 min. The reaction mixture was stirred overnight. The reaction was worked up as described above for H₃PIMIC3.

The product was dried under vacuum to give an orange solid (164 mg, 81%). The material was used directly in the metalation reaction. Analytically pure material was obtained by column chromatography (hexanes:ethyl acetate = 1:1). ^1H NMR (400 MHz, CDCl_3) δ 8.70 (s, 2H), 8.11 (d, $J = 1.9$ Hz, 2H), 7.74 (s, 2H), 7.61 (d, $J = 8.4$ Hz, 4H), 7.53 – 7.33 (m, 12H), 7.19 (dd, $J = 9.1$, 3.1 Hz, 2H), 7.11 (dd, $J = 8.0$, 3.1 Hz, 2H), 4.66 (s, 2H), 2.99 (d, $J = 15.3$ Hz, 1H), 1.83 (t, $J = 7.6$ Hz, 1H), 0.96 (dt, $J = 15.4$, 7.8 Hz, 2H), 0.63 (dt, $J = 15.0$, 7.6 Hz, 1H), 0.27 (dt, $J = 15.1$, 7.4 Hz, 1H). ^{19}F NMR (376 MHz, CDCl_3) δ -125.3 (t, $J = 8.5$ Hz). $^{13}\text{C}\{^1\text{H}\}$ NMR (101 MHz,

CDCl₃) δ 178.6 (s), 160.8 (s), 155.4 (d, *J* = 237.3 Hz), 155.2 (s), 146.2 (s), 143.5 (s), 139.9 (s, two carbon signals overlap), 138.2 (s), 136.7 (s), 131.6 (d, *J* = 7.0 Hz), 130.4 (s), 129.5 (s), 128.9 (s), 128.2 (s), 127.4 (s), 126.4 (s), 126.1 (s), 125.4 (s), 121.5 (s), 121.0 (d, *J* = 23.7 Hz), 119.2 (d, *J* = 7.5 Hz), 116.3 (d, *J* = 22.8 Hz), 115.8 (s), 73.1 (s), 45.9 (s), 34.9 (s), 33.4 (s), 32.1 (s), 27.5 (s), 25.5 (s), 23.7 (s). IR (KBr): ν 3036, 2950, 2924, 2863, 1705, 1619, 1584, 1458, 1419, 1359, 1325, 1282, 1259, 1204, 1147, 1109, 996, 878, 841, 785, 733, 698, 646, 533 cm⁻¹. ESI-MS(+) *m/z* calculated for [M+H]⁺ = 1014.5, found 1015.1. DART-HRMS(+) *m/z* calculated for C₆₆H₆₂F₂N₃O₅⁺ ([M+H]⁺) = 1014.4652, found 1014.4673. Mp (decomp.) = 248.5 °C.

H₃PIMIC6



To a solution of **4d** (118 mg, 0.20 mmol) and bis(carbaldehyde) (95 mg, 0.20 mmol) in anhydrous MeCN-CH₂Cl₂ (150 mL/6 mL) was added trifluoroacetic acid (120 μL, 1.6 mmol) under N₂ atmosphere. An orange material formed after 30 min. The reaction mixture was stirred overnight. The reaction was worked up as described above for H₃PIMIC3. The

product was dried under vacuum to give an orange solid (190 mg, 92%). The material was used directly in the metalation reaction. Analytically pure material was obtained by column chromatography (hexanes:ethyl acetate = 1:1). ¹H NMR (400 MHz, CDCl₃) δ 8.75 (s, 2H), 8.15 (d, *J* = 1.8 Hz, 2H), 7.78 (s, 2H), 7.66 (d, *J* = 8.3 Hz, 4H), 7.56 – 7.37 (m, 12H), 7.23 (dd, *J* = 9.0, 3.0 Hz, 2H), 7.15 (dd, *J* = 7.9, 3.0 Hz, 2H), 4.70 (s, 4H), 3.03 (t, *J* = 7.6 Hz, 2H), 2.02 (t, *J* = 7.5 Hz, 2H), 1.20 (quintet, *J* = 7.6 Hz, 2H), 0.77 – 0.60 (m, 4H), 0.29 (quintet, *J* = 7.3 Hz, 1H). ¹³C {¹H} NMR (101 MHz, CDCl₃) δ 179.1 (s), 160.8 (s), 155.4 (d, *J* = 237.1 Hz), 155.2 (d, *J* =

1.5 Hz), 146.1 (s), 143.5 (s), 139.9(3) (s), 139.9(2) (s), 138.1 (s), 136.7 (s), 131.6 (d, $J = 7.0$ Hz), 130.4 (s), 129.5 (s), 128.9 (s), 128.2 (s), 127.4 (s), 126.5 (s), 126.1 (s), 125.4 (s), 121.5 (s), 121.0 (d, $J = 23.4$ Hz), 119.2 (d, $J = 7.6$ Hz), 116.3 (d, $J = 22.8$ Hz), 115.8 (s), 73.1 (s), 46.1 (s), 34.8 (s), 33.7 (s), 32.1 (s), 28.1 (s), 27.7 (s), 25.6 (s), 24.3 (s). ^{19}F NMR (376 MHz, CDCl_3) δ -125.3 (t, $J = 8.5$ Hz). IR (KBr): ν 3032, 2954, 2928, 2854, 1709, 1619, 1584, 1446, 1424, 1359, 1316, 1282, 1238, 1204, 1143, 1109, 996, 879, 832, 785, 698, 646, 533 cm^{-1} . ESI-MS(+) m/z calculated for $[\text{M}+\text{H}]^+ = 1028.5$, found 1028.7. DART-HRMS(+) m/z calculated for $\text{C}_{67}\text{H}_{64}\text{F}_2\text{N}_3\text{O}_5^+$ ($[\text{M}+\text{H}]^+$) = 1028.4809, found 1028.4816. Mp (decomp.) = 217.0 $^\circ\text{C}$.

3. X-ray Data Collection and Refinement.

Single crystal X-ray diffraction studies were performed using suitable crystals of **6-18**. Single crystals were mounted on loops with Paratone-N oil and transferred to a N₂ cold stream (100 K) by a KRYO-FLEX low-temperature apparatus. The crystal of **9_2** was prepared and mounted in the cold stream of dry ice. Data were collected on a Bruker SMART APEX CCD X-ray diffractometer equipped with a Bruker APEX2 CCD detector with Mo K α radiation ($\lambda = 0.71073 \text{ \AA}$) controlled by the APEX2 software package.¹⁰ Intensities were measured at 100 K. Reduction of the data was performed by SAINT.¹¹ Empirical absorption corrections were calculated with SADABS.¹² The space groups were determined by XPREP¹³ through analysis of the Laue symmetry and systematic absences. The structures of **7, 8, 9_1, 10, 12, 16-18** were solved by direct or Patterson methods. Structures of **6, 9_2, 11, 13-15** were solved with SHELXT.¹⁴ All structures were refined by full-matrix least-squares based on F^2 using SHELXL (Re. 647).¹⁵ Each structure was checked for higher symmetry using PLATON.¹⁶ All non-hydrogen atoms were located and refined anisotropically. Hydrogen atoms were assigned to idealized positions and given thermal parameters equal to either 1.5 (methyl hydrogen atoms) or 1.2 (non-methyl hydrogen atoms) times the thermal parameters of the atoms to which they were attached. DSR¹⁷ was used to model the disorders of poorly defined solvent molecules in the lattice. The SQUEEZE program¹⁸ as implemented in PLATON was used to handle extremely disordered solvent in the crystal lattice of some structures. The models obtained were added as .fab-files to the refinements using SHELXL.¹⁵

Distance and anisotropic displacement parameter restraints were applied to disordered atoms. Figures were generated using the program Mercury.¹⁹ See Figures S1-S14 and Tables S1-S4 be-

low for crystallographic data and refinement details. Specific details about refinement, including disorder, are provided below for selected structures.

[Fe₂(PIMIC3)(AnthCO₂)(MeCN)]₂ (6) crystallized in the triclinic space group $P\bar{1}$. The crystal was a non-merohedral twin. Refinement was performed using an hk15 file generated by PLATON¹⁶ and the BASF refined to 0.20020. The data were merged during this process, which makes the value of R(int) meaningless.

The asymmetric unit contains one molecule, which displays disorder at two *tert*-butyl groups and a part of the benzyl ether backbone. The disorders were modeled across two positions. The main occupied part of the benzyl ether backbone refined to an occupancy of 67.8%. The main parts of the *tert*-butyl groups refined to an occupancy of 69.0% and 55.1%, respectively.

A large number of poorly defined and disordered acetonitrile and toluene solvent molecules were found in the lattice. SQUEEZE was used to handle this disorder. SQUEEZE found one void of disordered solvent, which was located at -0.001 0.003 -0.003. The volume of the void was 3220 Å³ and thus provides room for approximately 190 non-hydrogen atoms. The equivalent of 888 electrons was identified, which corresponds to approximately 25 solvent molecules and thus allows for a variety of possible combinations of acetonitrile and toluene molecules.

[Fe₂(PIMIC4)(AnthCO₂)(MeCN)] (7) crystallized in the monoclinic space group $P2_1/c$ with one molecule of the complex in the asymmetric unit. The PIMIC4³⁻ ligand is disordered in three positions. Disorder of a part of the benzyl ether backbone and of one of the *tert*-butyl groups was modeled across two positions each, the main component occupancy is 78.6% and 54.7%, respectively. Disorder of one of the 4-fluorophenolate units was modeled across three positions with occupancies of 40.8%, 23.9%, and 35.2%. Several disordered solvent molecules were found in the lattice. Squeeze was used to deal with this disorder. Four independent solvent accessible

voids were identified, which were located at 0.157 0.286 0.022, -0.157 0.786 0.478, 0.157 0.214 0.522, and -0.157 0.714 0.978. Each void had a volume of 252 Å³ and contained the equivalent of 45 electrons, which could account for either one THF (40 electrons) or two acetonitrile molecules (44 electrons). This result leads to an occupancy of only 36% of the void, which in theory provides room for approximately 15 non-hydrogen atoms.

[Fe₂(PIMIC4)(Ph₃CCO₂)(MeCN)] (8) crystallized in the triclinic space group $P\bar{1}$ with one molecule of the complex and one free acetonitrile solvent molecule in the asymmetric unit. A *tert*-butyl group was modeled to a two part disorder with occupancies of 52.8% and 47.2%. The dibenzyl ether backbone and a 4-fluorophenolate unit were modeled to a two part disorder with a main component occupancy of 77.9%.

Crystals of **[Fe₂(PIMIC5)(AnthCO₂)(MeCN)] (9)** were obtained from two different solvent mixtures, which led to solvomorphism. The two polymorphic forms of **9** are referred herein as **9_1** and **9_2**, respectively.

9_1 crystallized in the triclinic space group $P\bar{1}$ with two independent molecules per asymmetric unit. The *tert*-butyl unit of one fragment is disordered across two positions with the main component being occupied at 83.6%. Several free solvent acetonitrile and THF molecules, which were disordered and only poorly defined, were found in the lattice. SQUEEZE was used to handle this solvent disorder. One solvent accessible void was found at -0.011 0.000 0.011, which had a volume of 2068 Å³ and thus provided room for approximately 122 non-hydrogen atoms. The equivalent of 535 electrons were identified within the void. Based on the ratio of free solvent molecules, which were observed in the lattice before applying SQUEEZE, we suggest a combination of 17 acetonitrile and 4 THF molecules, which sum up to 534 electrons. This result matches the electron equivalent found by SQUEEZE nearly perfectly. This combination would

lead to an occupancy of only 58% of the void, which explains the poor definition of the solvent molecules.

9_2 crystallized in the monoclinic space group $P2_1/c$. The crystal was a non-merohedral twin. Multiple domains were identified using the program CELL_NOW.²⁰ Data were integrated and scaled for each domain; however, only the first domain showed sufficient $I > \sigma$. Thus only data from this domain were used for the refinement. The asymmetric unit contained one molecule. The complex displayed disorder at the carbazole and diphenyl ether moieties of the ligand backbone. Both disorders were modeled across two positions. The main components refined to an occupancy of 77.8% and 90.1%, respectively. Several free acetonitrile and dichloromethane solvent molecules were found in the lattice, which were disordered and only poorly defined. SQUEEZE was used to handle this solvent disorder. Four solvent accessible voids were identified, each with a volume of 229 Å³. The voids are located at 0.151 0.679 0.023, -0.151 0.179 0.477, 0.151 0.821 0.523, and -0.151 0.321 0.977. The equivalent of 81 electrons was identified in the first two voids, voids 3 and 4 contained the equivalent of 80 electrons. This value corresponds to either two dichloromethane molecules (84 electrons), four acetonitrile molecules (88 electrons), or a combination of two acetonitrile molecules and one dichloromethane molecule (86 electrons) per void. Depending on the solvent composition, the filling of the voids is calculated to be 44.5%, 89.1%, and 66.8%, respectively.

[Fe₂(PIMIC6)(AnthCO₂)(MeCN)] (10) crystallized in the triclinic space group $P\bar{1}$ with two independent molecules in the asymmetric unit. The *tert*-butyl unit of one ligand molecule is disordered across two positions with the main component being occupied at 80.7%. The second ligand molecule displayed disorder at one 4-fluorophenolate unit and one benzyl ring. The disorder of the 4-fluorophenolate unit was modeled across two positions. The main component refined

to an occupancy of 74.0%. The disorder of the benzyl ring was modeled to three positions with occupancies of 80.4%, 7.2%, and 12.4%. The molecules of the metal complex were surrounded by several free solvent molecules in the lattice, which showed disorder across several positions and were only poorly defined. SQUEEZE was used to handle this disorder. One void was found, which was located at 0.000 0.500 0.000. The volume of the void was 1345 Å³ and thus provides room for approximately 79 non-hydrogen atoms. The equivalent of 342 electrons was identified, which allows for several combinations of free acetonitrile and THF solvent molecules. The amount of the solvent molecules hereby ranges from 0 to 15 acetonitrile and 0 to 8 THF molecules, respectively. This amount would approximately correspond to an 50-57% occupancy of the void.

[Fe₂(PIMIC6)(AnthCO₂)]·(CH₂Cl₂) (11) crystallized in the triclinic space group $P\bar{1}$ with two independent molecules in the asymmetric unit. The (CH₂)₆CO₂ unit of one of the molecules was disordered across two positions with the main component being occupied at 61.9%. The complex molecules were surrounded by several free dichloromethane and pentane solvent molecules in the lattice, which showed disorder across several positions and were only poorly defined. SQUEEZE was used to address this disorder. Two solvent accessible voids were identified, which were located at -0.173 0.261 0.209 and 0.173 0.739 0.791. The volume of these voids corresponds to 1201 and 1200 Å³ and equivalents of 296 and 295 electrons were identified, respectively. Given the fact that both dichloromethane and pentane have 42 electrons, the equivalent of 295-296 electrons would account for seven solvent molecules of either kind in the lattice. Depending on the nature of the solvent the occupancy of the void can be 30-50%.

[Fe₃O(HPIMIC4)₂(AnthCO₂)₂(MeCN)] (12) crystallized in the monoclinic space group $C2/c$ with one molecule in the asymmetric unit. The benzyl ether unit of the ligand backbone as well

as both of the *tert*-butyl units were disordered. The benzyl ether unit was modeled across three positions and the main component was refined to an occupancy of 49.7%. The occupancies of the minor components were refined to 36.0% and 14.3%. Disorder of one *tert*-butyl group was modeled across three positions with occupancies of 70.7%, 17.4%, and 12.0%, respectively. Disorder of the other *tert*-butyl group was modeled to two positions with the main component being occupied at 88.9%. The coordinated acetonitrile molecule is only half occupied and lies on a twofold rotation axis. Its occupancy was set to 0.250 to model the complete half occupied molecule. The occupancy of its hydrogen atoms was set to 0.125 to model the disorder of the symmetry-generated hydrogen atoms accordingly. The coordinated acetonitrile molecule was part of a complex disorder with several dichloromethane solvent molecules, which were modeled across four positions. The two main components of the dichloromethane disorder showed weak binding interactions with the iron center. The occupancy of chlorine atoms, which lie on the twofold rotation axis, was set to 0.5 to model the full molecules. A total of 1.5 solvent molecules (including the coordinated acetonitrile) occupied the free coordination site of the diiron site; however the exact composition of the disorder could not be resolved. The occupancies of the solvent molecules accordingly were restrained to unity with a standard deviation of 0. The free variables were hereby weighted differently to mirror the higher occupancy of the coordinated acetonitrile molecule, whose occupancy accordingly refined to 123% with regard to a total of 1.5 solvent molecules. The free coordination site of the second iron atom was occupied with $\frac{3}{4}$ of a dichloromethane molecule. The molecule displayed a complex disorder and was modeled across four positions with occupancies of 40.4%, 26.3%, 7.3%, and 5.2%. The least occupied part showed weak binding interactions with the diiron unit. The occupancies of the molecules were restrained to 0.75 with a standard deviation of 0, whereas the free variables were weighted differently. Sev-

eral free solvent molecules were found in the lattice, which were of only poor definition and showed a complex disorder. SQUEEZE was used to include a model of these disordered solvent molecules into the refinement model. Four solvent accessible voids were found, which were located at 0.250 -0.250 0.500, 0.250 0.250 1.000, 0.750 0.250 0.500, and 0.750 -0.250 1.000. The volume of each void was 346 Å³, which provides room for approximately 20 non-hydrogen atoms. The equivalent of 91 electrons was found within each void. This equivalent corresponds approximately to either two dichloromethane molecules (84 electrons) or one dichloromethane and two acetonitrile molecules (86 electrons). The occupancy of the voids thus would amount to 30-45%.

[Fe₄(μ-O)₂(μ-OH)₂(PIMIC4)₂] (13) crystallized in the triclinic space group $P\bar{1}$ with one molecule in the asymmetric unit. The diiron sites contain bridging hydroxyl ions. The coordinates of the hydroxyl hydrogen atom was taken from the Fourier synthesis. Identification of the bridging oxygen species based on the analysis of the Fourier synthesis alone was not possible, because several Q-peaks were observed close to O7. The bridging oxygen species was subsequently determined based on the oxidation state assignment of the iron ions. Both ions were determined to be Fe(III) (see Table S5 for oxidation state assignment). In order to generate a charge balanced model the bridging oxygen species had to be charged negatively and thus OH⁻. The oxygen-hydrogen distance was restrained to ideal values using the DFIX command in SHELXL.¹⁵ Several free solvent molecules were found in the lattice of the crystal. Only one acetonitrile molecule was comparatively well defined and included in the refinement model. SQUEEZE was used to handle the disorder of other poorly defined solvent molecules. One void with a volume of 433 Å³ was identified, which provides room for approximately 25 non-hydrogen atoms. The void is located at 0.500 1.000 0.000 and includes the equivalent of 108 electrons. This value corresponds

exactly to one dichloromethane and three acetonitrile molecules (108 electrons). The occupancy of the void accordingly was 50%, which accounts for the poor definition of the solvent molecules. **[Fe₂(F₂PIM)(AnthCO₂)₂(THF)] (14)** crystallized in the triclinic space group $P\bar{1}$ with two independent molecules per asymmetric unit. The ligand of one complex molecule displays disorder at one fluorophenolate unit and a part of the benzyl ether fluorophenolate backbone. In addition, the coordinated THF molecule is disordered. All disorders were modeled independently across two positions. The main occupied components of the fluorophenolate unit, ligand backbone and coordinated THF molecules refined to 60.9%, 79.6%, and 70.4%, respectively. More than half of the ligand of the second complex molecule in the asymmetric unit was disordered across two positions. The main component refined to an occupancy of 74.0%. In addition, the coordinated anthracene carboxylate and the coordinated THF molecule displayed whole molecule disorder with the main component occupied at 70.8% and 67.0%, respectively.

Several free, poorly defined solvent dichloromethane and THF molecules were found in the lattice. SQUEEZE was used to include this solvent disorder in the refinement model. One solvent accessible void was identified by SQUEEZE, which was located at 0.000 0.006 0.477. The volume of this void was 1135 Å³ and contained the equivalent of 310 electrons. This equivalent allows for approximately 7-8 dichloromethane and/or THF solvent molecules (both solvent molecules have 42 electrons). Because the exact ratio of the solvent molecules is unknown, a 36-60% occupancy of the void was estimated.

[Fe₂(F₂PIM)(Ph₃CCO₂)₂] (15) crystallized in the triclinic space group $P\bar{1}$ with one molecule per asymmetric unit. A part of the benzyl ether unit was disordered and accordingly modeled across two positions. The main component refined to an occupancy of 88.0%. The disorder of the ether group was not resolved well. In the C₆H₄CH₂O unit, the CH₂ carbon atom of the minor occupied

part does not lie in the same plane of the phenyl ring. An unreasonably strong set of restraints would, however, be necessary to force all atoms into the same plane. Thus the bond angle was not corrected in the refinement model at hand. In addition, one of the coordinated triphenyl acetate units displayed a whole molecule disorder and was modeled across three positions. The occupancies of the components refined to 51.4%, 24.3%, and 24.3%. Several free toluene solvent molecules were present in the lattice, which were poorly defined and disordered. SQUEEZE was used to handle this disorder. One void of 1393 Å³, which would allow for a maximum of 82 non-hydrogen atoms, was identified. It was located at -0.005 0.000 0.009. The equivalent of 364 electrons was identified, which corresponds to approximately seven toluene molecules (350 electrons). The molecules occupy approximately 60% of the void, which accounts for their poor definition.

[Fe₂(PIMIC4)(*o*-Ph₂PC₆H₄CO₂)(MeCN)] (16) crystallized in the triclinic space group $P\bar{1}$ with one molecule per asymmetric unit. Several poorly defined free acetonitrile solvent molecules were found in the lattice. SQUEEZE was used to handle this solvent disorder. Three solvent accessible voids were found, among which only one was of reasonable size. This void was located at 0.053 0.031 0.500 and had a volume of 830 Å³, which is enough room for approximately 49 non-hydrogen atoms. The equivalent of 200 electrons was identified within the void. This equivalent corresponds nearly exactly to nine acetonitrile molecules (198 electrons), which would occupy a room of 459 Å³ and thus only 55% of the void.

[Fe₂(PIMIC4)(*o*-PhSC₆H₄CO₂)(MeCN)] (17) crystallized in the monoclinic space group $P2_1/c$ with one molecule in the asymmetric unit. The carboxylated phenylsulfide ligand as well as one methyl group of the ligand systems were refined across two positions with the main component being occupied at 62.4% and 52.0%, respectively.

[Fe₂(PIMIC4)(*o*-Ph₂CHC₆H₄CO₂)(MeCN)] (18) crystallized in the triclinic space group $P\bar{1}$ with one molecule of the complex in the asymmetric unit. The ligand displayed disorder at one *tert*-butyl group as well as at one fluorophenolate unit. The disorder of the *tert*-butyl group was modeled across two positions with the main component occupied at 76.6%. The disorder of the fluorophenolate group was modeled across three positions with occupancies of 27.4%, 39.9%, and 32.7%, respectively. Two disordered and poorly defined acetonitrile solvent molecules were found in the lattice. Each was modeled across three positions and their occupancies were restrained to 2.0. The individual occupancies hereby refined to 47.2%, 31.0%, 20.5%, 30.8%, 24.3%, and 46.2%.

Table S1. X-ray Crystallographic Data for Compounds **6-9_1** at 100 K.

	6	7	8	9_1
Empirical formula	C ₁₆₂ H ₁₃₂ F ₄ Fe ₄ N ₈ O ₁₄	C ₈₂ H ₆₈ F ₂ Fe ₂ N ₄ O ₇	C ₈₉ H ₇₇ F ₂ Fe ₂ N ₅ O ₇	C ₈₃ H ₇₀ F ₂ Fe ₂ N ₄ O ₇
Formula weight	2714.15	1371.10	1478.25	1385.13
Crystal system	Triclinic	Monoclinic	Triclinic	Triclinic
Space group	<i>P</i> $\bar{1}$	<i>P</i> 2 ₁ / <i>c</i>	<i>P</i> $\bar{1}$	<i>P</i> $\bar{1}$
a, Å	16.950(6)	11.022(3)	12.535(3)	19.962(5)
b, Å	18.909(6)	20.367(6)	14.274(4)	20.378(6)
c, Å	31.846(10)	33.243(9)	21.617(5)	22.652(6)
α, °	79.467(5)	90	77.300(6)	85.646(4)
β, °	81.223(5)	94.748(5)	75.942(6)	64.670(4)
γ, °	65.873(5)	90	79.231(7)	80.702(4)
Volume, Å³	9124(5)	7437(4)	3623.6(15)	8219(4)
Z	2	4	2	4
ρ_{calcd}, g/cm³	0.988	1.225	1.355	1.119
μ, mm⁻¹	0.367	0.450	0.468	0.408
θ range, °	1.524 to 24.872	1.585 to 25.350	1.477 to 29.585	1.630 to 25.133
Completeness to θ, %	98.7	98.4	99.9	98.7
Reflections collected	31232	79555	78173	123034
Independent reflections	-	13255	20065	29030
R(int)	-	0.0839	0.0395	0.0690
Restraints	3696	1084	400	1833
Parameters	1846	990	998	1819
Min, max transmission	0.6052, 0.7452	0.6258, 0.7425	0.6348, 0.7452	0.6526, 0.7452
R1 (wR2) [<i>I</i> > 2σ(<i>I</i>)]	0.0938 (0.2438)	0.0500 (0.1224)	0.0510 (0.1316)	0.1174 (0.3352)
R1 (wR2)	0.1264 (0.2713)	0.0752 (0.1353)	0.0748 (0.1466)	0.1561 (0.3631)
Goodness-of-fit on <i>F</i>²	1.022	1.024	1.022	1.074
Max, min peaks, e/Å³	1.206 and -0.903	0.491 and -0.418	0.686 and -0.820	2.274 and -0.800

Table S2. X-ray Crystallographic Data for Compounds **9_2-12** at 100 K.

	9_2	10	11	12
Empirical formula	C ₈₃ H ₇₀ F ₂ Fe ₂ N ₄ O ₇	C ₁₆₈ H ₁₄₄ F ₄ Fe ₄ N ₈ O ₁₄	C ₈₃ H ₇₁ Cl ₂ F ₂ Fe ₂ N ₅ O ₇	C _{163.57} H _{137.62} Cl _{4.45} F ₄ Fe ₃ N _{6.62} O ₁₅
Formula weight	1385.13	2798.30	1443.02	2837.18
Crystal system	Monoclinic	Triclinic	Triclinic	Monoclinic
Space group	<i>P</i> 2 ₁ / <i>c</i>	<i>P</i> $\bar{1}$	<i>P</i> $\bar{1}$	<i>C</i> 2/ <i>c</i>
a, Å	10.963(2)	20.197(6)	19.411(4)	41.357(5)
b, Å	20.623(5)	20.961(6)	20.626(4)	19.045(2)
c, Å	32.827(7)	21.727(6)	22.103(5)	21.273(3)
α, °	90	115.348(4)	83.965(3)	90
β, °	96.403(4)	96.887(4)	80.777(3)	117.909(2)
γ, °	90	106.251(5)	83.934(3)	90
Volume, Å³	7375(3)	7670(4)	8651(3)	14807(3)
Z	4	2	4	4
ρ_{calcd}, g/cm³	1.247	1.212	1.108	1.273
μ, mm⁻¹	0.455	0.438	0.450	0.440
θ range, °	1.168 to 26.373	1.485 to 25.374	1.310 to 18.882	1.436 to 25.081
Completeness to θ, %	99.9	99.0	98.6	99.5
Reflections collected	15088	96690	71585	97530
Independent reflections	15088	27542	13506	13096
R(int)	-----	0.1048	0.0983	0.1124
Restraints	1437	1117	2481	2518
Parameters	1060	1992	1797	1395
Min, max transmission	0.5114, 0.7457	0.5769, 0.7452	0.5742, 0.7452	0.6425/0.7450
R1 (wR2) [<i>I</i> > 2σ(<i>I</i>)]	0.0583 (0.1361)	0.0920 (0.2463)	0.0761 (0.1836)	0.0581 (0.1227)
R1 (wR2)	0.0887 (0.1484)	0.1566 (0.2905)	0.1147 (0.2081)	0.1040 (0.1425)
Goodness-of-fit on <i>F</i>²	1.077	1.037	1.070	1.041
Max, min peaks, e/Å³	0.817 and -0.589	1.781 and -1.228	0.854 and -0.632	0.758 and -0.601

Table S3. X-ray Crystallographic Data for Compounds **13-16** at 100 K.

	13	14	15	16
Empirical formula	C ₁₃₄ H ₁₂₀ F ₄ Fe ₄ N ₈ O ₁₄	C ₇₄ H ₅₂ F ₂ Fe ₂ N ₂ O ₁₀ S	C ₈₀ H ₅₆ F ₂ Fe ₂ N ₂ O ₉ S	C ₈₆ H ₇₃ F ₂ Fe ₂ N ₄ O ₇ P
Formula weight	2365.77	1310.93	1371.02	1455.15
Crystal system	Triclinic	Triclinic	Triclinic	Triclinic
Space group	<i>P</i> $\bar{1}$	<i>P</i> $\bar{1}$	<i>P</i> $\bar{1}$	<i>P</i> $\bar{1}$
a, Å	12.710(3)	16.873(2)	13.889(3)	15.490(4)
b, Å	13.856(3)	18.258(3)	17.155(3)	17.224(4)
c, Å	18.821(4)	23.754(3)	18.946(4)	18.421(4)
α, °	96.69(3)	90.686(2)	90.82(3)	91.857(4)
β, °	91.98(3)	108.724(2)	106.31(3)	111.043(4)
γ, °	110.53(3)	105.256(2)	102.49(3)	113.776(4)
Volume, Å³	3072.6(12)	6648.9(16)	4216.5(17)	4106.5(17)
Z	1	4	2	2
ρ_{calcd}, g/cm³	1.279	1.310	1.080	1.177
μ, mm⁻¹	0.534	0.533	0.422	0.430
θ range, °	1.584 to 25.988	1.334 to 27.924	1.570 to 27.881	1.540 to 29.588
Completeness to θ, %	99.9	99.9	99.9	100.0
Reflections collected	51177	127160	79923	80238
Independent reflections	12028	31448	19856	20263
R(int)	0.0959	0.0523	0.0361	0.0809
Restraints	1	7235	2063	12
Parameters	740	2251	1099	927
Min, max transmission	0.6681, 0.7453	0.6866, 0.7456	0.6124, 0.7456	0.5248, 0.7458
R1 (wR2) [$I > 2\sigma(I)$]	0.0556 (0.1168)	0.0447 (0.1002)	0.0357 (0.0872)	0.0677 (0.1838)
R1 (wR2)	0.1072 (0.1359)	0.0869 (0.1179)	0.0523 (0.0950)	0.1094 (0.2155)
Goodness-of-fit on F^2	1.012	1.009	1.041	1.050
Max, min peaks, e/Å³	0.919 and -0.859	0.673 and -0.860	0.455 and -0.459	2.018 and -1.202

Table S4. X-ray Crystallographic Data for Compounds **17-18** at 100 K.

	17	18
Empirical formula	C ₈₀ H ₆₈ F ₂ Fe ₂ N ₄ O ₇ S	C ₉₁ H ₈₀ F ₂ Fe ₂ N ₆ O ₇
Formula weight	1379.14	1519.13
Crystal system	Monoclinic	Triclinic
Space group	<i>P</i> 2 ₁ / <i>c</i>	<i>P</i> $\bar{1}$
a, Å	14.2878(10)	12.0561(16)
b, Å	41.874(3)	17.553(2)
c, Å	11.0297(8)	19.198(3)
α, °	90	109.430(2)
β, °	92.3670(10)	90.010(2)
γ, °	90	92.686(2)
Volume, Å³	6593.3(8)	3826.6(9)
Z	4	2
ρ_{calcd}, g/cm³	1.389	1.319
μ, mm⁻¹	0.539	0.446
θ range, °	1.426 to 26.391	1.691 to 29.628
Completeness to θ, %	100.0	99.9
Reflections collected	114590	82844
Independent reflections	13480	21219
R(int)	0.0556	0.0293
Restraints	734	608
Parameters	1021	1134
Min, max transmission	0.6831, 0.7454	0.6862, 0.7459
R1 (wR2) [<i>I</i> > 2σ(<i>I</i>)]	0.0476 (0.1053)	0.0377 (0.0971)
R1 (wR2)	0.0597 (0.1113)	0.0475 (0.1038)
Goodness-of-fit on <i>F</i>²	1.123	1.034
Max, min peaks, e/Å³	0.934 and -0.515	0.740 and -0.441

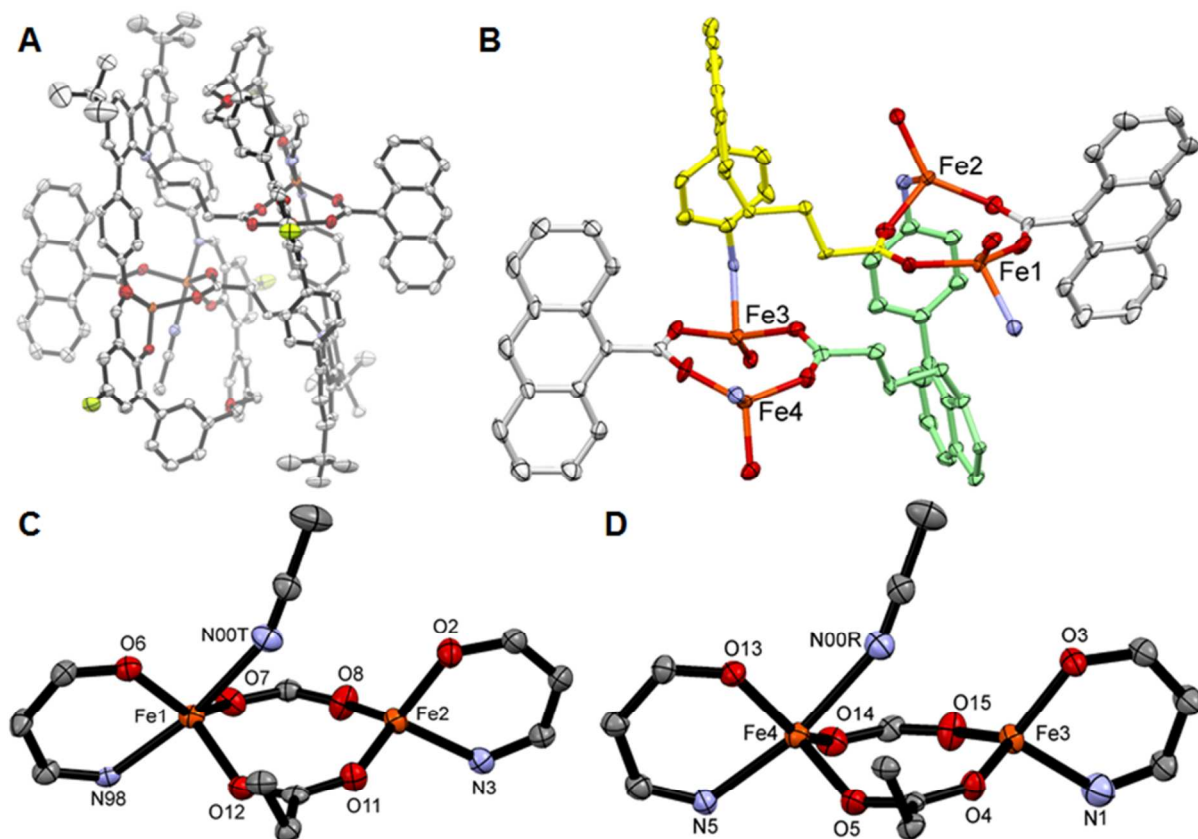


Figure S1. A. X-ray crystal structure of $[\text{Fe}_2(\text{PIMIC3})(\text{AnthCO}_2)(\text{MeCN})]_2$ (**6**) in ORTEP representation at 50% probability. H atoms were omitted for clarity. B. Isolated view of the dimer illustrating the intermolecular bridging by aliphatic carboxylate chains. C and D. Isolated view of the diiron cores, in which the carboxylate behind the Fe-Fe vector is the external carboxylate ligand. Color scheme: iron, orange; carbon, white (in A and B) and gray (in C and D); nitrogen, blue; oxygen, red; fluorine, green. Selected bond distances (\AA) and angles ($^\circ$): In C: $\text{Fe}(1)\cdots\text{Fe}(2) = 4.026(2)$; $\text{Fe}(1)\text{--O}(6) = 1.936(4)$; $\text{Fe}(1)\text{--O}(7) = 2.041(4)$; $\text{Fe}(1)\text{--O}(12) = 1.999(4)$; $\text{Fe}(1)\text{--N}(98) = 2.147(5)$; $\text{Fe}(1)\text{--N}(00\text{T}) = 2.276(6)$; $\text{Fe}(2)\text{--O}(2) = 1.908(4)$; $\text{Fe}(2)\text{--O}(8) = 1.961(4)$; $\text{Fe}(2)\text{--O}(11) = 1.984(4)$; $\text{Fe}(2)\text{--N}(3) = 2.070(5)$; $\text{Fe}(2)\text{--N}(00\text{T}) = 3.137(9)$; $\text{O}(7)\text{--Fe}(1)\text{--O}(12) = 111.37(19)$; $\text{O}(6)\text{--Fe}(1)\text{--N}(98) = 87.13(18)$; $\text{O}(8)\text{--Fe}(2)\text{--O}(11) = 118.17(19)$; $\text{O}(2)\text{--Fe}(2)\text{--N}(3) = 90.96(19)$. In D: $\text{Fe}(3)\cdots\text{Fe}(4) = 3.993(2)$; $\text{Fe}(3)\text{--O}(3) = 1.921(4)$; $\text{Fe}(3)\text{--O}(4) = 1.974(4)$; $\text{Fe}(3)\text{--O}(15) = 1.983(4)$; $\text{Fe}(3)\text{--N}(1) = 2.074(5)$; $\text{Fe}(3)\text{--N}(00\text{R}) = 3.078(6)$; $\text{Fe}(4)\text{--O}(5) = 2.003(4)$; $\text{Fe}(4)\text{--O}(13) = 1.928(4)$; $\text{Fe}(4)\text{--O}(14) = 2.016(4)$; $\text{Fe}(4)\text{--N}(5) = 2.139(5)$; $\text{Fe}(4)\text{--N}(00\text{R}) = 2.287(6)$; $\text{O}(4)\text{--Fe}(3)\text{--O}(15) = 120.43(18)$; $\text{O}(3)\text{--Fe}(3)\text{--N}(1) = 90.89(19)$; $\text{O}(5)\text{--Fe}(4)\text{--O}(14) = 109.92(17)$; $\text{O}(13)\text{--Fe}(4)\text{--N}(5) = 86.12(18)$.

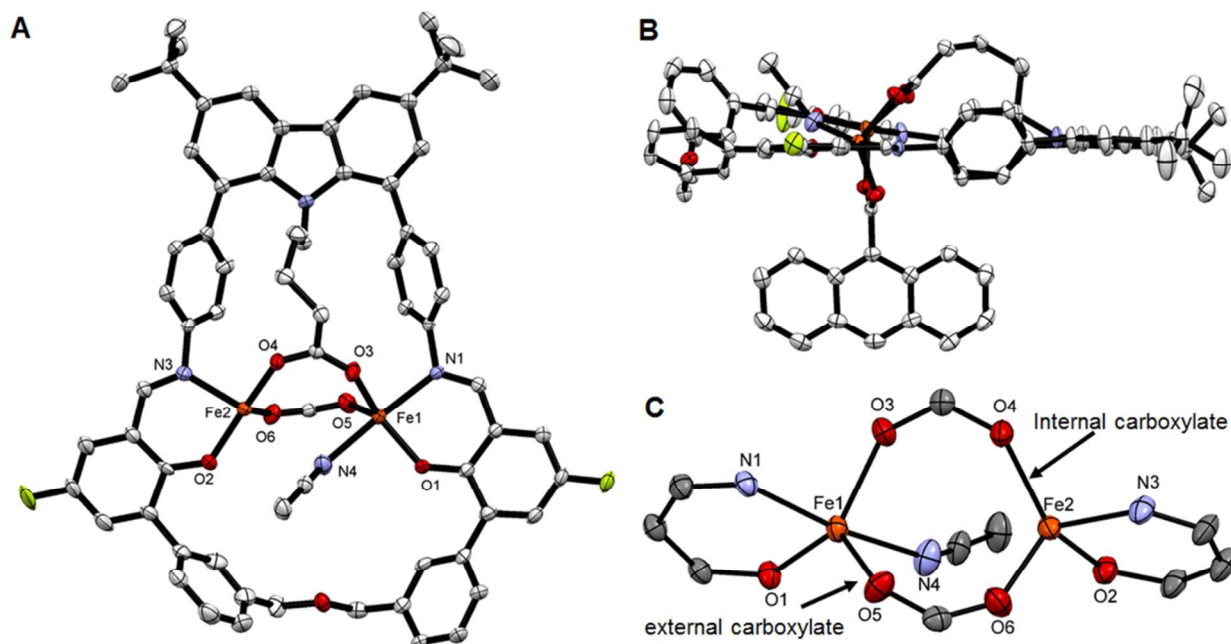


Figure S2. A. X-ray crystal structure of $[\text{Fe}_2(\text{PIMIC4})(\text{AnthCO}_2)(\text{MeCN})]$ (**7**) in ORTEP representation at 50% probability. H atoms and the anthracene ring were omitted for clarity. B. Side view of the X-ray crystal structure of $[\text{Fe}_2(\text{PIMIC4})(\text{AnthCO}_2)(\text{MeCN})]$ in ORTEP representation at 50% probability. C. Isolated view of the diiron cores. Color scheme: iron, orange; carbon, white (in A and B) and gray (in C); nitrogen, blue; oxygen, red; fluorine, green. Selected bond distances (\AA) and angles ($^\circ$): $\text{Fe}(1)\cdots\text{Fe}(2) = 3.972(1)$; $\text{Fe}(1)\text{--O}(1) = 1.9335(18)$; $\text{Fe}(1)\text{--O}(3) = 2.019(2)$; $\text{Fe}(1)\text{--O}(5) = 2.022(2)$; $\text{Fe}(1)\text{--N}(1) = 2.140(2)$; $\text{Fe}(1)\text{--N}(4) = 2.261(3)$; $\text{Fe}(2)\text{--O}(2) = 1.9163(19)$; $\text{Fe}(2)\text{--O}(4) = 1.991(2)$; $\text{Fe}(2)\text{--O}(6) = 1.983(2)$; $\text{Fe}(2)\text{--N}(3) = 2.067(2)$; $\text{Fe}(2)\text{--N}(4) = 2.887(3)$; $\text{O}(3)\text{--Fe}(1)\text{--O}(5) = 105.13(9)$; $\text{O}(1)\text{--Fe}(1)\text{--N}(1) = 86.40(8)$; $\text{O}(4)\text{--Fe}(2)\text{--O}(6) = 109.67(9)$; $\text{O}(2)\text{--Fe}(2)\text{--N}(3) = 89.45(9)$.

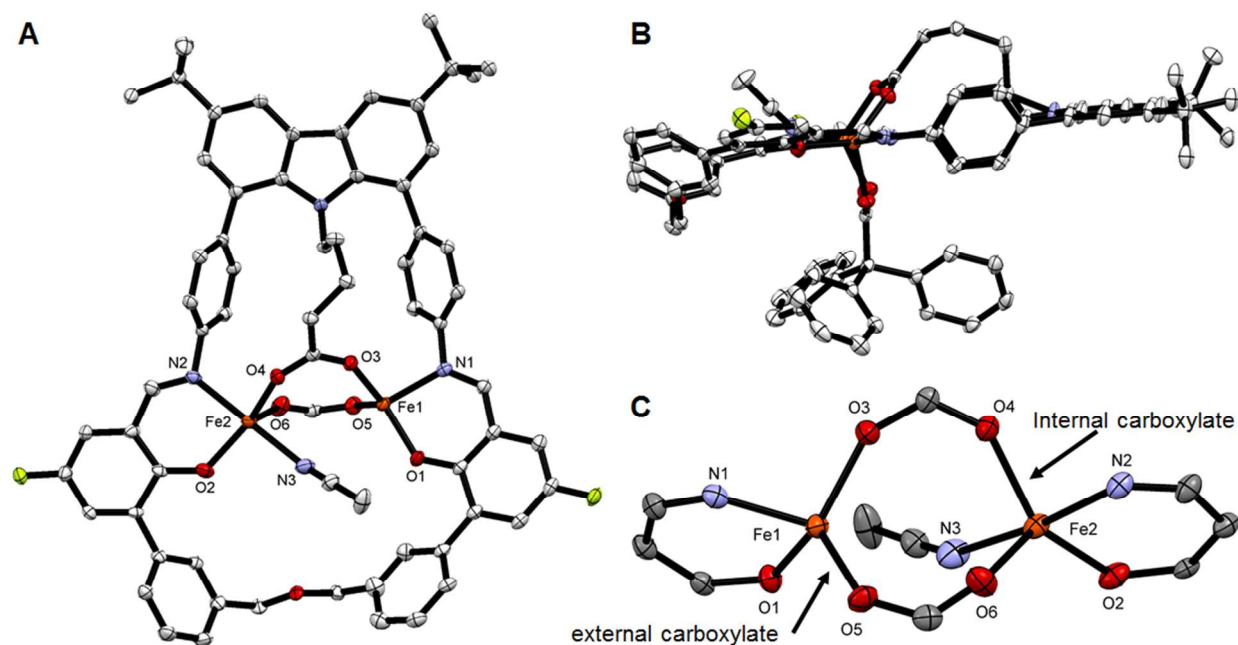


Figure S3. A. X-ray crystal structure of $[\text{Fe}_2(\text{PIMIC4})(\text{Ph}_3\text{CCO}_2)(\text{MeCN})]$ (**8**) in ORTEP representation at 50% probability. H atoms, the anthracene ring, and non-coordinated acetonitrile were omitted for clarity. B. Side view of the X-ray crystal structure of $[\text{Fe}_2(\text{PIMIC4})(\text{Ph}_3\text{CCO}_2)(\text{MeCN})]$ in ORTEP representation at 50% probability. C. Isolated view of the diiron cores. Color scheme: iron, orange; carbon, white (in A and B) and gray (in C); nitrogen, blue; oxygen, red; fluorine, green. Selected bond distances (\AA) and angles ($^\circ$): $\text{Fe}(1)\cdots\text{Fe}(2) = 4.0560(9)$; $\text{Fe}(1)\text{--O}(1) = 1.9270(15)$; $\text{Fe}(1)\text{--O}(3) = 1.9749(16)$; $\text{Fe}(1)\text{--O}(5) = 1.9918(16)$; $\text{Fe}(1)\text{--N}(1) = 2.0692(19)$; $\text{Fe}(1)\text{--N}(3) = 3.122(2)$; $\text{Fe}(2)\text{--O}(2) = 1.976(9)$; $\text{Fe}(2)\text{--O}(4) = 2.0275(16)$; $\text{Fe}(2)\text{--O}(6) = 2.0155(17)$; $\text{Fe}(2)\text{--N}(2) = 2.1339(19)$; $\text{Fe}(2)\text{--N}(3) = 2.201(2)$; $\text{O}(3)\text{--Fe}(1)\text{--O}(5) = 109.17(7)$; $\text{O}(1)\text{--Fe}(1)\text{--N}(1) = 88.05(7)$; $\text{O}(4)\text{--Fe}(2)\text{--O}(6) = 100.48(7)$; $\text{O}(2)\text{--Fe}(2)\text{--N}(2) = 86.21(7)$.

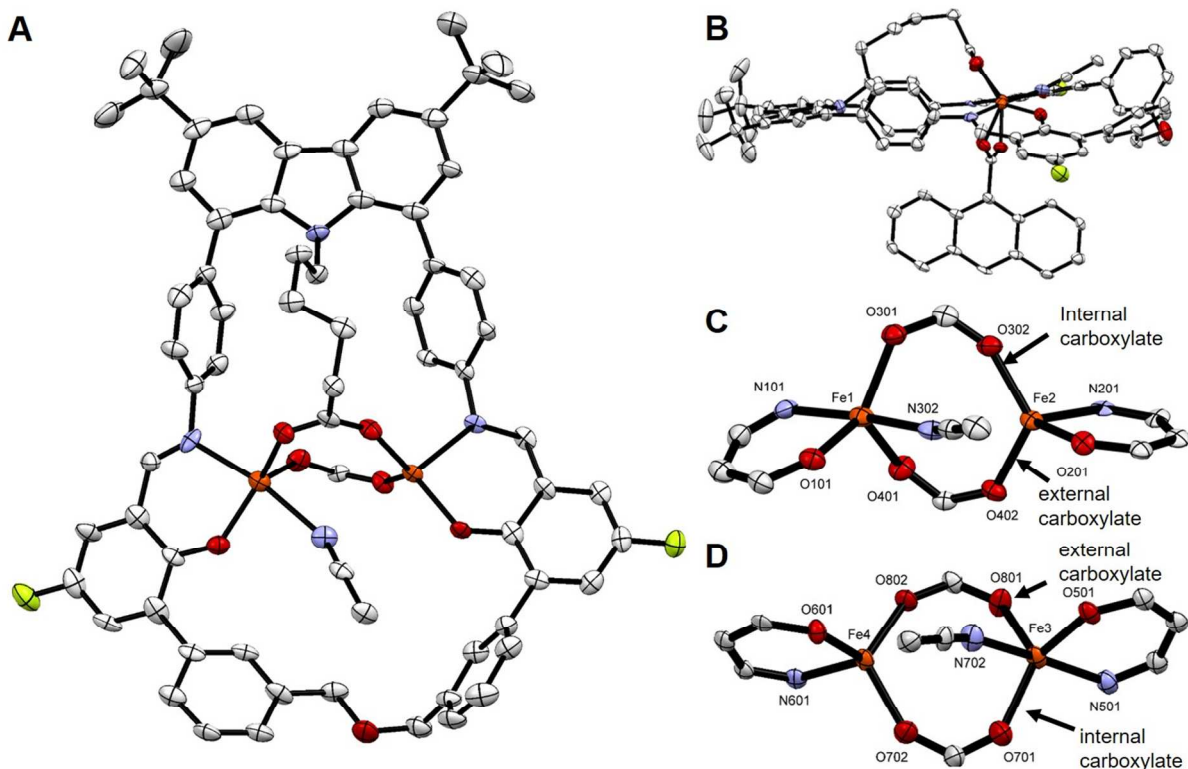


Figure S4. A. X-ray crystal structure of $[\text{Fe}_2(\text{PIMIC5})(\text{AnthCO}_2)(\text{MeCN})]$ (**9_1**) in ORTEP representation at 50% probability. There are two independent molecules of the complex in the asymmetric unit. Only one of them is illustrated. H atoms and the anthracene ring were omitted for clarity. B. Side view of the X-ray crystal structure of $[\text{Fe}_2(\text{PIMIC5})(\text{AnthCO}_2)(\text{MeCN})]$ in ORTEP representation at 50% probability. C and D. Isolated view of the diiron cores of the two independent molecules. Color scheme: iron, orange; carbon, white; nitrogen, blue; oxygen, red; fluorine, green. Selected bond distances (\AA) and angles ($^\circ$): In C: $\text{Fe}(1)\cdots\text{Fe}(2) = 3.894(3)$; $\text{Fe}(1)\text{--O}(101) = 1.939(6)$; $\text{Fe}(1)\text{--O}(301) = 2.024(6)$; $\text{Fe}(1)\text{--O}(401) = 2.036(6)$; $\text{Fe}(1)\text{--N}(101) = 2.134(7)$; $\text{Fe}(1)\text{--N}(302) = 2.281(8)$; $\text{Fe}(2)\text{--O}(201) = 1.926(6)$; $\text{Fe}(2)\text{--O}(302) = 1.976(6)$; $\text{Fe}(2)\text{--O}(402) = 2.008(6)$; $\text{Fe}(2)\text{--N}(201) = 2.076(7)$; $\text{Fe}(2)\text{--N}(302) = 2.845(1)$; $\text{O}(301)\text{--Fe}(1)\text{--O}(401) = 107.3(3)$; $\text{O}(101)\text{--Fe}(1)\text{--N}(101) = 86.2(3)$; $\text{O}(302)\text{--Fe}(2)\text{--O}(402) = 115.1(3)$; $\text{O}(201)\text{--Fe}(2)\text{--N}(201) = 90.3(3)$. In D: $\text{Fe}(3)\cdots\text{Fe}(4) = 4.066(3)$; $\text{Fe}(3)\text{--O}(501) = 1.943(6)$; $\text{Fe}(3)\text{--O}(701) = 1.985(7)$; $\text{Fe}(3)\text{--O}(801) = 2.058(6)$; $\text{Fe}(3)\text{--N}(501) = 2.151(8)$; $\text{Fe}(3)\text{--N}(702) = 2.236(8)$; $\text{Fe}(4)\text{--O}(601) = 1.916(6)$; $\text{Fe}(4)\text{--O}(702) = 1.968(7)$; $\text{Fe}(4)\text{--O}(802) = 1.971(6)$; $\text{Fe}(4)\text{--N}(601) = 2.060(7)$; $\text{Fe}(4)\text{--N}(702) = 3.167(1)$; $\text{O}(701)\text{--Fe}(3)\text{--O}(801) = 111.2(3)$; $\text{O}(501)\text{--Fe}(3)\text{--N}(501) = 86.9(3)$; $\text{O}(702)\text{--Fe}(4)\text{--O}(802) = 113.3(3)$; $\text{O}(601)\text{--Fe}(4)\text{--N}(601) = 91.5(3)$.

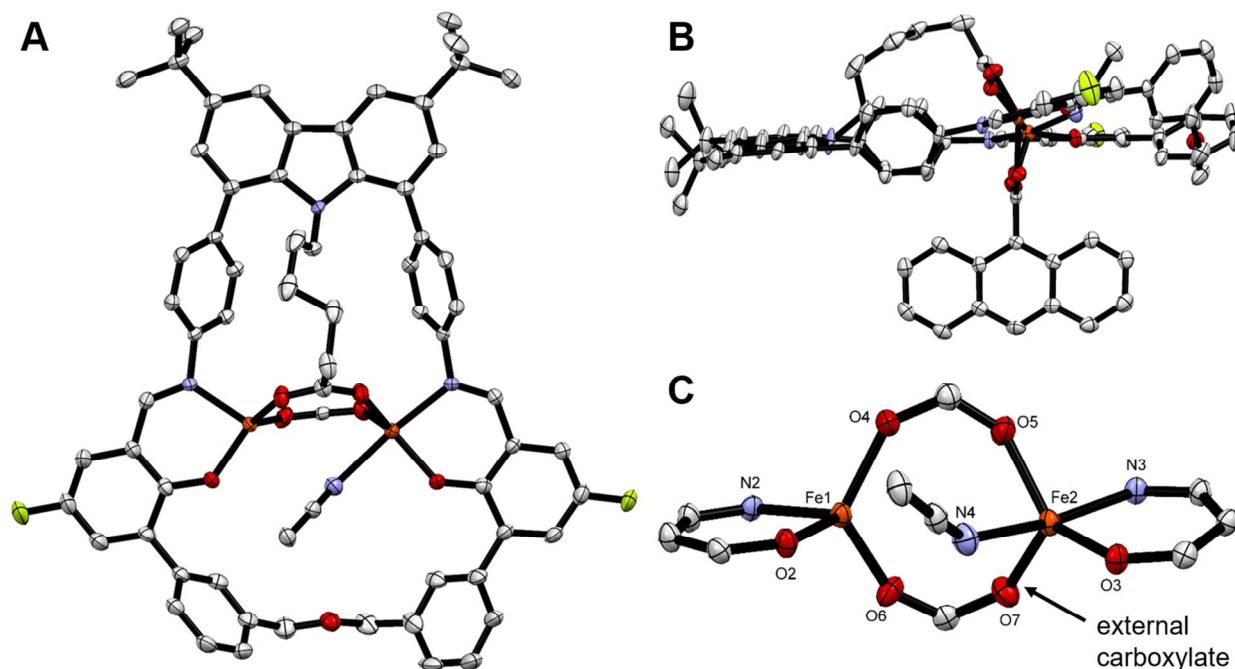


Figure S5. A. X-ray crystal structure of $[\text{Fe}_2(\text{PIMIC5})(\text{AnthCO}_2)(\text{MeCN})]$ (**9_2**) in ORTEP representation at 50% probability. H atoms and the anthracene ring were omitted for clarity. B. Side view of the X-ray crystal structure of $[\text{Fe}_2(\text{PIMIC5})(\text{AnthCO}_2)(\text{MeCN})]$ in ORTEP representation at 50% probability. C. Isolated view of the diiron core. Color scheme: iron, orange; carbon, white; nitrogen, blue; oxygen, red; fluorine, green. Selected bond distances (\AA) and angles ($^\circ$): $\text{Fe}(1)\cdots\text{Fe}(2) = 4.007(6)$; $\text{Fe}(1)\text{--O}(2) = 1.9087(19)$; $\text{Fe}(1)\text{--O}(4) = 1.982(2)$; $\text{Fe}(1)\text{--O}(6) = 1.964(2)$; $\text{Fe}(1)\text{--N}(2) = 2.068(2)$; $\text{Fe}(2)\text{--N}(4) = 2.292(3)$; $\text{Fe}(2)\text{--O}(3) = 1.925(2)$; $\text{Fe}(2)\text{--O}(5) = 1.999(2)$; $\text{Fe}(2)\text{--O}(7) = 2.004(2)$; $\text{Fe}(2)\text{--N}(3) = 2.136(2)$; $\text{Fe}(1)\text{--N}(4) = 2.953(9)$; $\text{O}(4)\text{--Fe}(1)\text{--O}(6) = 116.08(9)$; $\text{O}(2)\text{--Fe}(1)\text{--N}(2) = 89.85(9)$; $\text{O}(5)\text{--Fe}(2)\text{--O}(7) = 107.33(9)$; $\text{O}(3)\text{--Fe}(2)\text{--N}(3) = 86.57(9)$.

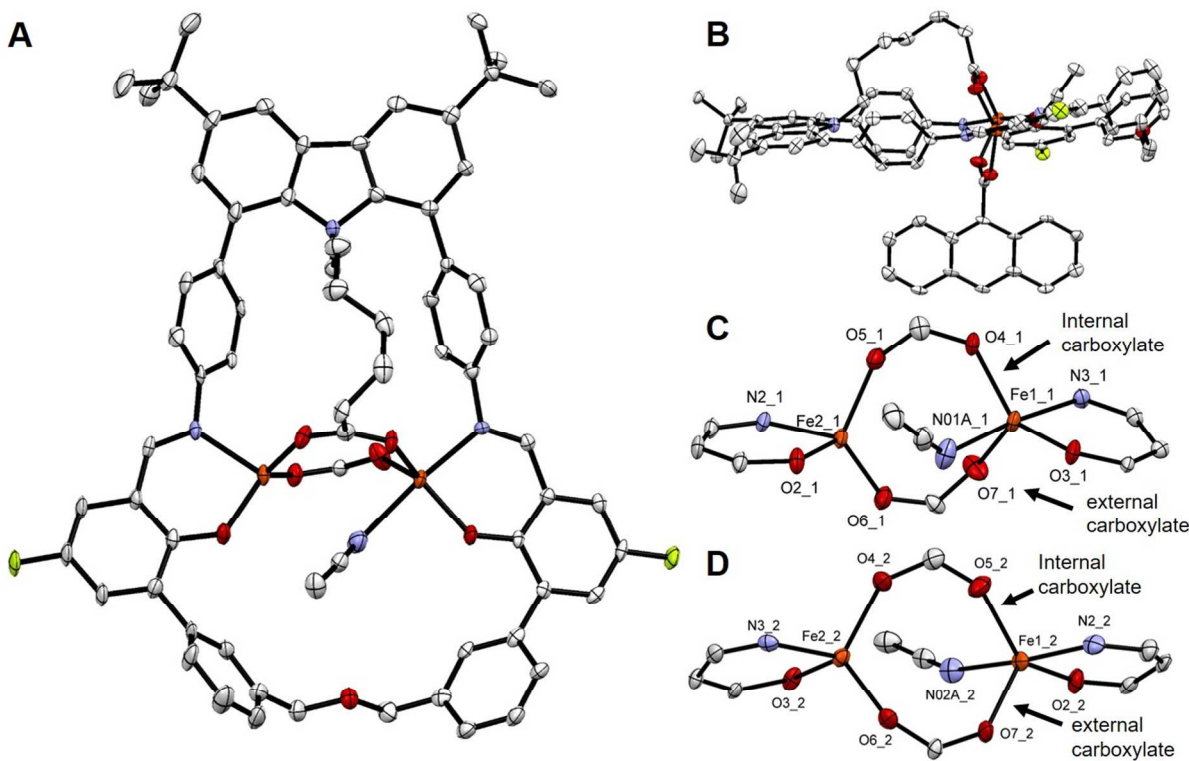


Figure S6. A. X-ray crystal structure of $[\text{Fe}_2(\text{PIMIC6})(\text{AnthCO}_2)(\text{MeCN})]$ (**10**) in ORTEP representation at 50% probability. There are two independent molecules of the complex in the asymmetric unit. Only one of them is illustrated. H atoms and the anthracene ring were omitted for clarity. B. Side view of the X-ray crystal structure of $[\text{Fe}_2(\text{PIMIC6})(\text{AnthCO}_2)(\text{MeCN})]$ in ORTEP representation at 50% probability. C and D. Isolated view of the diiron cores of the two independent molecules. Color scheme: iron, orange; carbon, white; nitrogen, blue; oxygen, red; fluorine, green. Selected bond distances (\AA) and angles ($^\circ$): In C: $\text{Fe}(1)\cdots\text{Fe}(2) = 4.064(2)$; $\text{Fe}(1)\text{--O}(2) = 1.924(4)$; $\text{Fe}(1)\text{--O}(5) = 1.997(4)$; $\text{Fe}(1)\text{--O}(7) = 2.022(4)$; $\text{Fe}(1)\text{--N}(2) = 2.151(6)$; $\text{Fe}(1)\text{--N}(02a) = 2.244(6)$; $\text{Fe}(2)\text{--O}(3) = 1.893(4)$; $\text{Fe}(2)\text{--O}(6) = 1.963(4)$; $\text{Fe}(2)\text{--O}(4) = 1.964(4)$; $\text{Fe}(2)\text{--N}(3) = 2.057(5)$; $\text{Fe}(2)\text{--N}(02a) = 3.128(7)$; $\text{O}(5)\text{--Fe}(1)\text{--O}(7) = 111.66(19)$; $\text{O}(2)\text{--Fe}(1)\text{--N}(2) = 88.37(19)$; $\text{O}(6)\text{--Fe}(2)\text{--O}(4) = 113.02(18)$; $\text{O}(3)\text{--Fe}(2)\text{--N}(3) = 90.42(18)$. In D: $\text{Fe}(1)\cdots\text{Fe}(2) = 3.956(2)$; $\text{Fe}(1)\text{--O}(3) = 1.909(4)$; $\text{Fe}(1)\text{--O}(4) = 1.983(5)$; $\text{Fe}(1)\text{--O}(7) = 2.000(5)$; $\text{Fe}(1)\text{--N}(3) = 2.106(5)$; $\text{Fe}(1)\text{--N}(01a) = 2.304(6)$; $\text{Fe}(2)\text{--O}(2) = 1.908(4)$; $\text{Fe}(2)\text{--O}(5) = 1.958(5)$; $\text{Fe}(2)\text{--O}(6) = 1.987(5)$; $\text{Fe}(2)\text{--N}(2) = 2.065(5)$; $\text{Fe}(2)\text{--N}(01a) = 2.959(9)$; $\text{O}(4)\text{--Fe}(1)\text{--O}(7) = 109.2(2)$; $\text{O}(3)\text{--Fe}(1)\text{--N}(3) = 87.88(18)$; $\text{O}(5)\text{--Fe}(2)\text{--O}(6) = 116.2(2)$; $\text{O}(2)\text{--Fe}(2)\text{--N}(2) = 90.38(19)$.

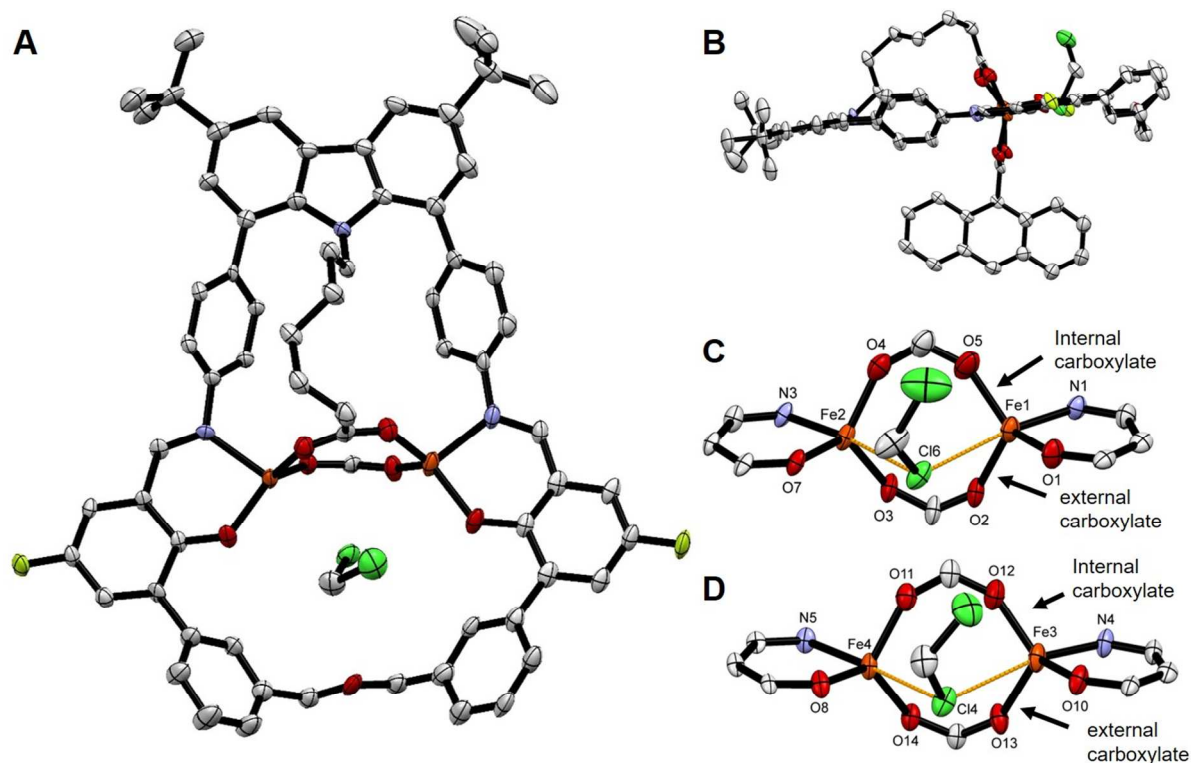


Figure S7. A. X-ray crystal structure of $[\text{Fe}_2(\text{PIMIC6})(\text{AnthCO}_2)] \cdot (\text{CH}_2\text{Cl}_2)$ (**11**) in ORTEP representation at 50% probability. There are two independent molecules of the complex in the asymmetric unit. Only one of them is illustrated. H atoms and the anthracene ring were omitted for clarity. B. Side view of the X-ray crystal structure of $[\text{Fe}_2(\text{PIMIC6})(\text{AnthCO}_2)] \cdot (\text{CH}_2\text{Cl}_2)$ in ORTEP representation at 50% probability. C and D. Isolated view of the diiron cores of the two independent molecules. Color scheme: iron, orange; carbon, white; nitrogen, blue; oxygen, red; fluorine, green; chlorine, bright green. Selected bond distances (\AA) and angles ($^\circ$): In C: $\text{Fe}(1) \cdots \text{Fe}(2) = 4.153(2)$; $\text{Fe}(1) \cdots \text{Cl}(6) = 3.168(3)$; $\text{Fe}(2) \cdots \text{Cl}(6) = 2.922(3)$; $\text{Fe}(1) - \text{O}(1) = 1.887(7)$; $\text{Fe}(1) - \text{O}(5) = 1.943(8)$; $\text{Fe}(1) - \text{O}(2) = 2.011(8)$; $\text{Fe}(1) - \text{N}(1) = 2.053(8)$; $\text{Fe}(2) - \text{O}(7) = 1.917(7)$; $\text{Fe}(2) - \text{O}(4) = 1.969(8)$; $\text{Fe}(2) - \text{O}(3) = 2.006(7)$; $\text{Fe}(2) - \text{N}(3) = 2.056(8)$; $\text{O}(5) - \text{Fe}(1) - \text{O}(2) = 113.8(3)$; $\text{O}(1) - \text{Fe}(1) - \text{N}(1) = 90.4(3)$; $\text{O}(4) - \text{Fe}(2) - \text{O}(3) = 114.0(3)$; $\text{O}(7) - \text{Fe}(2) - \text{N}(3) = 90.2(3)$. In D: $\text{Fe}(3) \cdots \text{Fe}(4) = 4.215(2)$; $\text{Fe}(3) \cdots \text{Cl}(4) = 3.230(3)$; $\text{Fe}(4) \cdots \text{Cl}(1\text{B}) = 2.885(3)$; $\text{Fe}(3) - \text{O}(10) = 1.900(7)$; $\text{Fe}(3) - \text{O}(12) = 1.924(8)$; $\text{Fe}(3) - \text{O}(13) = 2.012(7)$; $\text{Fe}(3) - \text{N}(4) = 2.046(8)$; $\text{Fe}(4) - \text{O}(8) = 1.906(7)$; $\text{Fe}(4) - \text{O}(11) = 1.978(8)$; $\text{Fe}(4) - \text{O}(14) = 2.000(7)$; $\text{Fe}(4) - \text{N}(5) = 2.068(8)$; $\text{O}(12) - \text{Fe}(3) - \text{O}(13) = 108.9(3)$; $\text{O}(10) - \text{Fe}(3) - \text{N}(4) = 91.1(3)$; $\text{O}(11) - \text{Fe}(4) - \text{O}(14) = 111.8(3)$; $\text{O}(8) - \text{Fe}(4) - \text{N}(5) = 89.5(3)$.

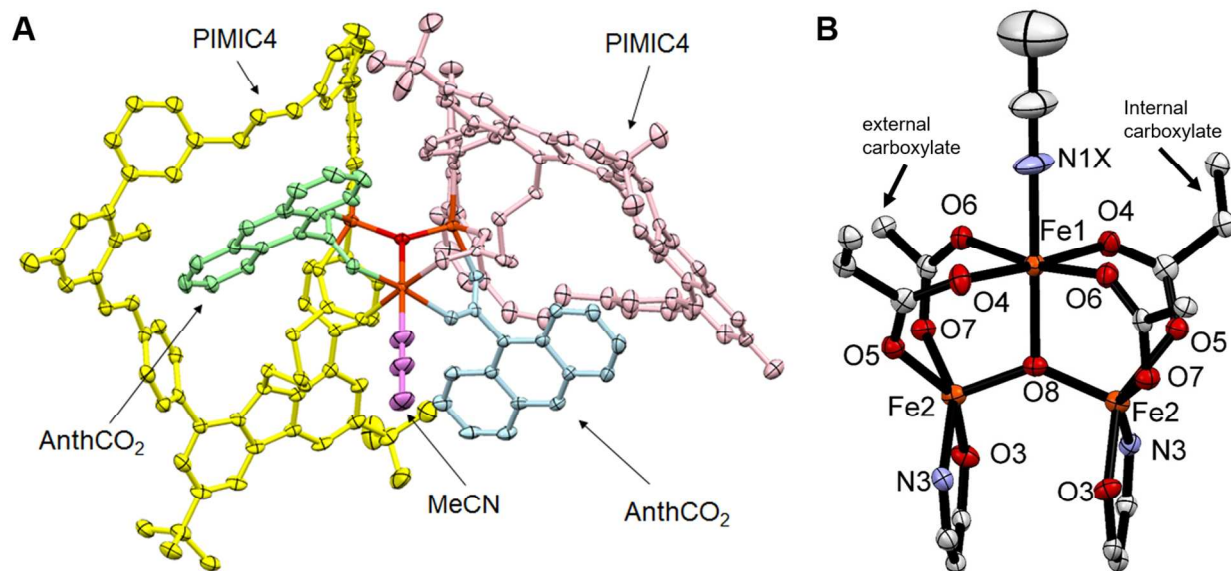


Figure S8. A. X-ray crystal structure of $[\text{Fe}_3(\mu_3\text{-O})(\text{HPIMIC4})_2(\text{AnthCO}_2)_2(\text{MeCN})]$ (**12**) in ORTEP representation at 50% probability. H atoms and non-coordinated solvent molecules were omitted for clarity. B. Isolated view of the triiron cores. Color scheme: iron, orange; carbon, white; nitrogen, blue; oxygen, red. The MeCN moiety coordinating to Fe(1) is disordered with several dichloromethane molecules. One of them shows weak binding interactions via Cl(1X). Selected bond distances (Å) and angles (°): Fe(1)···Fe(2) = 3.270(2); Fe(2)···Fe(2) = 3.380(1); Fe(1)–O(4) = 2.066(2); Fe(1)–O(6) = 2.151(2); Fe(1)–O(8) = 2.119(3); Fe(1)–N(1X) = 2.13(2); Fe(1)–Cl(1X) = 2.23(5); Fe(2)–O(3) = 1.907(2); Fe(2)–O(5) = 2.011(2); Fe(2)–O(7) = 2.023(2); Fe(2)–O(8) = 1.8216(13); Fe(2)–N(3) = 2.126(3); Fe(2)–Cl(6Y) = 2.372(17); O(4)–Fe(1)–O(4) = 176.00(15); O(4)–Fe(1)–O(8) = 92.00(8); O(4)–Fe(1)–O(6) = 88.98(9)/90.67(9); O(8)–Fe(1)–O(6) = 94.96(7); O(6)–Fe(1)–O(6) = 170.07(14); O(8)–Fe(1)–N(1X) = 180.0.

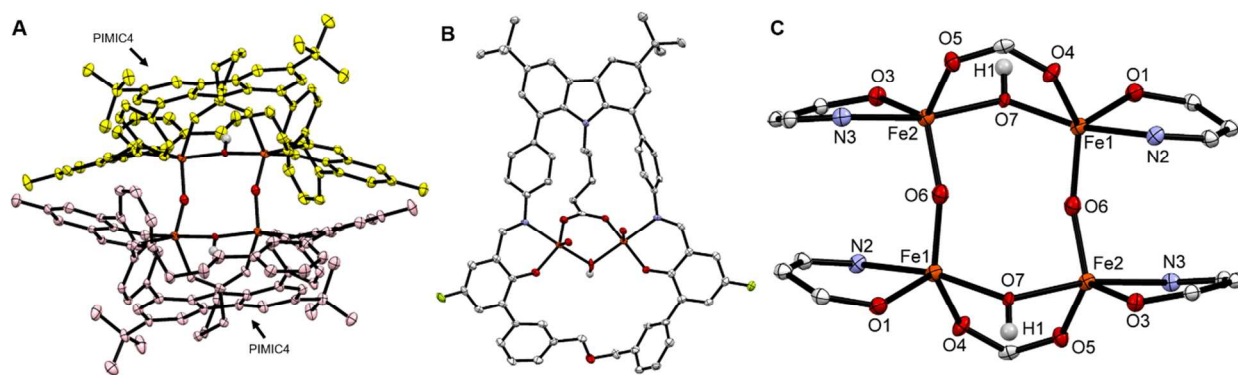


Figure S9. A. X-ray crystal structure of $[\text{Fe}_4(\mu\text{-O})_2(\mu\text{-OH})_2(\text{PIMIC4})_2]$ (**13**) in ORTEP representation at 50% probability. H atoms and non-coordinated solvent molecules were omitted for clarity. B. Isolated view of half of the tetrairon complex. C. Isolated view of the tetrairon cores. Color scheme: iron, orange; carbon, white; nitrogen, blue; oxygen, red; hydrogens of *OH*, light gray. Selected bond distances (\AA) and angles ($^\circ$): $\text{Fe}(1)\cdots\text{Fe}(2) = 3.426(0)/3.493(5)$; $\text{Fe}(1)\text{-O}(1) = 1.892(3)$; $\text{Fe}(1)\text{-O}(4) = 2.003(2)$; $\text{Fe}(1)\text{-O}(6) = 1.779(3)$; $\text{Fe}(1)\text{-O}(7) = 2.057(3)$; $\text{Fe}(1)\text{-N}(2) = 2.177(3)$; $\text{Fe}(2)\text{-O}(3) = 1.916(2)$; $\text{Fe}(2)\text{-O}(5) = 2.005(3)$; $\text{Fe}(2)\text{-O}(6) = 1.773(2)$; $\text{Fe}(2)\text{-O}(7) = 2.059(3)$; $\text{Fe}(2)\text{-N}(3) = 2.193(3)$; $\text{O}(6)\text{-Fe}(1)\text{-O}(7) = 100.52(11)$; $\text{O}(6)\text{-Fe}(1)\text{-N}(2) = 90.83(11)$; $\text{O}(1)\text{-Fe}(1)\text{-N}(2) = 84.71(11)$; $\text{O}(6)\text{-Fe}(2)\text{-O}(7) = 96.98(10)$; $\text{O}(6)\text{-Fe}(2)\text{-N}(3) = 93.82(11)$; $\text{O}(3)\text{-Fe}(2)\text{-N}(3) = 84.33(11)$.

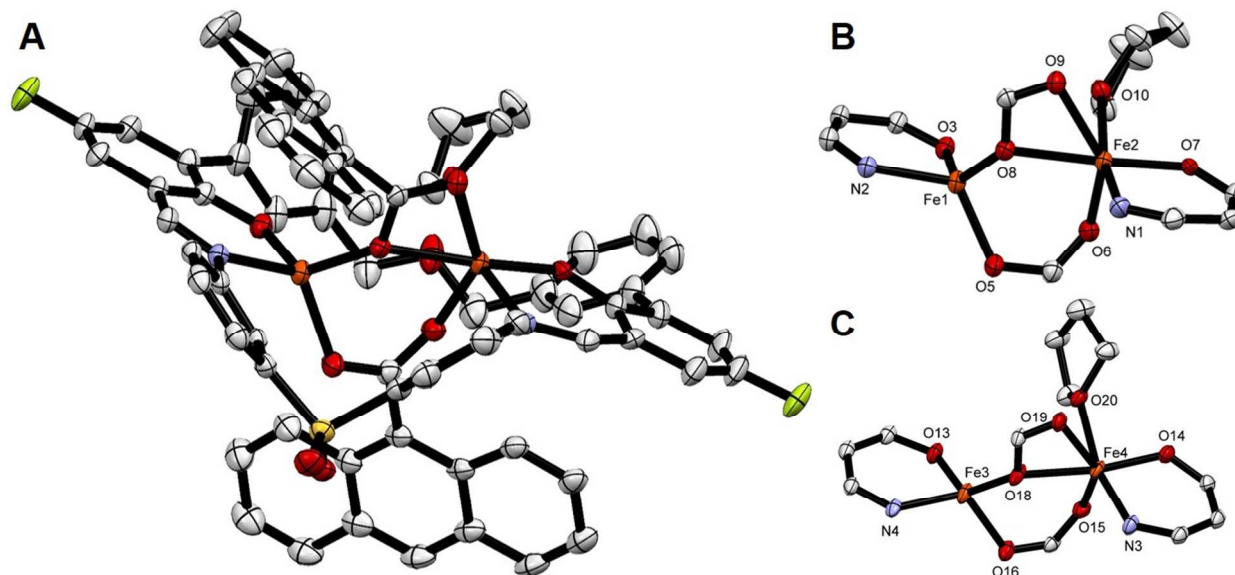


Figure S10. A. X-ray crystal structure of $[\text{Fe}_2(\text{F}_2\text{PIM})(\text{AnthCO}_2)(\text{THF})]$ (**14**) in ORTEP representation at 50% probability. There are two independent molecules of the complex in the asymmetric unit. Only one of them is illustrated. H atoms were omitted for clarity. B and C. Isolated view of the diiron cores of the two independent molecules of **14** in ORTEP representations at 50% probability. Color scheme: iron, orange; carbon, white; nitrogen, blue; oxygen, red; fluorine, green; sulfur, yellow. Selected bond distances (\AA) and angles ($^\circ$): $\text{Fe}(1)\cdots\text{Fe}(2) = 3.6155(7)$; $\text{Fe}(1)\text{--O}(3) = 1.902(6)$; $\text{Fe}(1)\text{--O}(5) = 2.0042(16)$; $\text{Fe}(1)\text{--O}(8) = 2.0264(17)$; $\text{Fe}(1)\text{--N}(2) = 2.0375(19)$; $\text{Fe}(2)\text{--O}(6) = 2.1282(18)$; $\text{Fe}(2)\text{--O}(7) = 1.911(11)$; $\text{Fe}(2)\text{--O}(8) = 2.1714(16)$; $\text{Fe}(2)\text{--O}(9) = 2.3260(17)$; $\text{Fe}(2)\text{--O}(10) = 2.1773(17)$; $\text{N}(1)\text{--Fe}(2) = 2.139(2)$; $\text{O}(5)\text{--Fe}(1)\text{--O}(8) = 96.12(7)$; $\text{O}(3)\text{--Fe}(1)\text{--N}(2) = 89.6(2)$; $\text{O}(6)\text{--Fe}(2)\text{--O}(8) = 86.07(6)$; $\text{O}(8)\text{--Fe}(2)\text{--O}(9) = 57.98(6)$; $\text{O}(7)\text{--Fe}(2)\text{--N}(1) = 85.5(4)$. In C: $\text{Fe}(3)\cdots\text{Fe}(4) = 3.643(1)$; $\text{Fe}(3)\text{--O}(13) = 1.858(6)$; $\text{Fe}(3)\text{--O}(16) = 1.9991(6)$; $\text{Fe}(3)\text{--O}(18) = 2.0256(16)$; $\text{Fe}(3)\text{--N}(4) = 2.078(6)$; $\text{Fe}(4)\text{--N}(3) = 2.156(2)$; $\text{Fe}(4)\text{--O}(14) = 1.9334(16)$; $\text{Fe}(4)\text{--O}(15) = 2.0971(16)$; $\text{Fe}(4)\text{--O}(18) = 2.1351(16)$; $\text{Fe}(4)\text{--O}(19) = 2.409(19)$; $\text{Fe}(4)\text{--O}(20) = 2.205(10)$; $\text{O}(16)\text{--Fe}(3)\text{--O}(18) = 94.84(7)$; $\text{O}(13)\text{--Fe}(3)\text{--N}(4) = 91.3(2)$; $\text{O}(15)\text{--Fe}(4)\text{--O}(18) = 87.42(6)$; $\text{O}(18)\text{--Fe}(4)\text{--O}(19) = 58.09(9)$; $\text{O}(14)\text{--Fe}(4)\text{--N}(3) = 87.39(7)$.

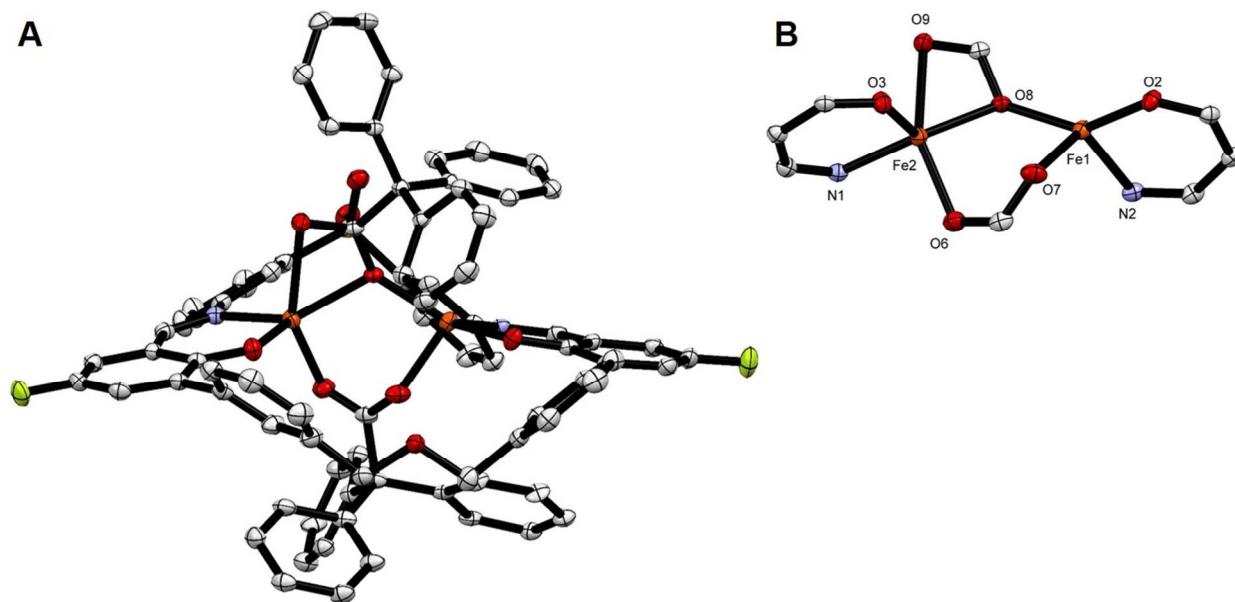


Figure S11. A. X-ray crystal structure of $[\text{Fe}_2(\text{F}_2\text{PIM})(\text{Ph}_3\text{CCO}_2)]$ (**15**) in ORTEP representation at 50% probability. H atoms and non-coordinated solvent molecules were omitted for clarity. B. Isolated view of the diiron core of $[\text{Fe}_2(\text{F}_2\text{PIM})(\text{Ph}_3\text{CCO}_2)]$ in ORTEP representation at 50% probability. Color scheme: iron, orange; carbon, white; nitrogen, blue; oxygen, red; fluorine, green. Selected bond distances (\AA) and angles ($^\circ$): In B: $\text{Fe}(1)\cdots\text{Fe}(2) = 4.064(1)$; $\text{Fe}(1)\text{--O}(2) = 1.8897(12)$; $\text{Fe}(1)\text{--O}(7) = 2.0087(13)$; $\text{Fe}(1)\text{--O}(8) = 2.0203(13)$; $\text{Fe}(1)\text{--N}(2) = 2.0593(14)$; $\text{N}(1)\text{--Fe}(2) = 2.0379(14)$; $\text{Fe}(2)\text{--O}(3) = 1.9058(12)$; $\text{Fe}(2)\text{--O}(6) = 2.0536(14)$; $\text{Fe}(2)\text{--O}(8) = 2.1320(12)$; $\text{Fe}(2)\text{--O}(9) = 2.3628(16)$; $\text{O}(7)\text{--Fe}(1)\text{--O}(8) = 88.03(5)$; $\text{O}(2)\text{--Fe}(1)\text{--N}(2) = 92.20(6)$; $\text{O}(3)\text{--Fe}(2)\text{--N}(1) = 92.96(6)$; $\text{O}(6)\text{--Fe}(2)\text{--O}(8) = 93.34(5)$; $\text{O}(8)\text{--Fe}(2)\text{--O}(9) = 57.79(4)$.

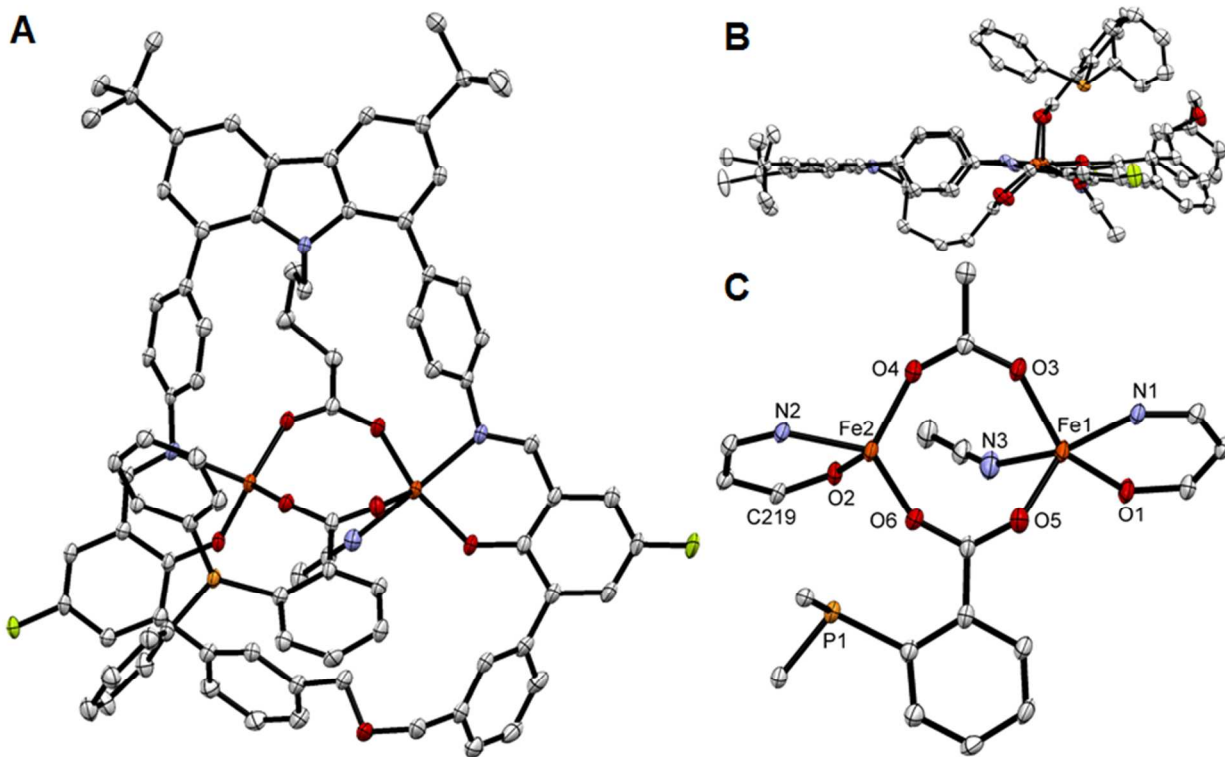


Figure S12. A. X-ray crystal structure of $[\text{Fe}_2(\text{PIMIC4})(o\text{-Ph}_2\text{PC}_6\text{H}_4\text{CO}_2)(\text{MeCN})]$ (**16**) in ORTEP representation at 50% probability. H atoms were omitted for clarity. B. Side view of the X-ray crystal structure of $[\text{Fe}_2(\text{PIMIC4})(o\text{-Ph}_2\text{PC}_6\text{H}_4\text{CO}_2)(\text{MeCN})]$ in ORTEP representation at 50% probability. C. Isolated view of the diiron cores. Color scheme: iron, orange; carbon, white; nitrogen, blue; oxygen, red; fluorine, green; phosphorus, light orange. Selected bond distances (Å) and angles (°): $\text{Fe}(1)\cdots\text{Fe}(2) = 4.064(1)$; $\text{Fe}(1)\text{--O}(1) = 1.951(2)$; $\text{Fe}(1)\text{--O}(3) = 2.025(2)$; $\text{Fe}(1)\text{--O}(5) = 2.021(2)$; $\text{Fe}(1)\text{--N}(1) = 2.130(3)$; $\text{Fe}(1)\text{--N}(3) = 2.231(3)$; $\text{Fe}(2)\text{--O}(2) = 1.909(2)$; $\text{Fe}(2)\text{--O}(4) = 1.967(2)$; $\text{Fe}(2)\text{--O}(6) = 1.969(2)$; $\text{Fe}(2)\text{--N}(2) = 2.058(2)$; $\text{Fe}(2)\text{--N}(3) = 3.109(3)$; $\text{O}(5)\text{--Fe}(1)\text{--O}(3) = 110.82(10)$; $\text{O}(1)\text{--Fe}(1)\text{--N}(1) = 87.14(10)$; $\text{O}(4)\text{--Fe}(2)\text{--O}(6) = 110.33(9)$; $\text{O}(2)\text{--Fe}(2)\text{--N}(2) = 89.06(10)$.

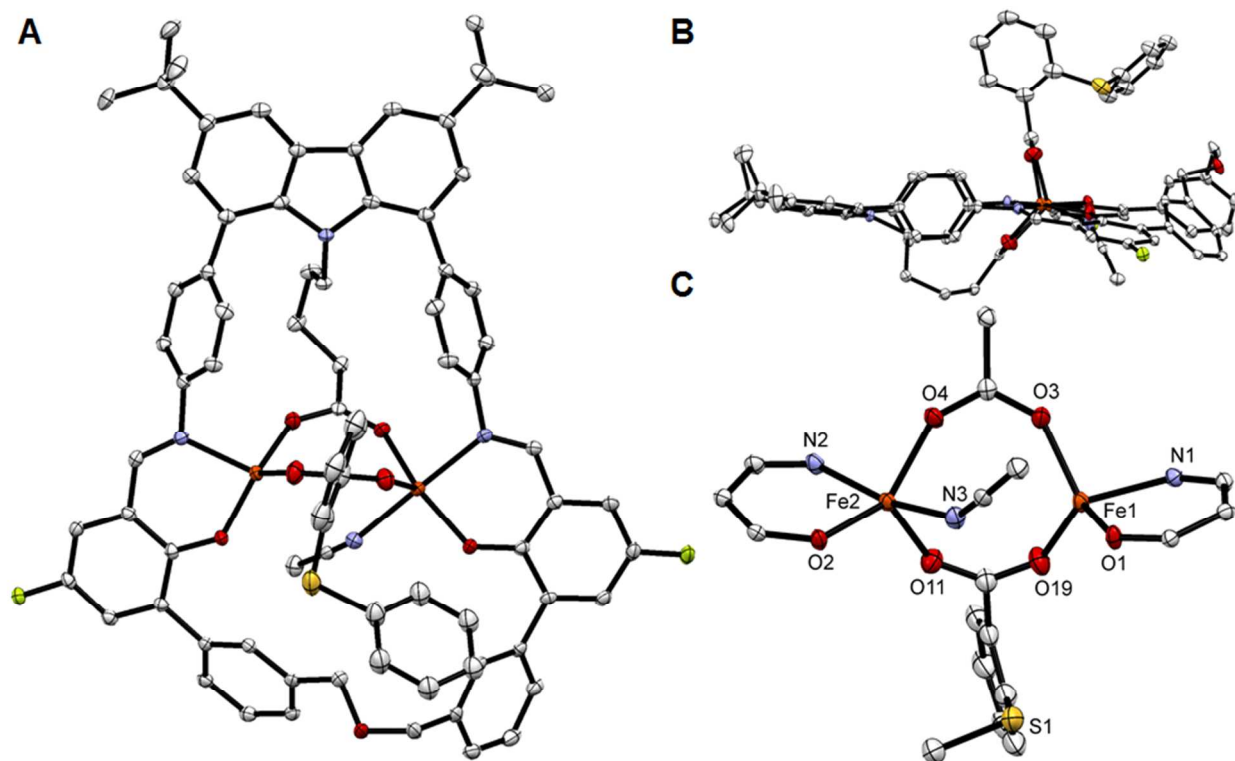


Figure S13. A. X-ray crystal structure of $[\text{Fe}_2(\text{PIMIC4})(o\text{-PhSC}_6\text{H}_4\text{CO}_2)(\text{MeCN})]$ (**17**) in ORTEP representation at 50% probability. H atoms were omitted for clarity. B. Side view of the X-ray crystal structure of $[\text{Fe}_2(\text{PIMIC4})(o\text{-PhSC}_6\text{H}_4\text{CO}_2)(\text{MeCN})]$ in ORTEP representation at 50% probability. C. Isolated view of the diiron cores. Color scheme: iron, orange; carbon, white; nitrogen, blue; oxygen, red; fluorine, green; sulfur, yellow. Selected bond distances (Å) and angles (°): $\text{Fe}(1)\cdots\text{Fe}(2) = 4.0490(5)$; $\text{Fe}(1)\text{--O}(1) = 1.9050(17)$; $\text{Fe}(1)\text{--O}(3) = 1.9764(18)$; $\text{Fe}(1)\text{--O}(19) = 1.9818(19)$; $\text{Fe}(1)\text{--N}(1) = 2.071(2)$; $\text{Fe}(2)\text{--O}(2) = 1.9551(17)$; $\text{Fe}(2)\text{--O}(4) = 2.0292(17)$; $\text{Fe}(2)\text{--O}(11) = 2.0584(19)$; $\text{Fe}(2)\text{--N}(2) = 2.131(2)$; $\text{Fe}(2)\text{--N}(3) = 2.198(2)$. The phenyl sulfide moiety is disordered, $\text{Fe}(1)\cdots\text{S}(1) = 4.826(4)$; $\text{Fe}(1)\cdots\text{S}(1\text{B}) = 4.911(7)$; $\text{Fe}(2)\cdots\text{S}(1) = 5.305(4)$; $\text{Fe}(2)\cdots\text{S}(1\text{B}) = 5.434(6)$; $\text{O}(3)\text{--Fe}(1)\text{--O}(19) = 106.65(8)$; $\text{O}(1)\text{--Fe}(1)\text{--N}(1) = 87.33(8)$; $\text{O}(4)\text{--Fe}(2)\text{--O}(11) = 103.20(8)$; $\text{O}(2)\text{--Fe}(2)\text{--N}(2) = 87.20(7)$.

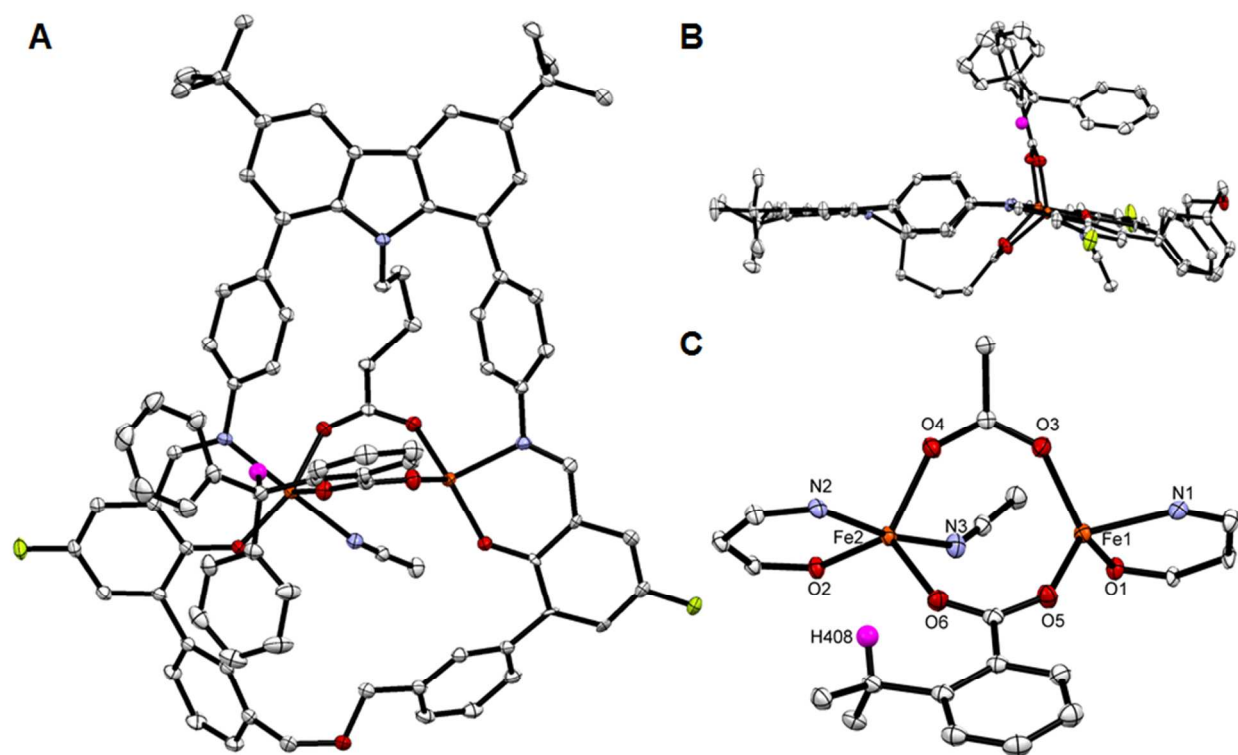


Figure S14. A. X-ray crystal structure of $[\text{Fe}_2(\text{PIMIC4})(o\text{-Ph}_2\text{CHC}_6\text{H}_4\text{CO}_2)(\text{MeCN})]$ (**18**) in ORTEP representation at 50% probability. H atoms and non-coordinated solvent molecules were omitted for clarity. B. Side view of the X-ray crystal structure of $[\text{Fe}_2(\text{PIMIC4})(o\text{-Ph}_2\text{CHC}_6\text{H}_4\text{CO}_2)(\text{MeCN})]$ in ORTEP representation at 50% probability. C. Isolated view of the diiron cores. Color scheme: iron, orange; carbon, white; nitrogen, blue; oxygen, red; fluorine, green; benzylic hydrogen, purple. Selected bond distances (\AA) and angles ($^\circ$): $\text{Fe}(1)\cdots\text{Fe}(2) = 3.9641(6)$; $\text{Fe}(1)\cdots\text{H}(408) = 3.422(5)$; $\text{Fe}(1)\text{--O}(1) = 1.9154(10)$; $\text{Fe}(1)\text{--O}(5) = 1.9871(10)$; $\text{Fe}(1)\text{--O}(3) = 1.9895(10)$; $\text{Fe}(1)\text{--N}(1) = 2.0691(12)$; $\text{Fe}(1)\text{--N}(3) = 3.027(1)$; $\text{Fe}(2)\text{--O}(2) = 1.9483(10)$; $\text{Fe}(2)\text{--O}(6) = 2.0304(10)$; $\text{Fe}(2)\text{--O}(4) = 2.0342(10)$; $\text{Fe}(2)\text{--N}(2) = 2.1577(12)$; $\text{Fe}(2)\text{--N}(3) = 2.2080(12)$; $\text{O}(3)\text{--Fe}(1)\text{--O}(5) = 107.44(5)$; $\text{O}(1)\text{--Fe}(1)\text{--N}(1) = 88.54(4)$; $\text{O}(4)\text{--Fe}(2)\text{--O}(6) = 105.54(4)$; $\text{O}(2)\text{--Fe}(2)\text{--N}(2) = 88.43(4)$.

4. Bond Valence Sum Analyses.

Our previous work²¹ showed that the oxidation state of iron atoms determined by bond valence sum analysis²² was in good agreement with the results obtained by other experimental methods.

Table S5. Bond Valence Sum Analyses for **7**, **12**, and **13**.

Complex	Bond	Bond Distance (Å)	Bond Valence ^a	Bond Valence Sum (BVS) ^b	Assigned Oxidation State
7	Fe(2)–O(2)	1.9163	0.61	2.17	2
	Fe(2)–O(4)	1.991	0.50		
	Fe(2)–O(6)	1.983	0.51		
	Fe(2)–N(4)	2.887	0.05		
	Fe(2)–N(3)	2.067	0.49		
	Fe(1)–O(1)	1.9335	0.59	2.20	2
	Fe(1)–O(3)	2.019	0.46		
	Fe(1)–O(5)	2.022	0.46		
	Fe(1)–N(4)	2.261	0.29		
	Fe(1)–N(1)	2.140	0.41		
12	Fe(1)–O(4)	2.066	0.41	2.23	2
	Fe(1)–O(4)	2.066	0.41		
	Fe(1)–O(6)	2.151	0.32		
	Fe(1)–O(6)	2.151	0.32		
	Fe(1)–O(8)	2.119	0.35		
	Fe(1)–N(1X)	2.13	0.20		
	Fe(2)–O(3)	1.907	0.67	2.99	3
	Fe(2)–O(5)	2.011	0.50		
	Fe(2)–O(7)	2.023	0.49		
	Fe(2)–O(8)	1.8216	0.85		
	Fe(2)–N(3)	2.126	0.48		
13	Fe(1)–O(1)	1.892	0.70	3.03	3
	Fe(1)–O(4)	2.003	0.52		
	Fe(1)–O(6)	1.779	0.95		
	Fe(1)–O(7)	2.057	0.45		
	Fe(1)–N(2)	2.176	0.42		
	Fe(2)–O(3)	1.916	0.65	2.98	3
	Fe(2)–O(5)	2.005	0.51		
	Fe(2)–O(6)	1.773	0.96		
	Fe(2)–O(7)	2.059	0.45		
	Fe(2)–N(3)	2.193	0.40		

^a The bond valence (s_{ij}), between cation i and anion j , was calculated based on the equation: $s_{ij} = \exp[(r_o - r)/B]$, in which r_o and B are empirically determined parameters and r is the observed bond distance. The following values were applied in these calculations. For Fe^{3+} : $r_o(\text{Fe}^{3+}-\text{O}) = 1.759 \text{ \AA}$, $r_o(\text{Fe}^{3+}-\text{N}) = 1.855 \text{ \AA}$; for Fe^{2+} : $r_o(\text{Fe}^{2+}-\text{O}) = 1.734 \text{ \AA}$, $r_o(\text{Fe}^{2+}-\text{N}) = 1.806 \text{ \AA}$; $B = 0.37$.²² ^b The bond valence sum (BVS) = $\sum s_{ij}$.

5. Cyclic voltammetry.

Cyclic voltammograms of 1.0 mM solutions of the diiron complexes **6-10** in dichloromethane were measured under inert atmosphere using a three-electrode setup containing a 2.0 mm diameter glassy carbon working electrode, a platinum auxiliary electrode, and a Ag/Ag⁺ pseudoreference electrode. *n*-Bu₄NPF₆ (0.1 M) was used as the supporting electrolyte. The measurements were carried out at scan rates of 50 to 1000 mV s⁻¹ at ambient temperature with a VersaSTAT3 potentiostat (Princeton Applied Research) operated with the V3 studio software. Data were referenced internally to the Fc⁺/Fc couple, which was added to the solutions of the complexes at the end of the measurements. Linear correlations were established between current (I) and square root of the scan rate V^{1/2}·s^{-1/2}, supporting the reversibility of the observed redox events.

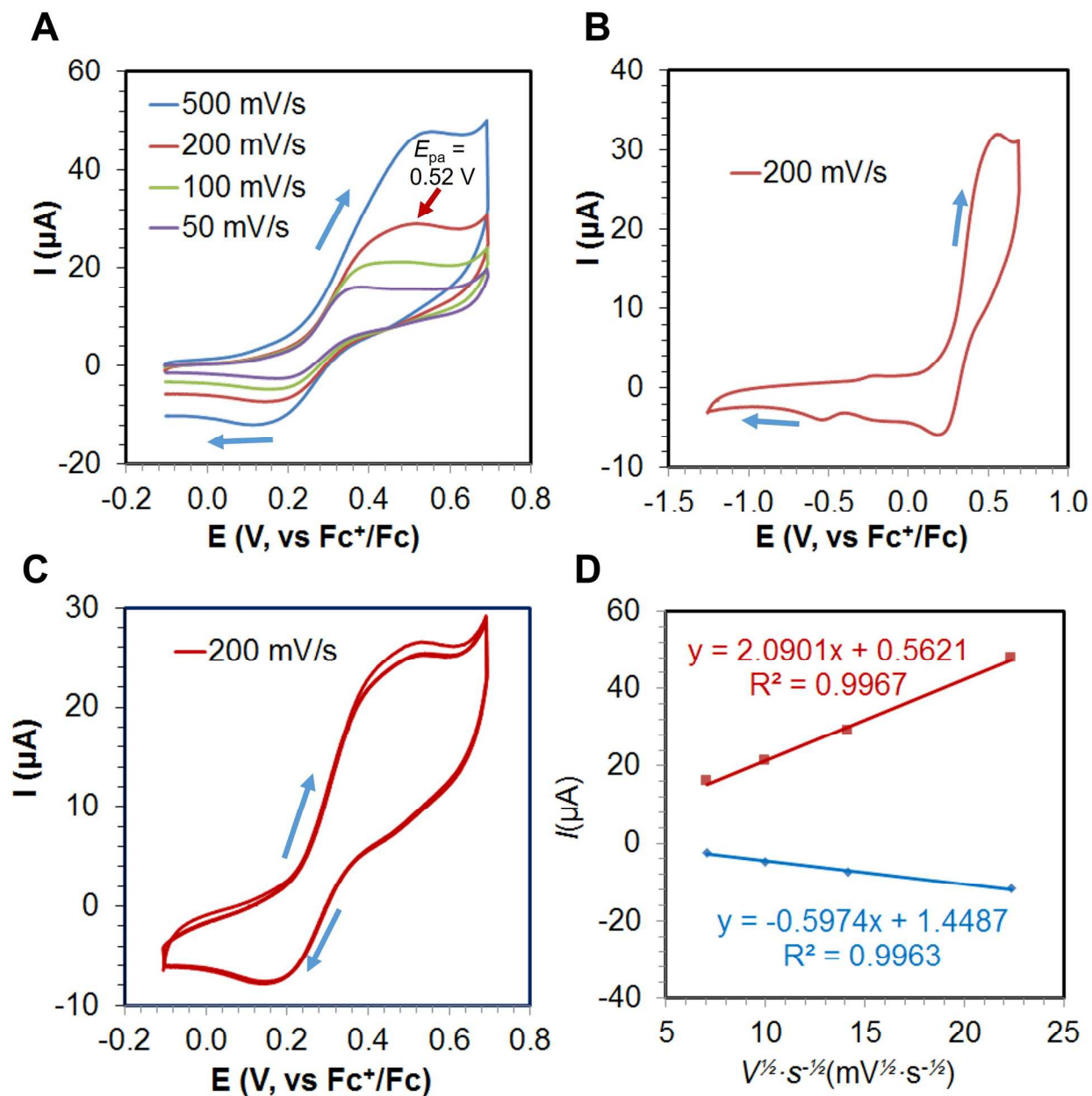


Figure S15. A-C. Cyclic voltammograms of 1.0 mM solutions of $[\text{Fe}_2(\text{PIMIC3})(\text{AnthCO}_2)(\text{MeCN})_2]$ (**6**) in dichloromethane at different scan rates and in different potential ranges. D. Correlation between current (I) and square root of scan rate $V^{1/2} \cdot s^{-1/2}$.

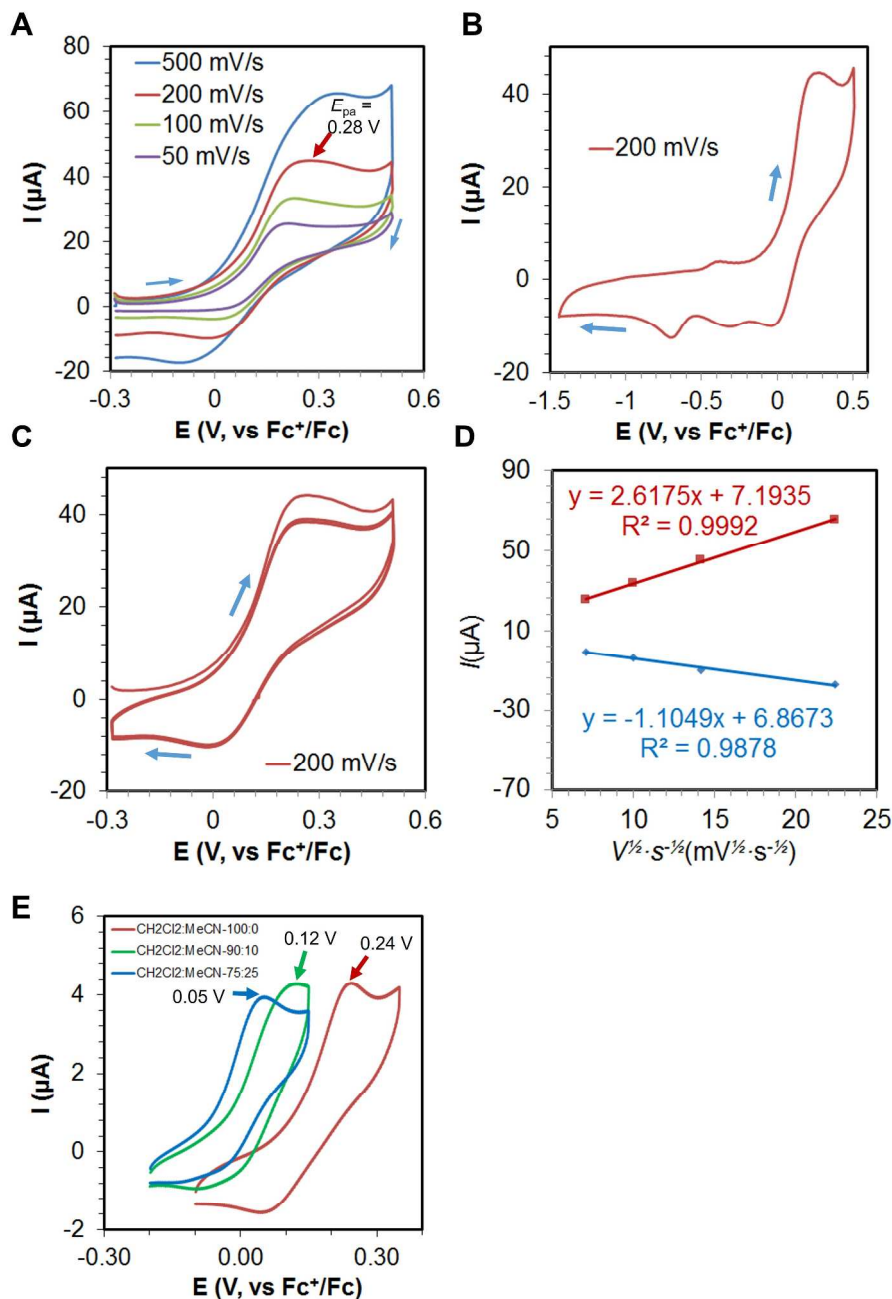


Figure S16. A-C. Cyclic voltammograms of 1.0 mM solutions of $[\text{Fe}_2(\text{PIMIC4})(\text{AnthCO}_2)(\text{MeCN})]$ (**7**) in dichloromethane at different scan rates and in different potential ranges. D. Correlation between current (I) and square root of scan rate $V^{1/2} \cdot s^{-1/2}$. E. Cyclic voltammograms of 1.0 mM solutions of $[\text{Fe}_2(\text{PIMIC4})(\text{AnthCO}_2)(\text{MeCN})]$ (**7**) in pure dichloromethane and dichloromethane-MeCN mixtures (v:v = 90:10 and 75:25). The potential was referenced to Fc^+/Fc at a scan rate of $100 \text{ mV} \cdot \text{s}^{-1}$. The results did not show a noticeable dependence of the reversibility of the redox events on the solvent polarity.

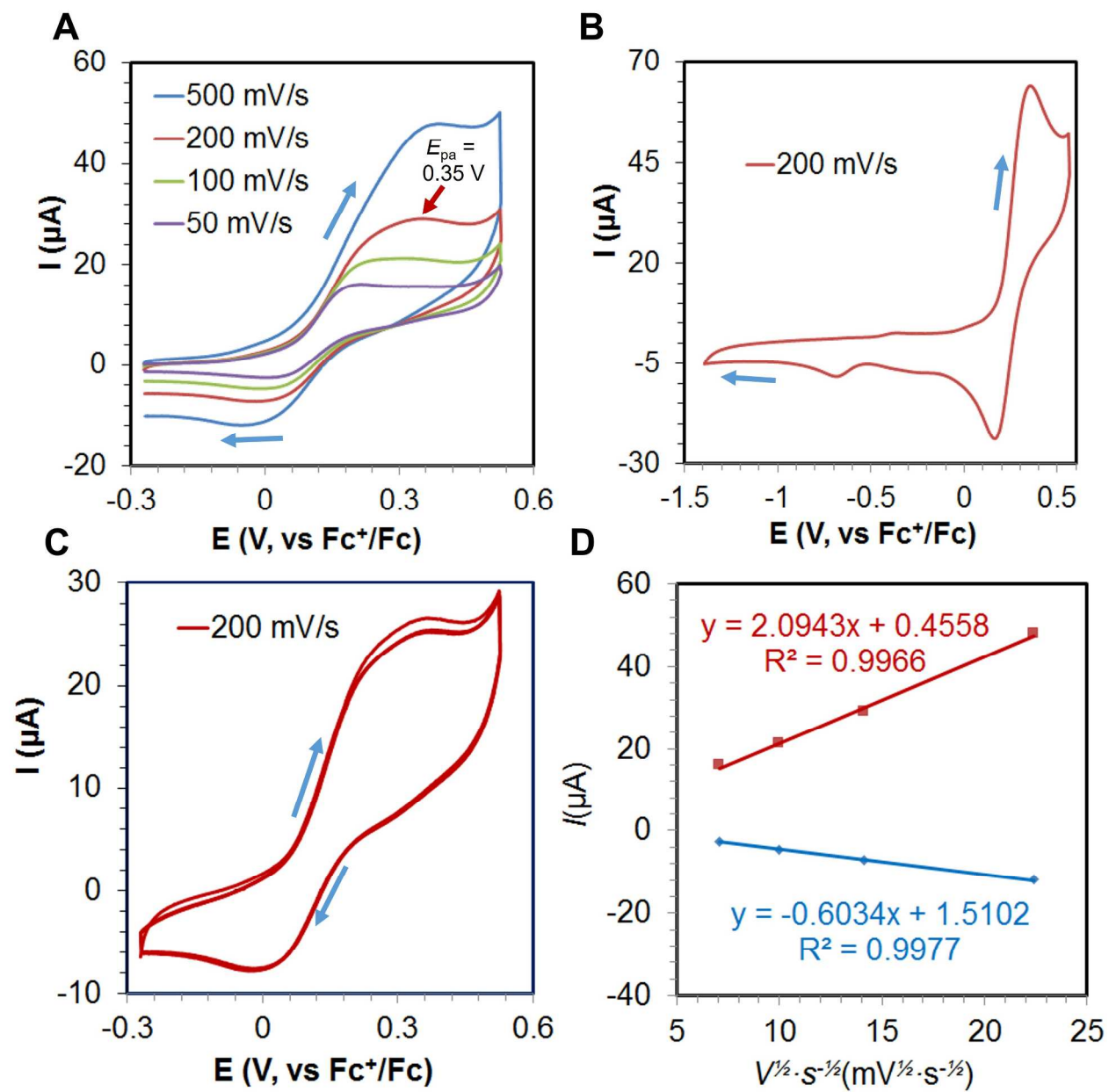


Figure S17. A-C. Cyclic voltammograms of 1.0 mM solutions of $[\text{Fe}_2(\text{PIMIC4})(\text{Ph}_3\text{CCO}_2)(\text{MeCN})]$ (8) in dichloromethane at different scan rates and in different potential ranges. D. Correlation between current (I) and square root of scan rate $V^{1/2} \cdot s^{-1/2}$.

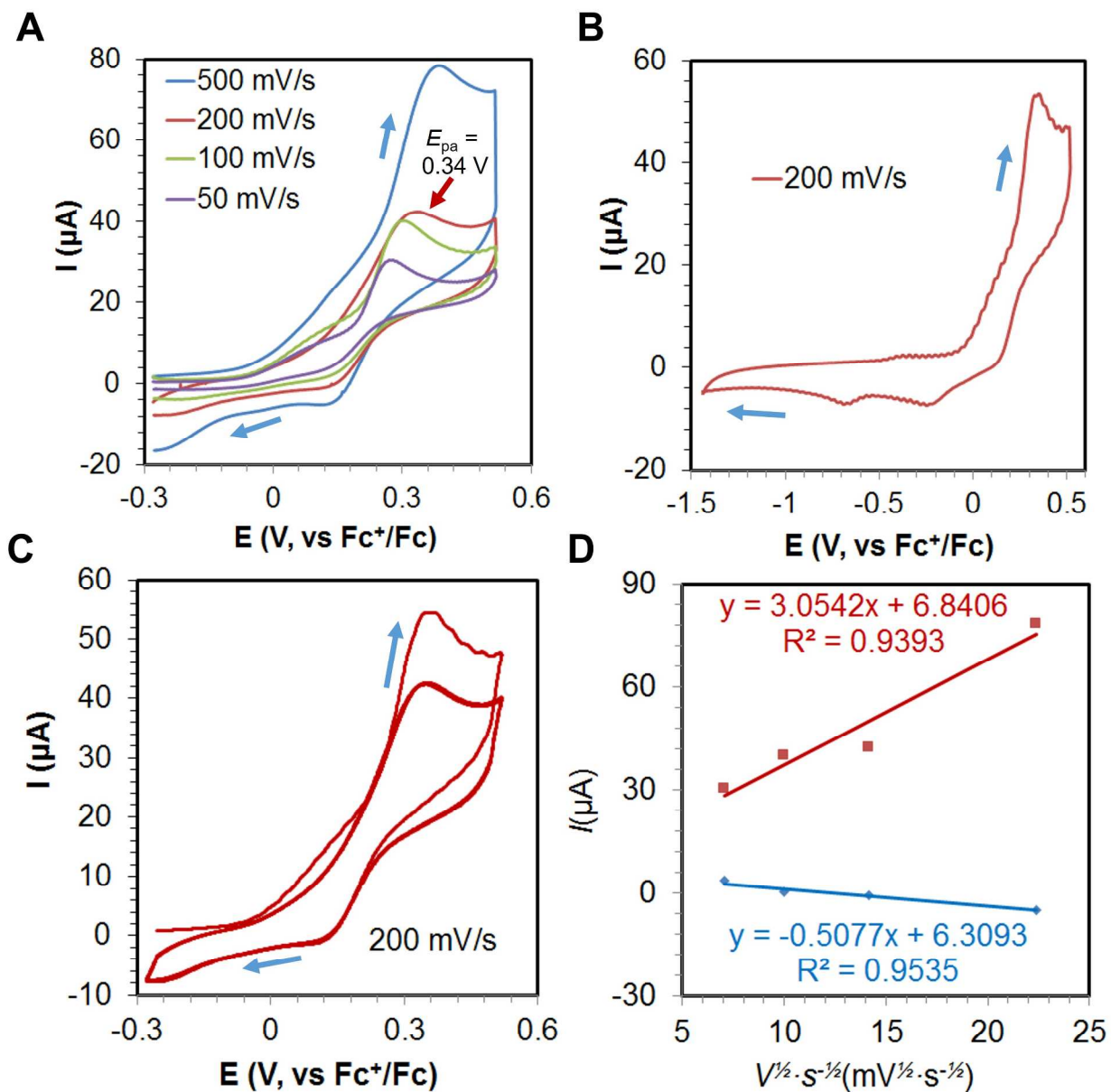


Figure S18. A-C. Cyclic voltammograms of 1.0 mM solutions of $[\text{Fe}_2(\text{PIMIC5})(\text{AnthCO}_2)(\text{MeCN})]$ (**9**) in dichloromethane at different scan rates and in different potential ranges. D. Correlation between current (I) and square root of scan rate $V^{1/2} \cdot s^{-1/2}$.

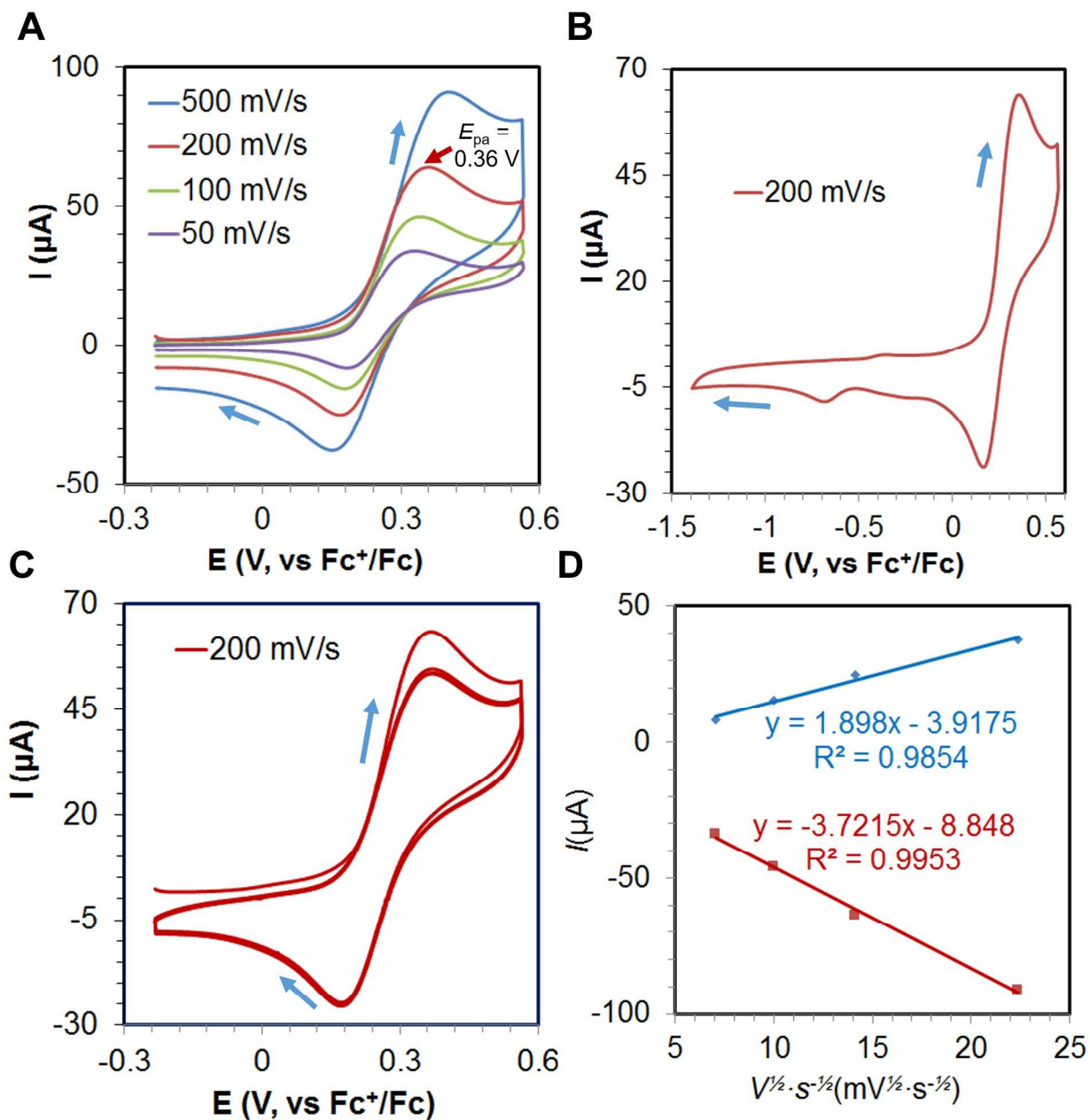


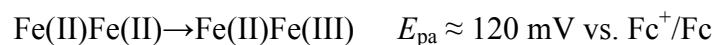
Figure S19. A-C. Cyclic voltammograms of 1.0 mM solutions of $[\text{Fe}_2(\text{PIMIC6})(\text{AnthCO}_2)(\text{MeCN})]$ (10) in dichloromethane at different scan rates and in different potential ranges. D. Correlation between current (I) and square root of scan rate $V^{1/2} \cdot s^{-1/2}$.

6. Chronocoulometry experiments.

Chronocoulometry experiments were conducted with $[\text{Fe}_2(\text{PIMIC4})(\text{AnthCO}_2)(\text{MeCN})]$ (**7**) at ambient temperature (21 ± 1 °C) in an N_2 glovebox using a Gamry REF 600 potentiostat and a three-electrode setup. Carbon paper was used as the working electrode, a Pt mesh in a separate, fritted compartment was used as the counter electrode, and Ag/AgNO_3 in a fritted compartment with acetonitrile was used as a pseudoreference electrode. Electrode potentials were referenced to the internal standard Fc^+/Fc couple. The experiments were carried out in a vigorously stirred solution of 0.1 M $n\text{-Bu}_4\text{NPF}_6$ in CH_2Cl_2 . The potential was held constant at 170 mV vs. Fc^+/Fc until there was no further increase in charge passed (Figures S20A and C). A cyclic voltammogram of **7** was acquired prior to each bulk electrolysis experiment to confirm the homogeneity of the sample (Figures S20B and D). A cyclic voltammogram of the $\text{H}_3\text{PIMIC4}$ ligand showed one redox event at +0.78 V vs. Fc^+/Fc . Therefore, the charge passed in the bulk electrolysis was unlikely to be due to the oxidation of the ligand (Figure S20E). In the first experiment, 6.6 μmol of **7** was electrolyzed for 22.3 h. The amount of charge passed was 0.923 C, corresponding to 1.5 electrons per diiron molecule. In the second experiment, 6.1 μmol of **7** was electrolyzed for 20.7 h. The amount of charge passed was 1.18 C, corresponding to 1.9 electrons per diiron molecule. In average, these measurements suggest that an overall two-electron oxidation of the diiron molecule at 170 mV vs. Fc^+/Fc .

Although the electrolysis indicates the observed redox event of **7** at 120 mV vs. Fc^+/Fc may be assigned as a two-electron process, other possibilities cannot be ruled out. The cyclic voltammograms of **7** from -0.2 V +0.8 V vs. Fc^+/Fc revealed a second oxidation wave at 440 mV at scan rates above 50 mV/s (Figures S20F and G). This wave disappeared at scan rates of 10 mV/s and 20 mV/s, an observation suggesting the product from the first oxidation event underwent decom-

position. Because the nature of the decomposition product(s) is not known, it is unclear if these species contributed to the amount of charge passed during the electrolysis process. If the decomposition product(s) were also oxidized during the bulk electrolysis, both oxidation waves can be assigned as one-electron processes according to the transformations below:



With the present data, we, nonetheless, refrain neither to explicitly assign the first wave as a two-electron process, nor to interpret the two waves as two sequential one-electron oxidation events.

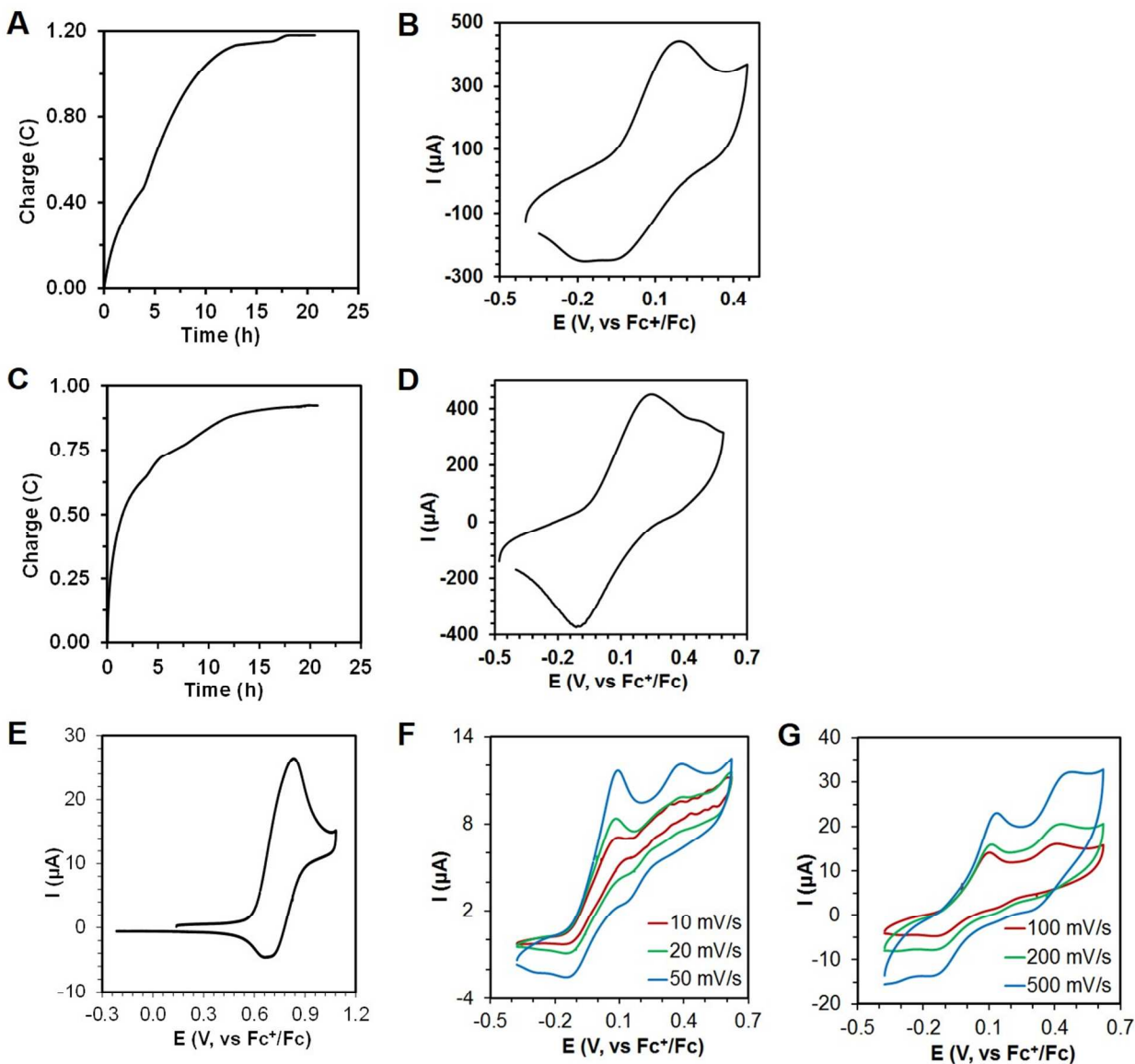


Figure S20. A.-D. Chronocoulometry and cyclic voltammometry experiments of $[\text{Fe}_2(\text{PIMIC4})(\text{AnthCO}_2)(\text{MeCN})]$ (**7**) in solution of 0.1 M $n\text{-Bu}_4\text{NPF}_6$ in CH_2Cl_2 . A. With 6.6 μmol of **7**. B. Pre-electrolysis cyclic voltammogram of **7** corresponding to the experiment in Panel A. The potential was referenced to Fc^+/Fc at a scan rate of $50 \text{ mV}\cdot\text{s}^{-1}$. C. With 6.1 μmol of **7**. D. Pre-electrolysis cyclic voltammogram of **7** corresponding to the experiment in Panel C. The potential was referenced to Fc^+/Fc at a scan rate of $100 \text{ mV}\cdot\text{s}^{-1}$. E. Cyclic voltammogram of the $\text{H}_3\text{PIMIC4}$ ligand acquired from -0.21 V to $+1.00 \text{ V}$ vs. Fc^+/Fc in solution of 0.1 M $n\text{-Bu}_4\text{NPF}_6$ in CH_2Cl_2 . F-G. Cyclic voltammogram of **7** acquired from -0.40 V to $+0.60 \text{ V}$ vs. Fc^+/Fc in solution of 0.1 M $n\text{-Bu}_4\text{NPF}_6$ in CH_2Cl_2 at different scan rates.

7. Oxidation Chemistry.

The oxidation of external substrates with diiron complexes was performed in an anaerobic dry box according to the following procedures.

7.1. Oxidation of External Substrates Using Urea-H₂O₂ in the Presence of Complexes 7, 8, 14, and 15 (Entries 1-3 of Table 1, Table 2, and Reaction d of Scheme 2).

To a dichloromethane solution of diiron complex (0.80 mL, 5.0 mM), a portion of substrate (0.20 mL, 20.0 mM, 1.0 equiv.) was added. The final concentration of the diiron complex and the substrate was 4.0 mM. Urea-H₂O₂ (1.9 mg, 0.020 mmol, 5.0 equiv.) was added in one portion at room temperature and the color of the mixture quickly turned dark brown. The mixture was kept in the anaerobic dry box with stirring for 30 min. *o*-Dichlorobenzene (0.40 mL, 20.0 mM, 2.0 equiv.) was added to the reaction mixture as an internal standard. To remove iron, the mixture was stirred with Chelex resin (~1 g). A small portion of the mixture was analyzed by GC-MS. For Entries 1 and 3 in Table 1, calibration curves were developed based on the relative response of the starting material to the product. For Entry 2 in Table 1 and all Entries in Table 2, calibration curves were developed based on the relative response of the starting material/product to the internal standard. With these calibration curves, the conversion of the substrate was determined according to the area ratio of the starting material/product and the internal standard.

7.2. Oxidation of External Substrates Using Urea-H₂O₂ in the Presence and Absence of [Fe(OTf)₂(MeCN)₂] (Table 1, control experiments).

To a mixture of dichloromethane (0.80 mL) and [Fe(OTf)₂(MeCN)₂] (3.5 mg, 0.008 mmol, 2.0 equiv.), a portion of substrate (0.20 mL, 20.0 mM, 1.0 equiv.) was added. The final concentration of the diiron complex and the substrate was 4.0 mM. Urea-H₂O₂ (1.9 mg, 0.020 mmol, 5.0 equiv.) was added in one portion at room temperature and the color of the mixture quickly turned dark

brown. The reaction mixture was stirred in the anaerobic dry box for 30 min. To remove iron, the mixture was stirred with Chelex resin (~1 g). A small portion of the mixture was analyzed by GC-MS. Calibration curves were developed based on the relative response of the starting material to the product. With these calibration curves, the conversion of the substrate was determined according to the area ratio of the starting material and the product.

7.3. Reaction between Complex 7 and MPPH.

To a dichloromethane solution of diiron complex (0.80 mL, 5.0 mM), a portion of MPPH (0.20 mL, 20.0 mM, 1.0 equiv.) was added at room temperature and the color of the mixture quickly turned dark brown. The reaction mixture was stirred in the anaerobic dry box for 30 min. *o*-Dichlorobenzene (0.40 mL, 20.0 mM, 2.0 equiv.) was added to the reaction mixture as an internal standard. To remove iron, the mixture was stirred with Chelex resin (~1 g). A small portion of the mixture was analyzed by GC-MS. Calibration curves were developed based on the relative response of the starting material/product to the internal standard. With these calibration curves, the conversion of the substrate was determined according to the area ratio of the starting material/product and the internal standard.

7.4. Oxidation of 2-Naphthalenemethanol with MPPH in the presence of Complex 7.

To a dichloromethane solution (0.90 mL) of diiron complex 7 (4.0 μmol) and 2-naphthalenemethanol (4.0 μmol), a portion of MPPH (0.10 mL, 20.0 mM, 0.5 equiv.) was added at room temperature and the color of the mixture quickly turned dark brown. The reaction mixture was stirred in the anaerobic dry box for 30 min. *o*-Dichlorobenzene (0.40 mL, 20.0 mM, 2.0 equiv.) was added to the reaction mixture as an internal standard. To remove iron, the mixture was stirred with Chelex resin (~1 g). A small portion of the mixture was analyzed by GC-MS. Calibration curves were developed based on the relative response of the starting material/product

to the internal standard. With these calibration curves, the conversion of the substrate was determined according to the area ratio of the starting material/product and the internal standard.

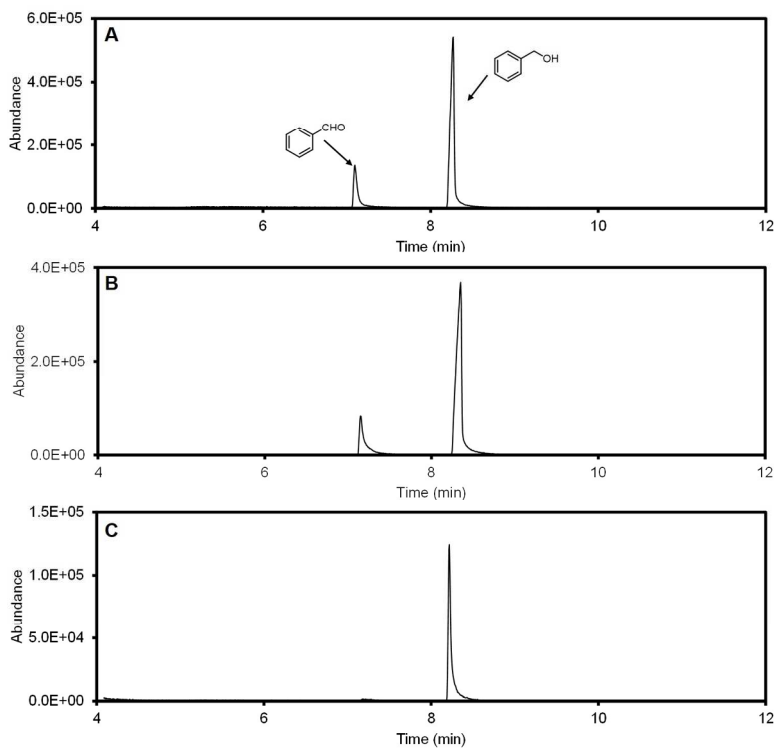


Figure S21. A. GC chromatogram of the reaction mixture of benzyl alcohol with complex **7** and urea-H₂O₂ (21% conversion); B. GC chromatogram of the reaction mixture of benzyl alcohol with [Fe(OTf)₂(MeCN)₂] and urea-H₂O₂ (12% conversion); C. GC chromatogram of the reaction mixture of benzyl alcohol with urea-H₂O₂.

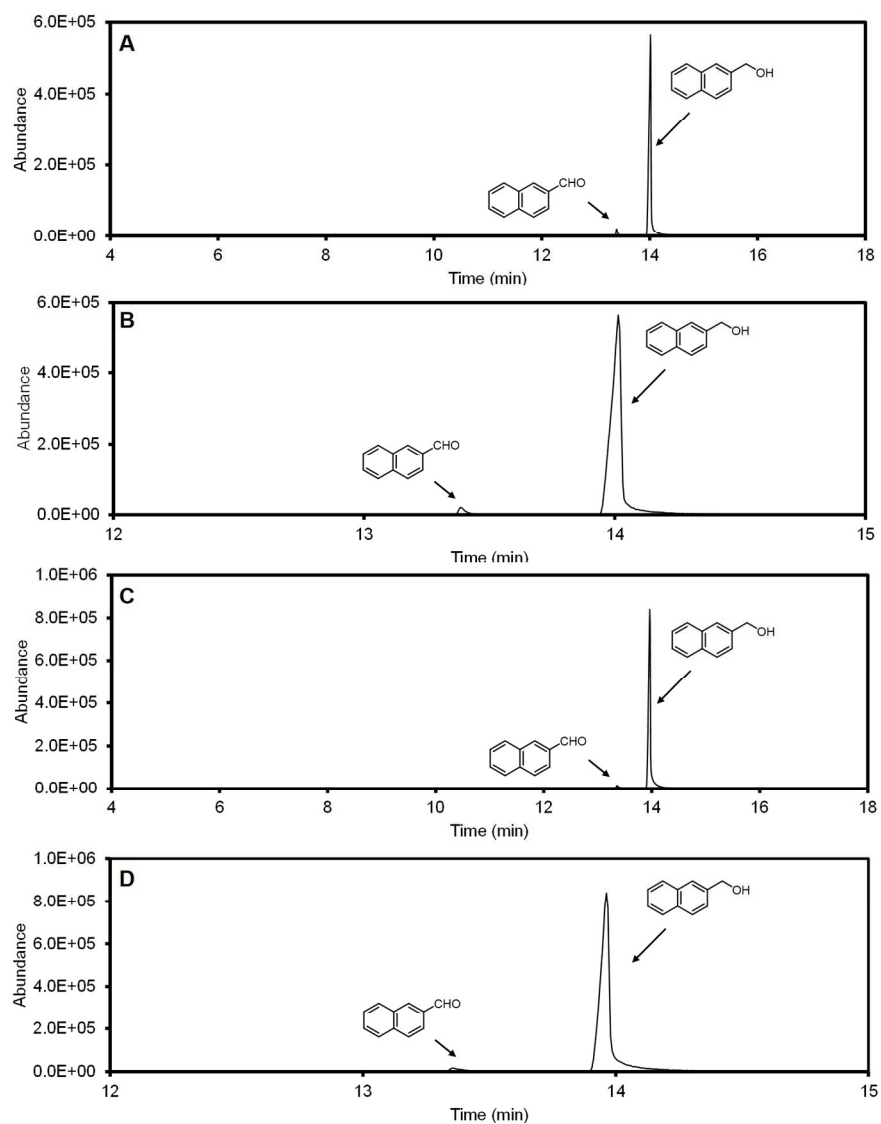


Figure S22. A. GC chromatogram of the reaction mixture of 2-naphthalenemethanol with [Fe(OTf)₂(MeCN)₂] and urea-H₂O₂ (2% conversion); B. Expansion of panel A; C. GC chromatogram of the oxidation reaction mixture of 2-naphthalenemethanol with urea-H₂O₂; D. Expansion of panel C.

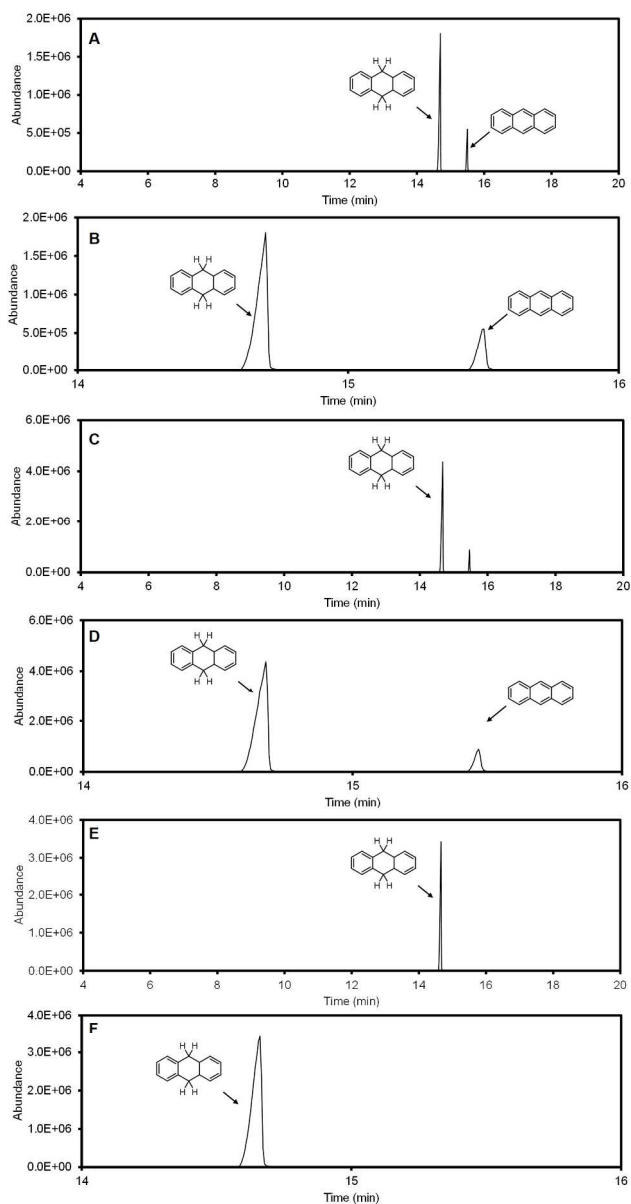


Figure S23. A. GC chromatogram of the reaction mixture of 9,10-dihydroanthracene (DHA) with complex **7** and urea- H_2O_2 (18% conversion); B. Expansion of panel A; C. GC chromatogram of the oxidation reaction mixture of DHA with $[\text{Fe}(\text{OTf})_2(\text{MeCN})_2]$ and urea- H_2O_2 (14% conversion); D. Expansion of panel C; E. GC chromatogram of the oxidation reaction mixture of DHA with urea- H_2O_2 ; F. Expansion of panel E.

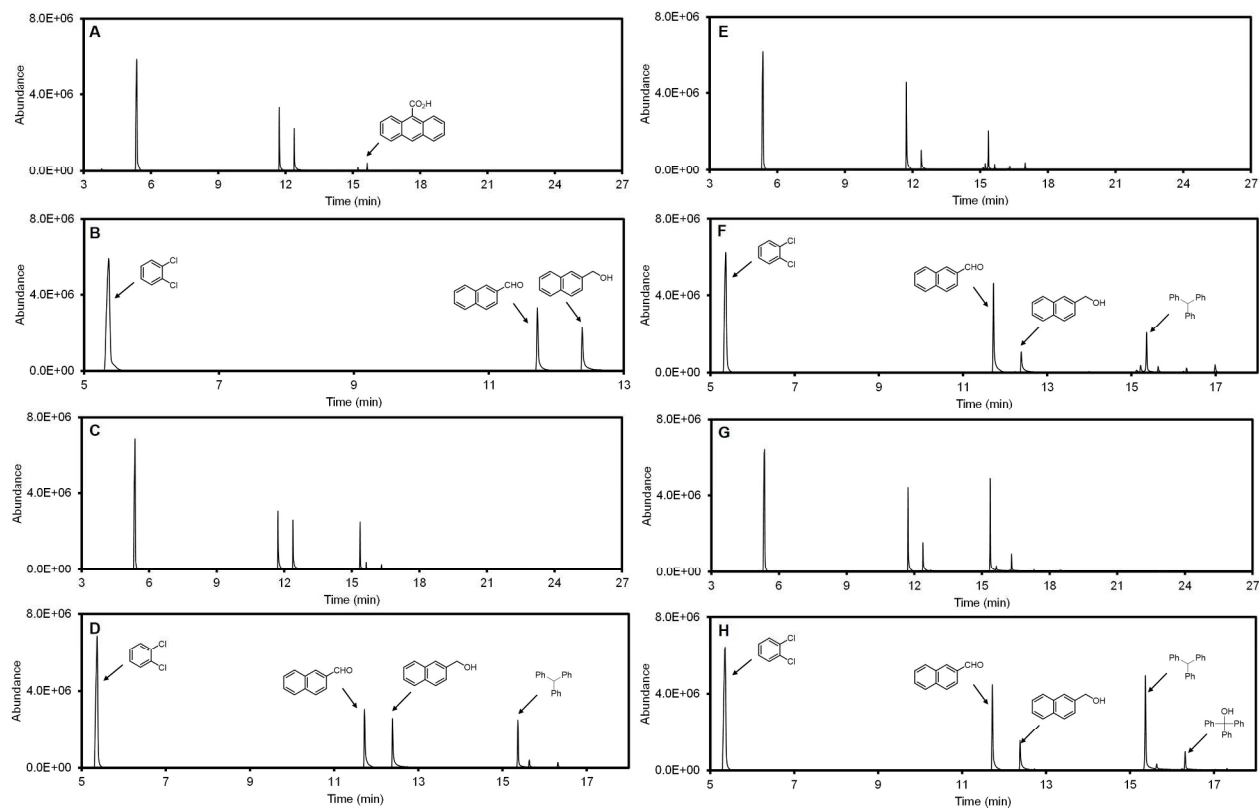


Figure S24. A. GC chromatogram of the reaction mixture of 2-naphthalenemethanol with complex **7** (49% conversion); B. Expansion of panel A; C. GC chromatogram of the reaction mixture of 2-naphthalenemethanol with complex **8** (47% conversion); D. Expansion of panel C; E. GC chromatogram of the reaction mixture of 2-naphthalenemethanol with complex **14** (69% conversion); F. Expansion of panel E; G. GC chromatogram of the reaction mixture of 2-naphthalenemethanol with complex **15** (59% conversion); H. Expansion of panel G.

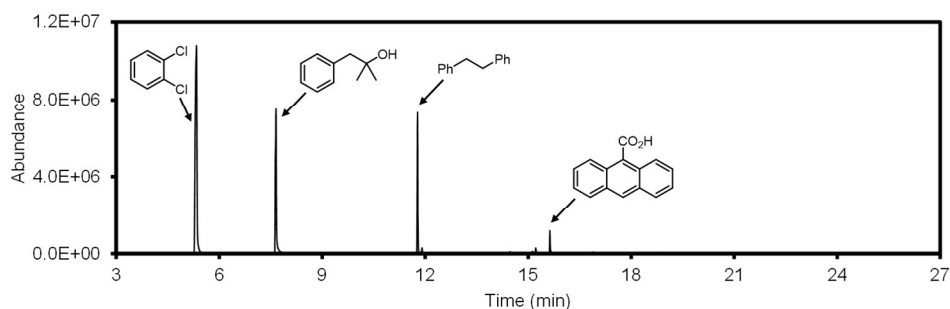


Figure S25. GC chromatogram of the reaction mixture of complex **7** and MPPH (Conversions of $\text{PhCH}_2(\text{Me})_2\text{COH}$ and $\text{PhC}_2\text{H}_4\text{Ph}$ are 77% and 23%, respectively).

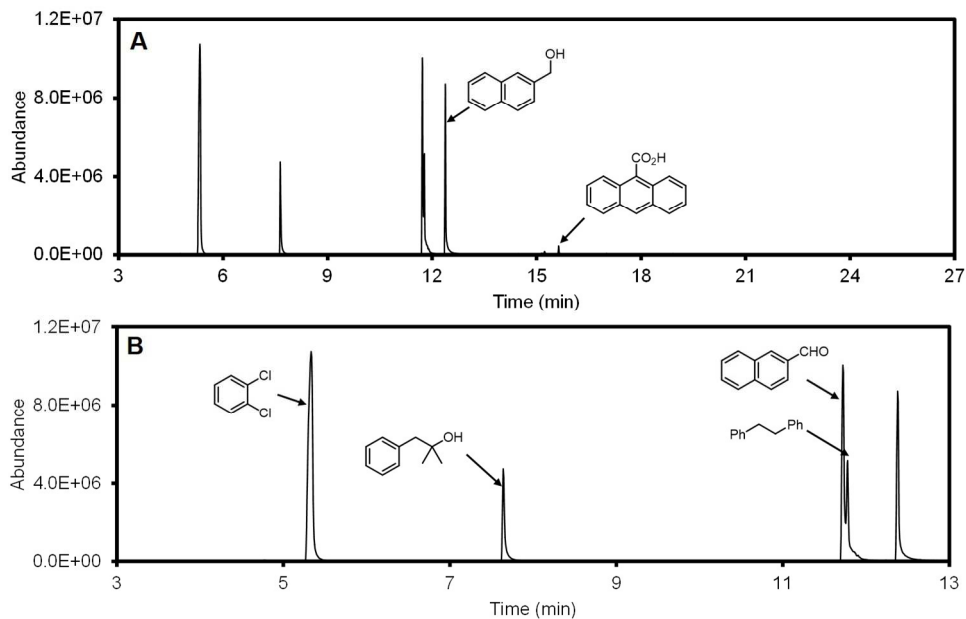


Figure S26. A. GC chromatogram of the reaction mixture of 2-naphthalenemethanol, complex **7**, and MPPH; B. Expansion of panel A. (Conversion of 2-naphthalenemethanol to 2-naphthaldehyde is 45%. Conversions of MPPH to PhCH₂(Me)₂COH and PhC₂H₄Ph are 59% and 41%, respectively).

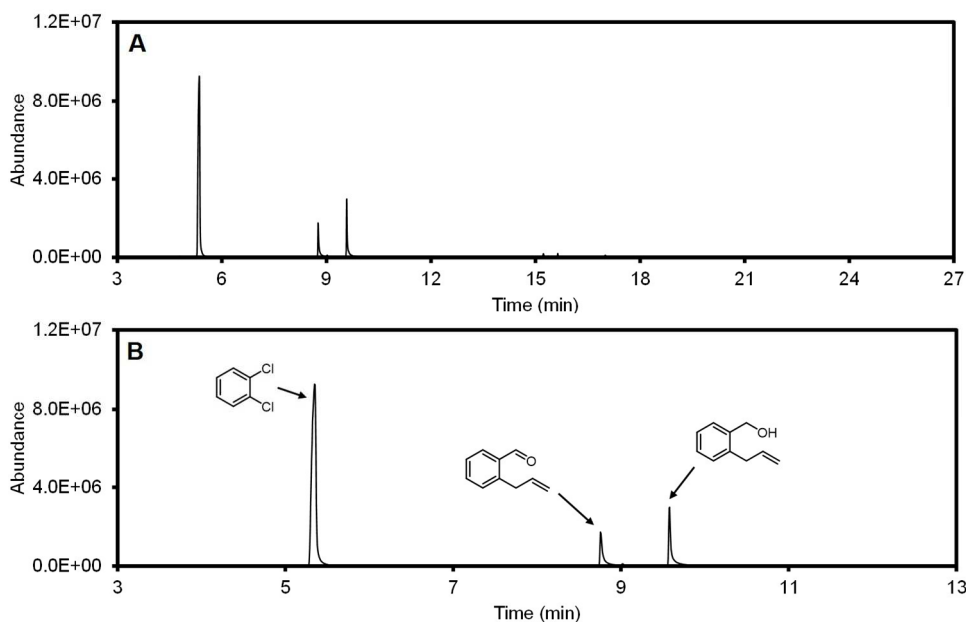


Figure S27. A. GC chromatogram of the reaction mixture of (2-allylphenyl)methanol, complex **7**, and urea-H₂O₂; B. Expansion of panel A.

8. NMR Spectra.

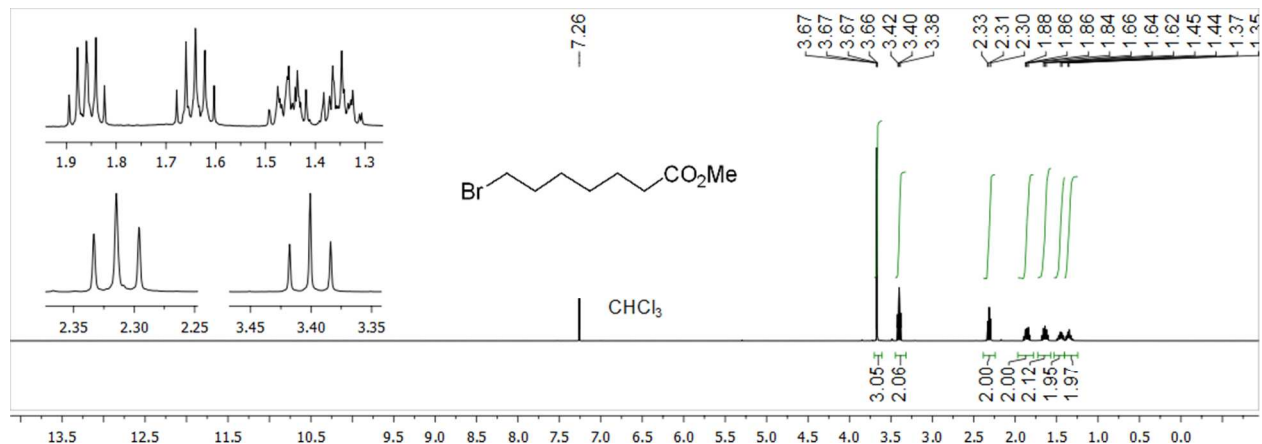


Figure S28. ^1H NMR spectrum of methyl 7-bromoheptanoate.

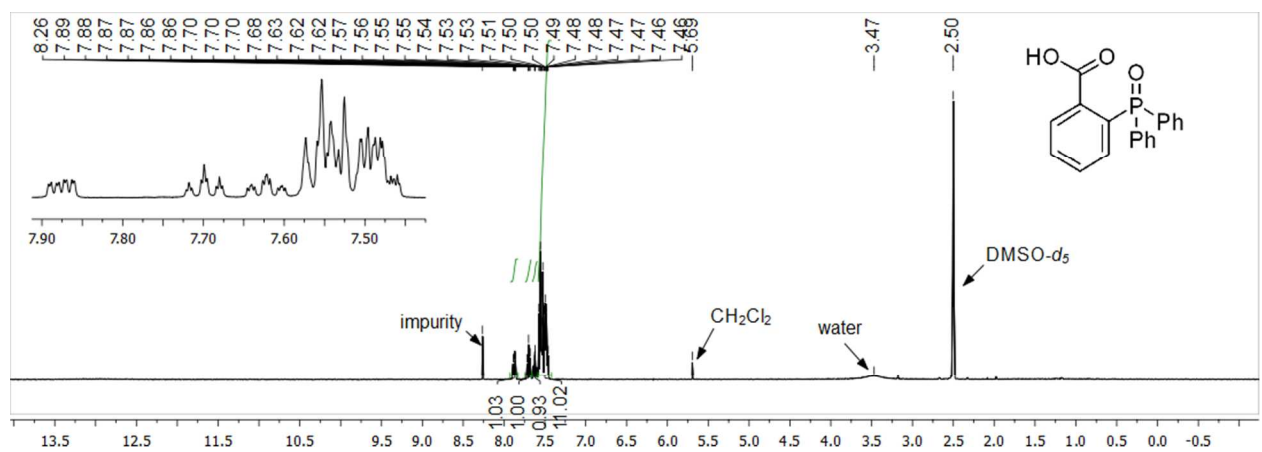


Figure S29. ^1H NMR spectrum of 2-(diphenylphosphoryl)benzoic acid.

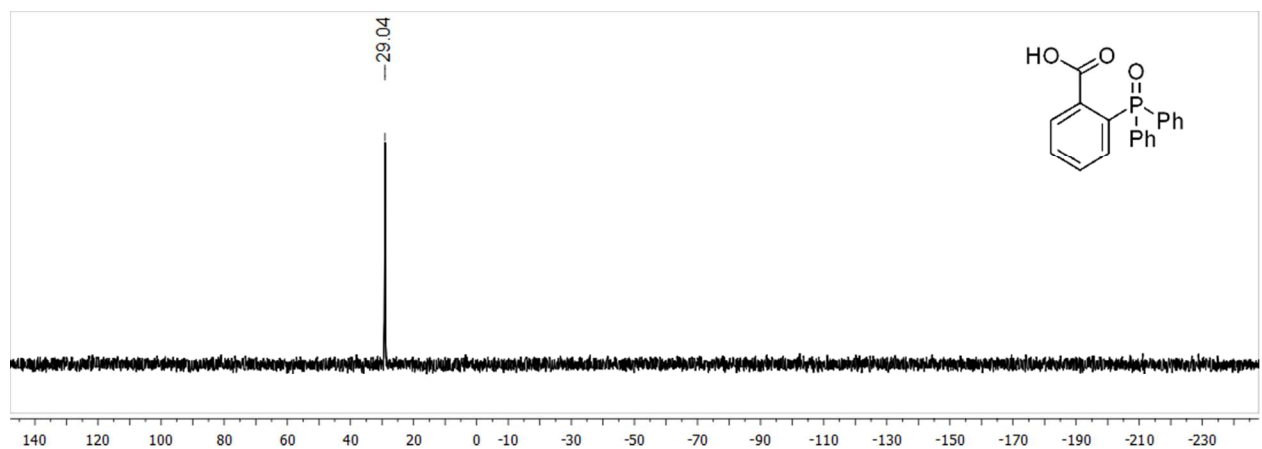


Figure S30. ^{31}P NMR spectrum of 2-(diphenylphosphoryl)benzoic acid.

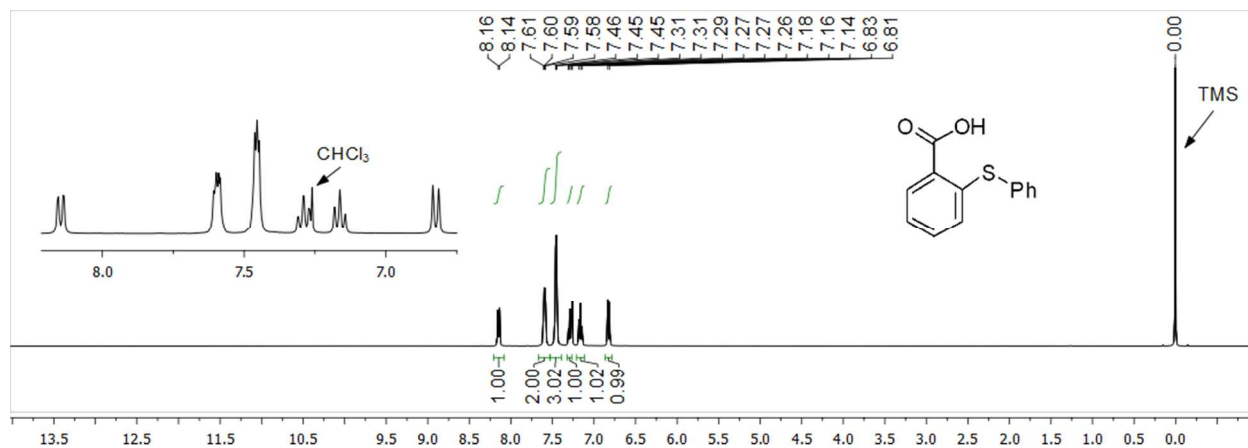


Figure S31. ^1H NMR spectrum of 2-(phenylthio)benzoic acid.

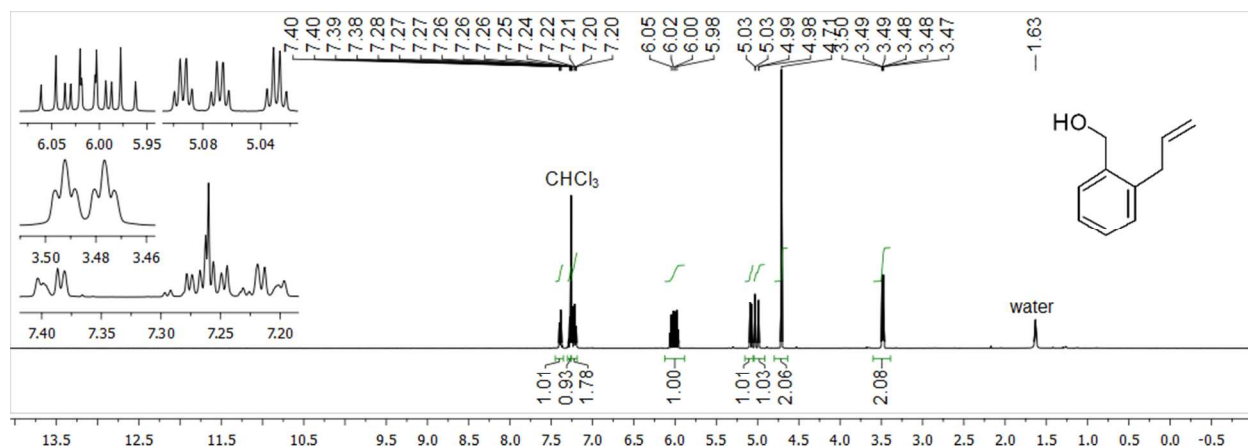


Figure S32. ^1H NMR spectrum of (2-allylphenyl)methanol.

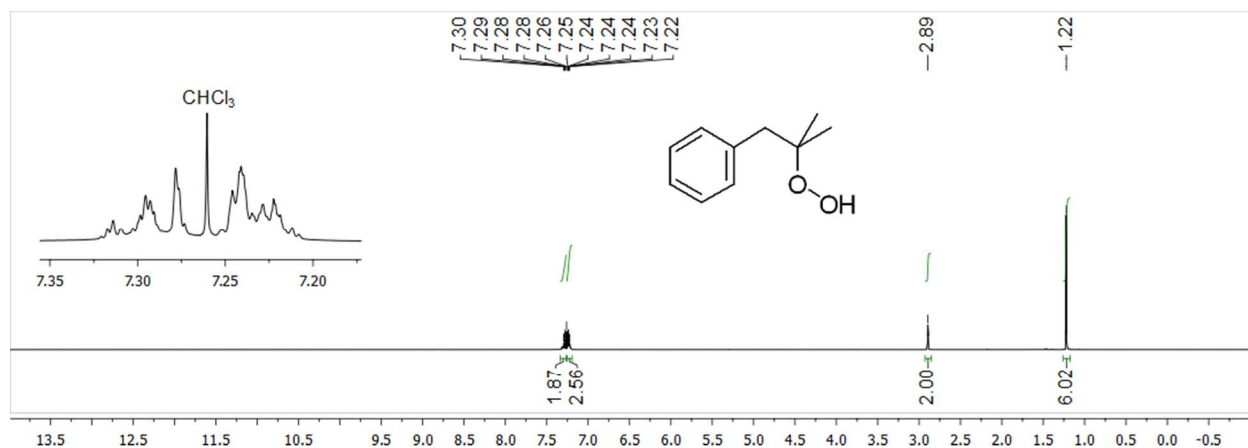


Figure S33. ^1H NMR spectrum of 2-methyl-1-phenylprop-2-yl hydroperoxide (MPPH).

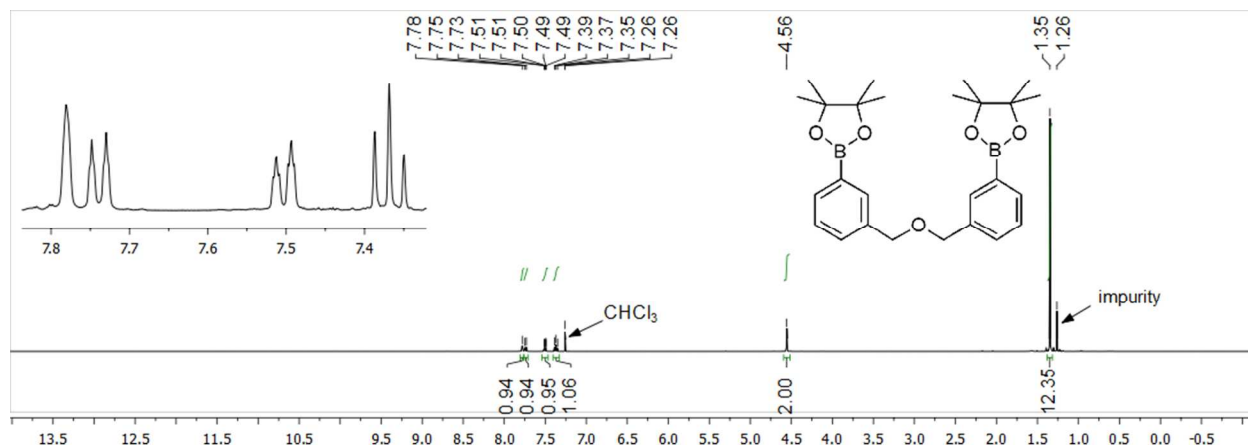


Figure S34. ¹H NMR spectrum of ((oxybis(methylene))bis(3,1-phenylene))diboronic acid pinacol ester.

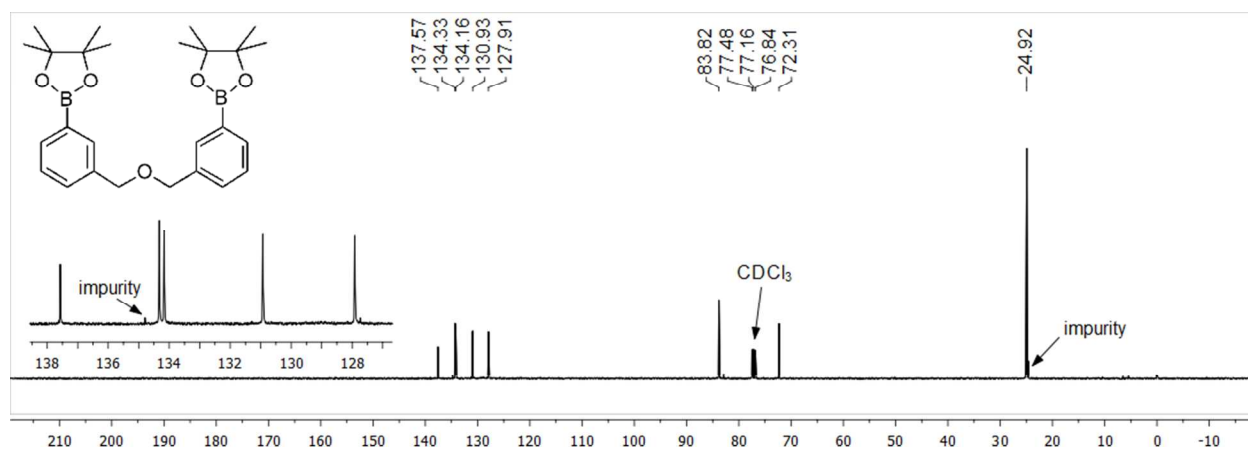


Figure S35. ¹³C{¹H} NMR spectrum of ((oxybis(methylene))bis(3,1-phenylene))diboronic acid pinacol ester.

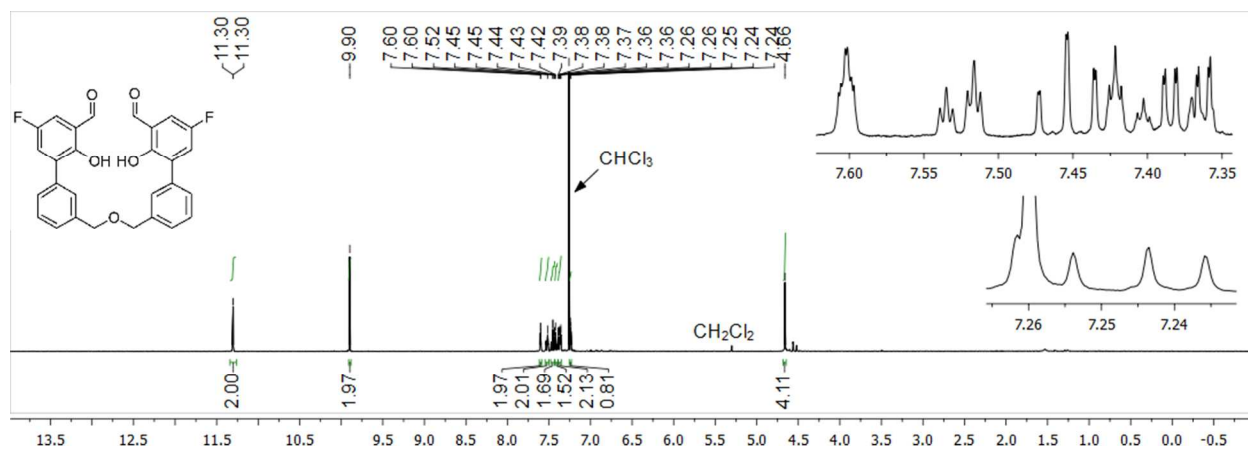


Figure S36. ¹H NMR spectrum of 3',3'''-(oxybis(methylene))bis(5-fluoro-2-hydroxy-[1,1'-biphenyl]-3-carbaldehyde).

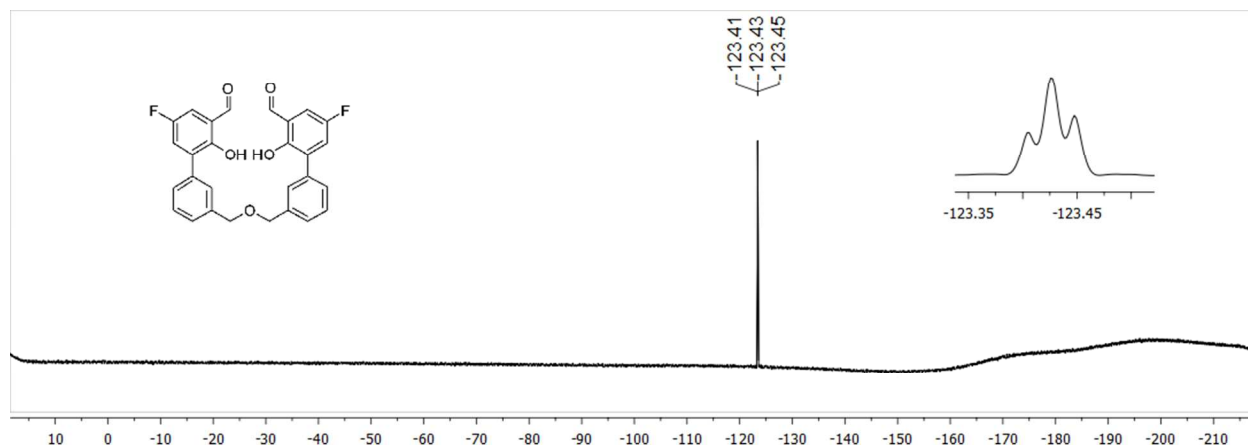


Figure S37. ^{19}F NMR spectrum of 3,3'-(oxybis(methylene))bis(5-fluoro-2-hydroxy-[1,1'-biphenyl]-3-carbaldehyde).

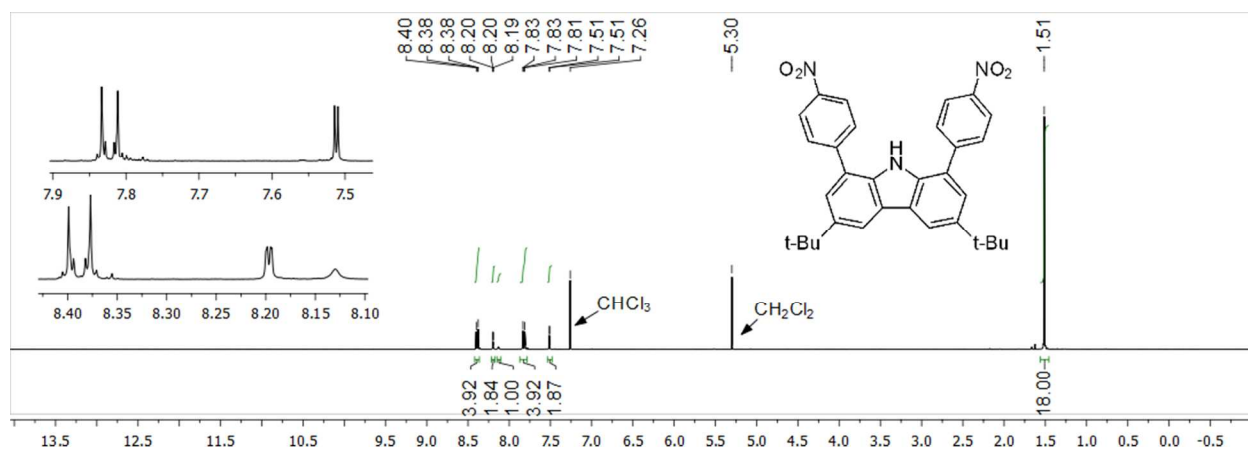


Figure S38. ^1H NMR spectrum of 3,6-di-*tert*-butyl-1,8-bis(4-nitrophenyl)-9H-carbazole (**2**).

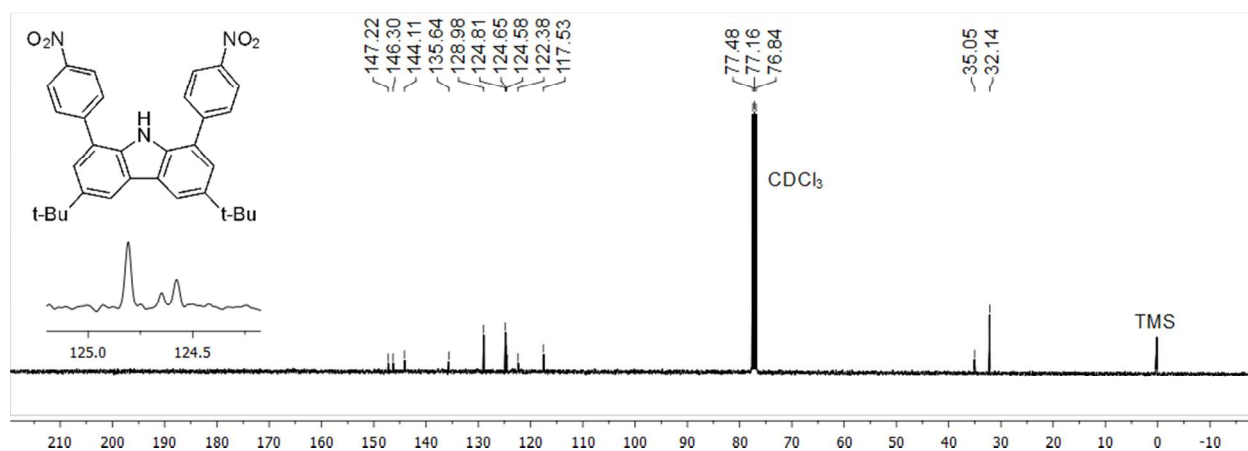


Figure S39. $^{13}\text{C}\{^1\text{H}\}$ NMR spectrum of 3,6-di-*tert*-butyl-1,8-bis(4-nitrophenyl)-9H-carbazole (**2**).

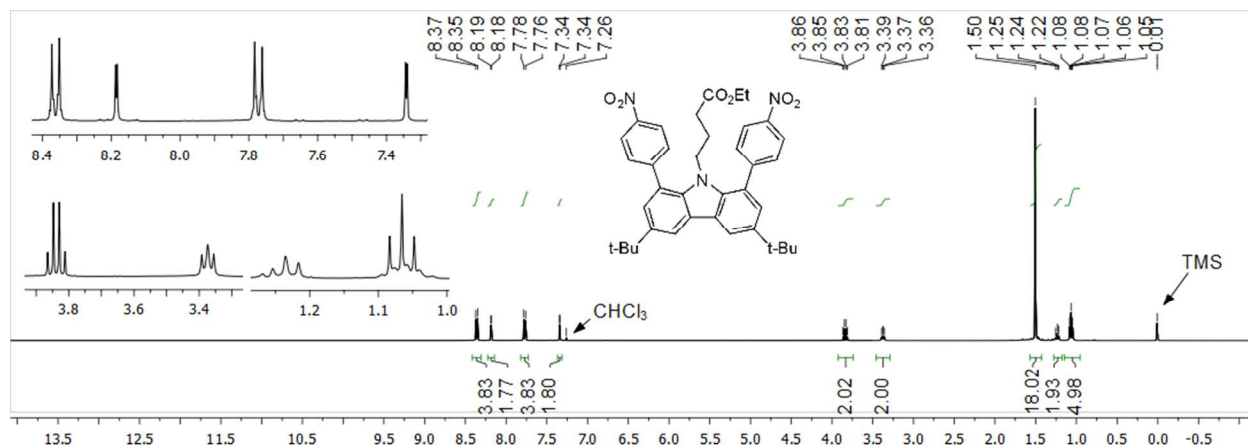


Figure S40. ^1H NMR spectrum of ethyl 4-(3,6-di-*tert*-butyl-1,8-bis(4-nitrophenyl)-9*H*-carbazol-9-yl)butanoate (**3a**).

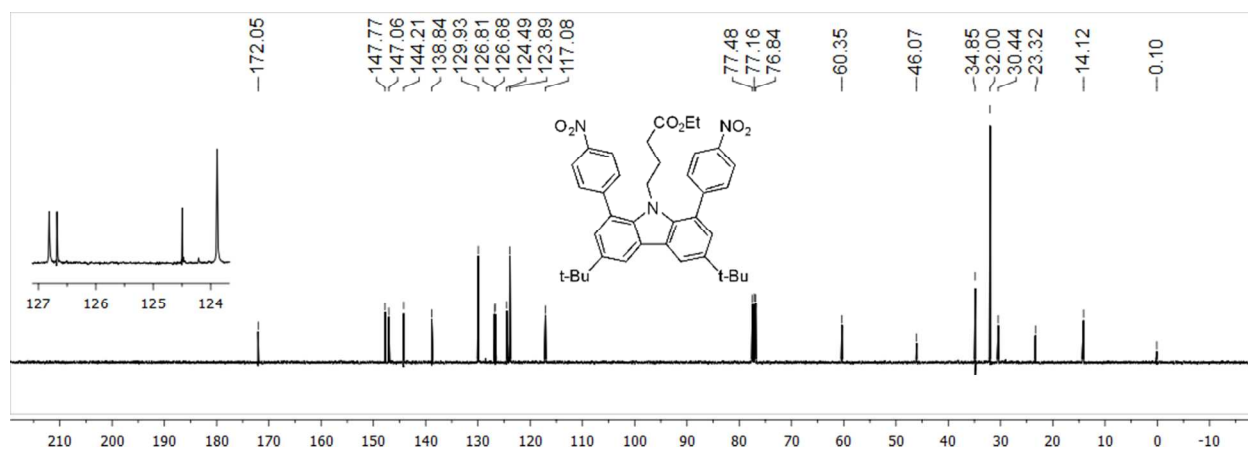


Figure S41. $^{13}\text{C}\{^1\text{H}\}$ NMR spectrum of ethyl 4-(3,6-di-*tert*-butyl-1,8-bis(4-nitrophenyl)-9*H*-carbazol-9-yl)butanoate (**3a**).

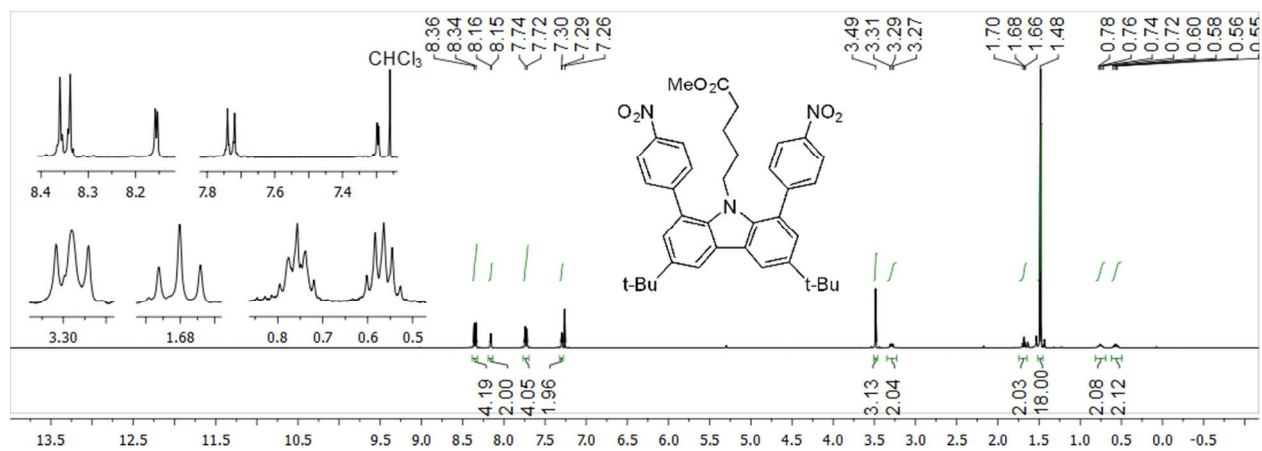


Figure S42. ^1H NMR spectrum of methyl 5-(3,6-di-*tert*-butyl-1,8-bis(4-nitrophenyl)-9*H*-carbazol-9-yl)pentanoate (**3b**).

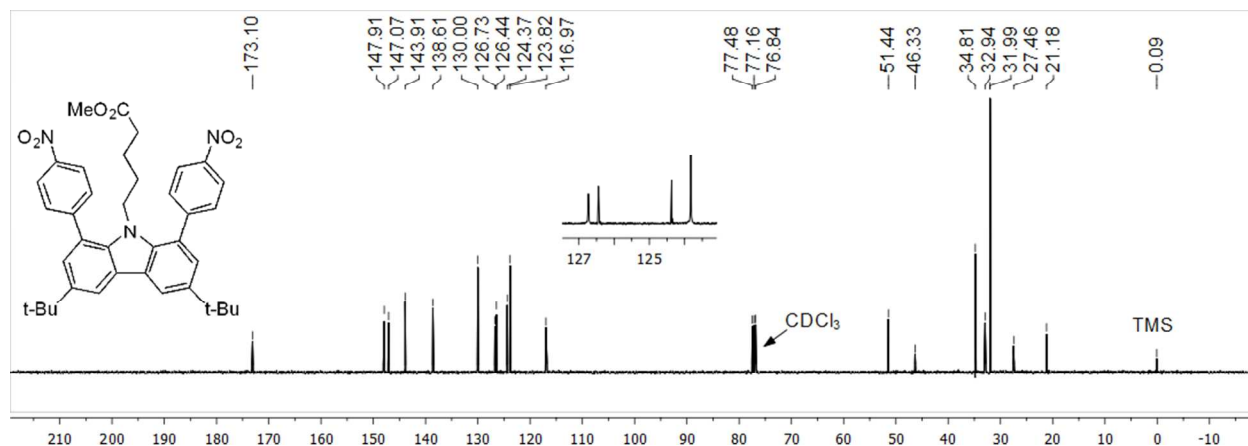


Figure S43. $^{13}\text{C}\{^1\text{H}\}$ NMR spectrum of methyl 5-(3,6-di-*tert*-butyl-1,8-bis(4-nitrophenyl)-9*H*-carbazol-9-yl)pentanoate (**3b**).

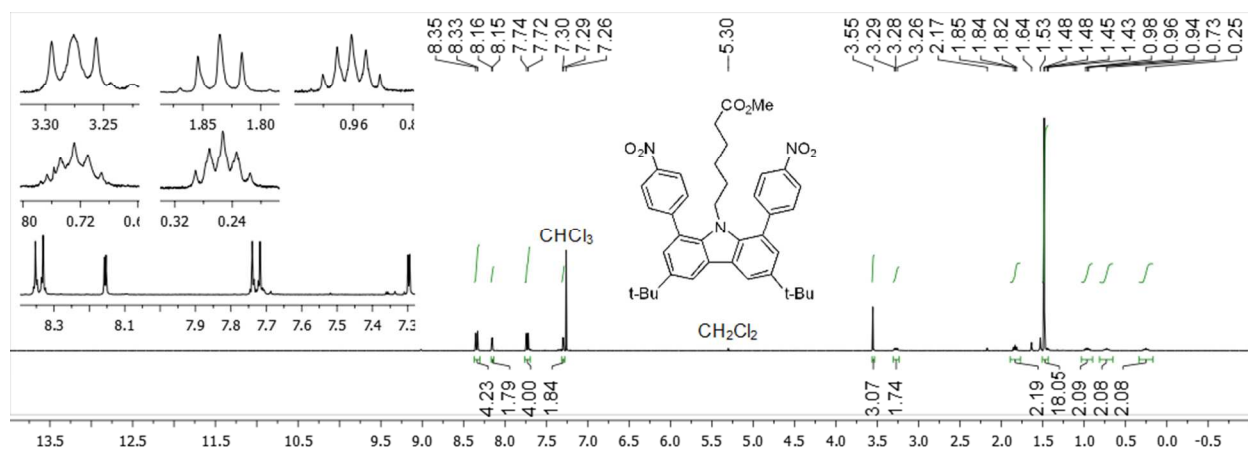


Figure S44. ^1H NMR spectrum of methyl 5-(3,6-di-*tert*-butyl-1,8-bis(4-nitrophenyl)-9*H*-carbazol-9-yl)pentanoate (**3c**).

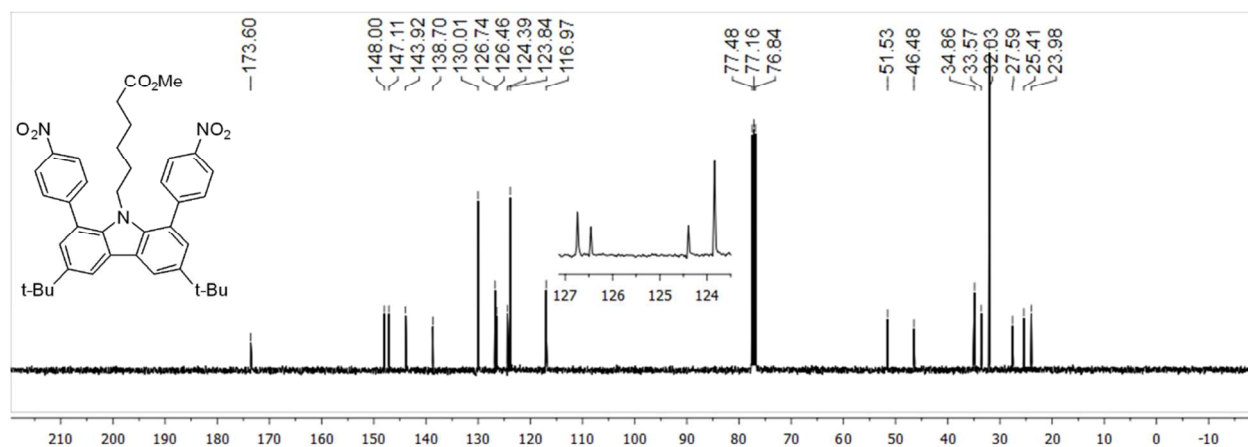


Figure S45. $^{13}\text{C}\{^1\text{H}\}$ NMR spectrum of methyl 6-(3,6-di-*tert*-butyl-1,8-bis(4-nitrophenyl)-9*H*-carbazol-9-yl)hexanoate (**3c**).

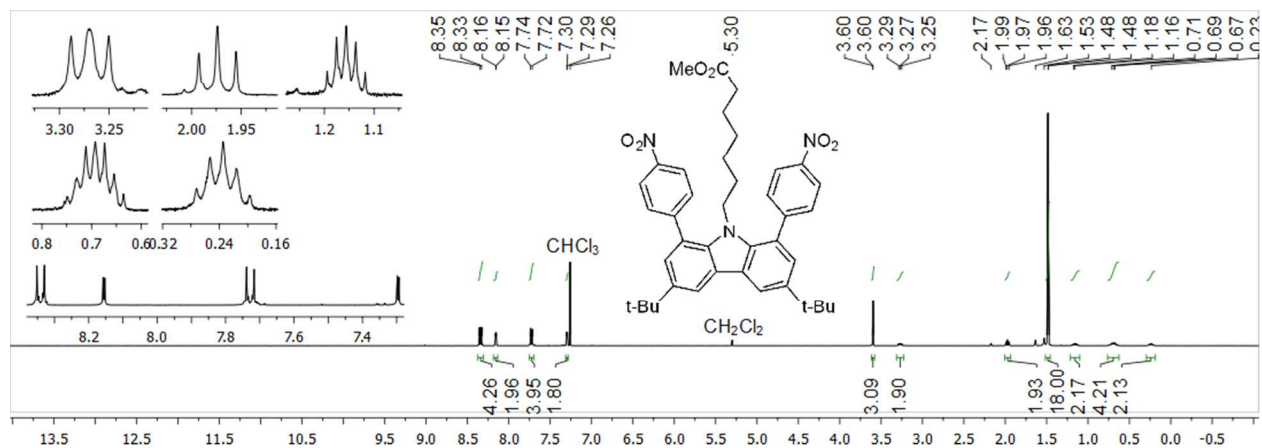


Figure S46. ^1H NMR spectrum of methyl 7-(3,6-di-*tert*-butyl-1,8-bis(4-nitrophenyl)-9*H*-carbazol-9-yl)heptanoate (**3d**).

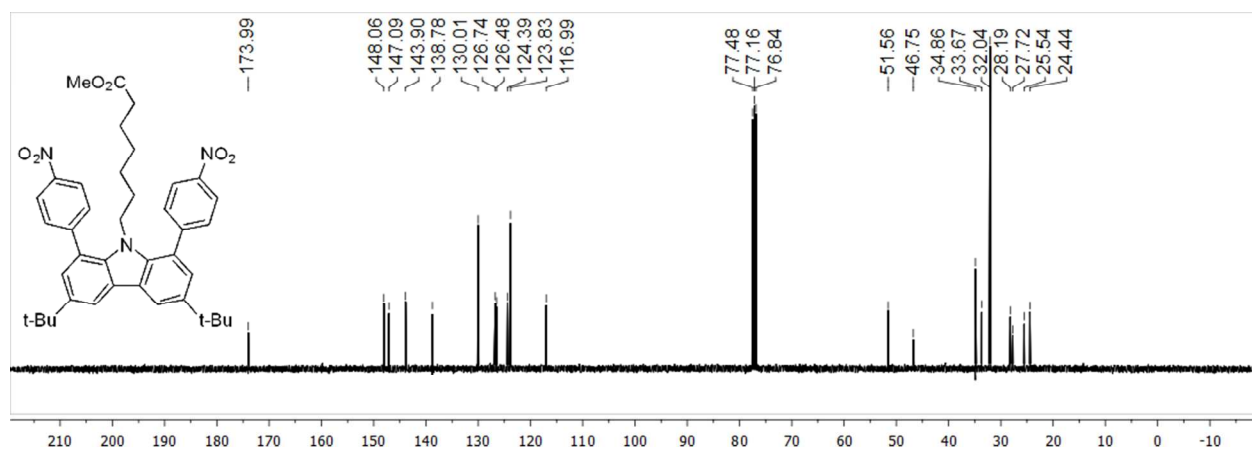


Figure S47. $^{13}\text{C}\{^1\text{H}\}$ NMR spectrum of methyl 7-(3,6-di-*tert*-butyl-1,8-bis(4-nitrophenyl)-9*H*-carbazol-9-yl)heptanoate (**3d**).

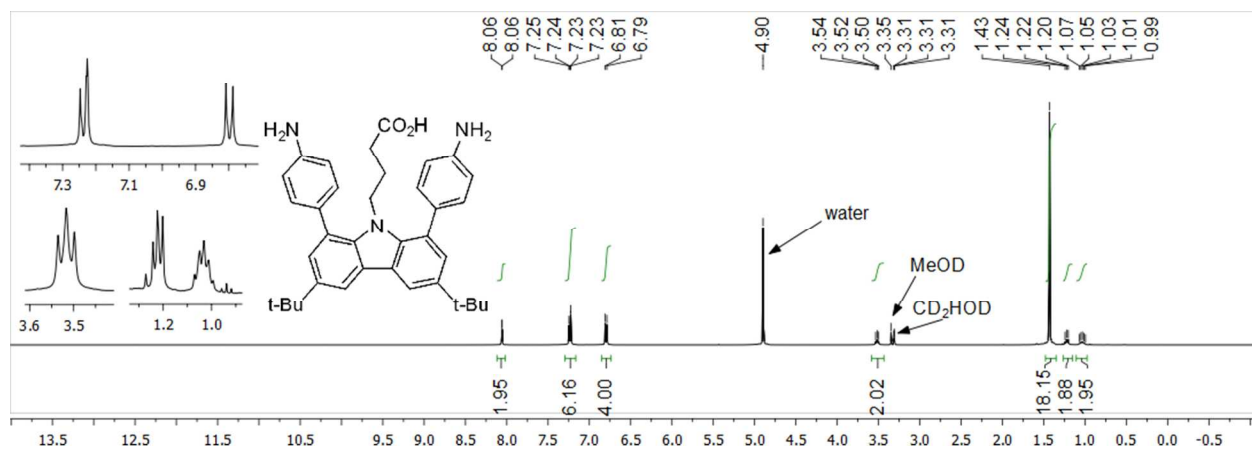


Figure S48. ^1H NMR spectrum of 4-(1,8-bis(4-aminophenyl)-3,6-di-*tert*-butyl-9*H*-carbazol-9-yl)butanoic acid (**4a**).

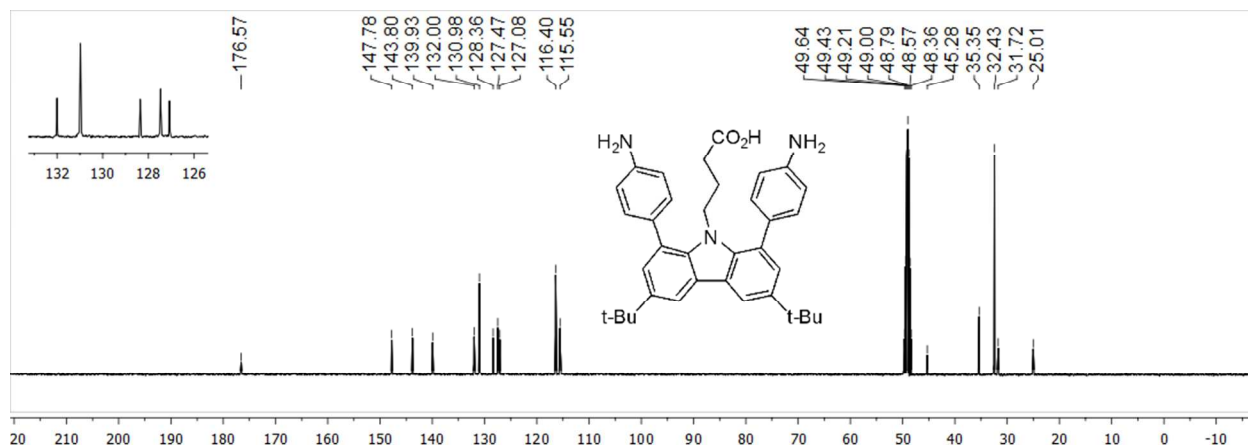


Figure S49. ¹³C{¹H} NMR spectrum of 4-(1,8-bis(4-aminophenyl)-3,6-di-*tert*-butyl-9*H*-carbazol-9-yl)butanoic acid (**4a**).

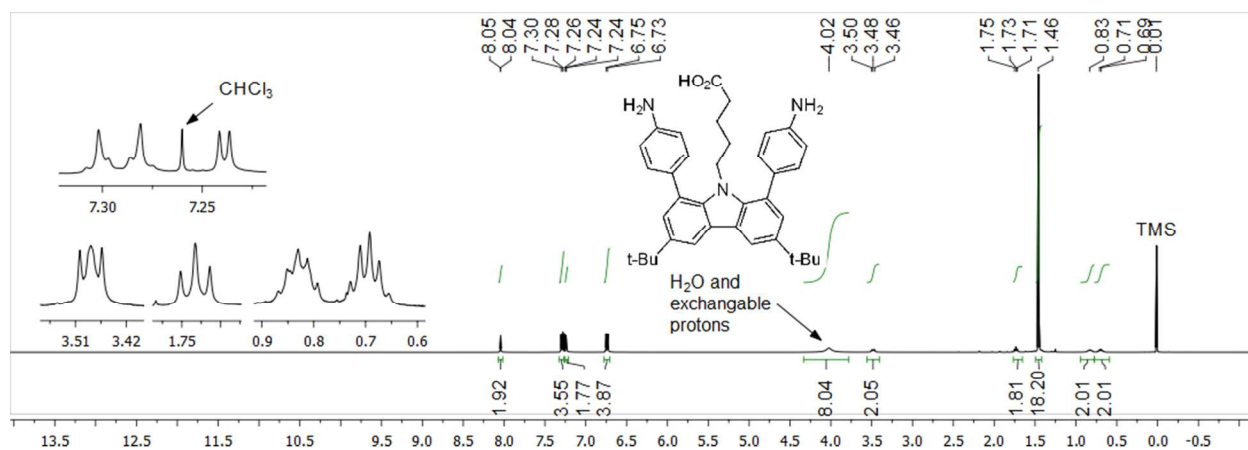


Figure S50. ¹H NMR spectrum of 5-(1,8-bis(4-aminophenyl)-3,6-di-*tert*-butyl-9*H*-carbazol-9-yl)pentanoic acid (**4b**).

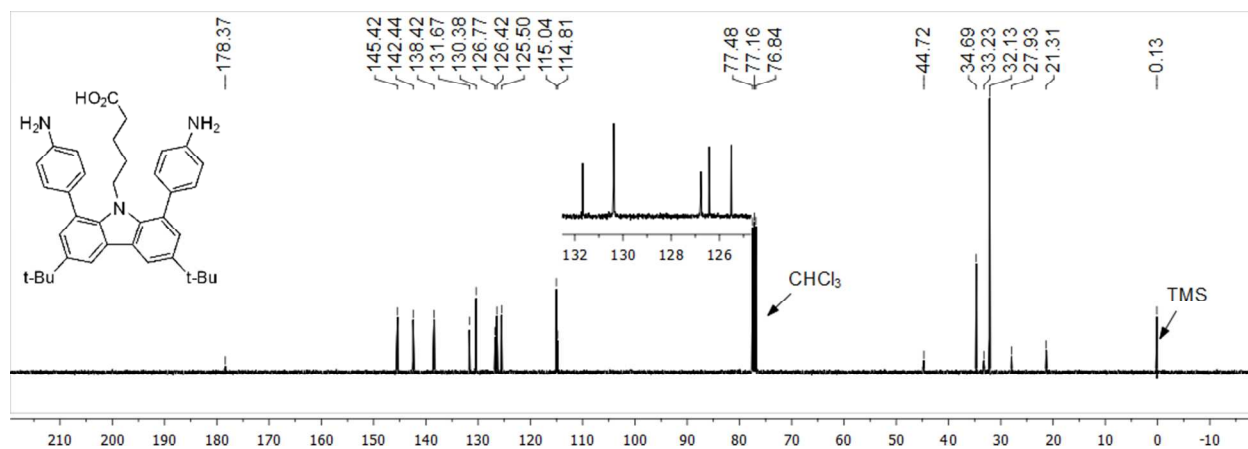


Figure S51. ¹³C{¹H} NMR spectrum of 5-(1,8-bis(4-aminophenyl)-3,6-di-*tert*-butyl-9*H*-carbazol-9-yl)pentanoic acid (**4b**).

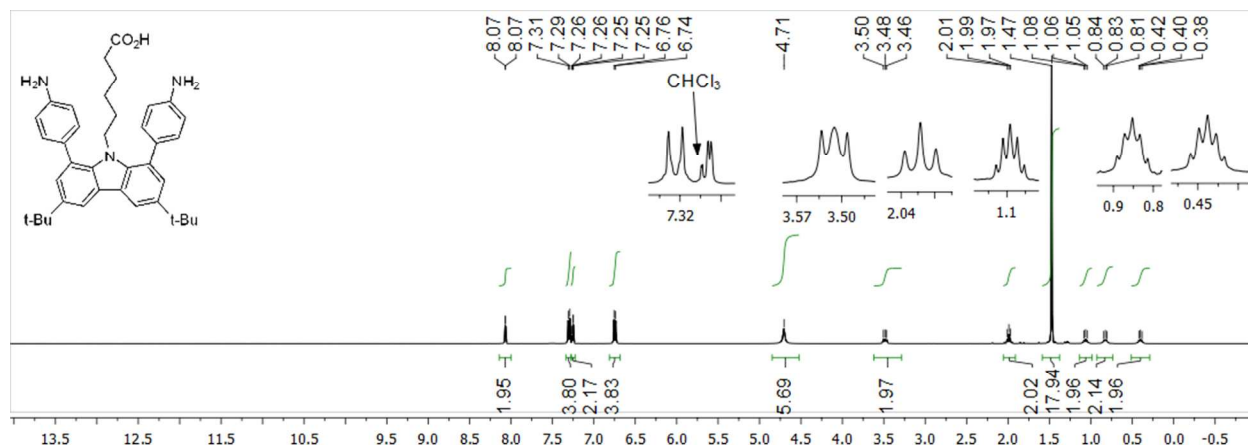


Figure S52. ^1H NMR spectrum of 6-(1,8-bis(4-aminophenyl)-3,6-di-*tert*-butyl-9*H*-carbazol-9-yl)hexanoic acid (**4c**).

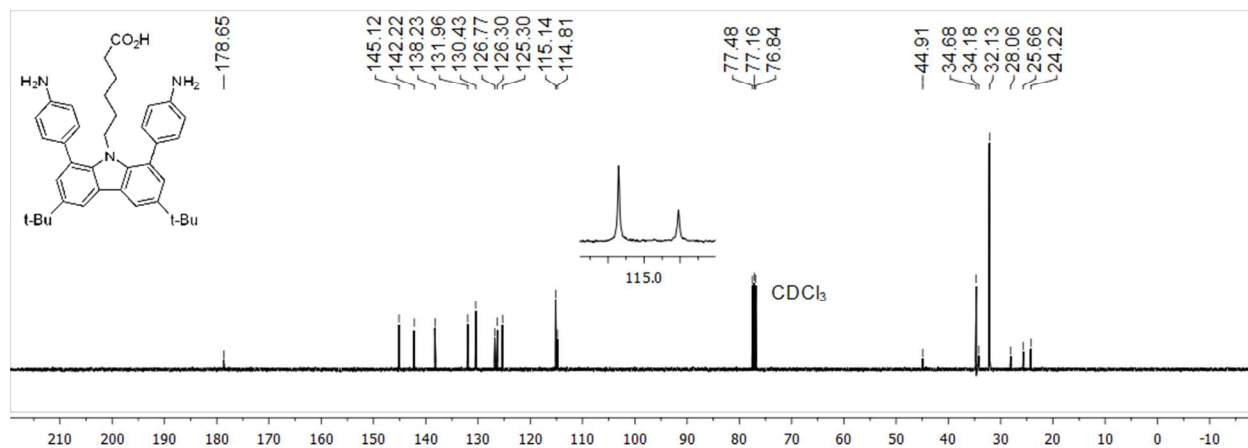


Figure S53. $^{13}\text{C}\{^1\text{H}\}$ NMR spectrum of 6-(1,8-bis(4-aminophenyl)-3,6-di-*tert*-butyl-9*H*-carbazol-9-yl)hexanoic acid (**4c**).

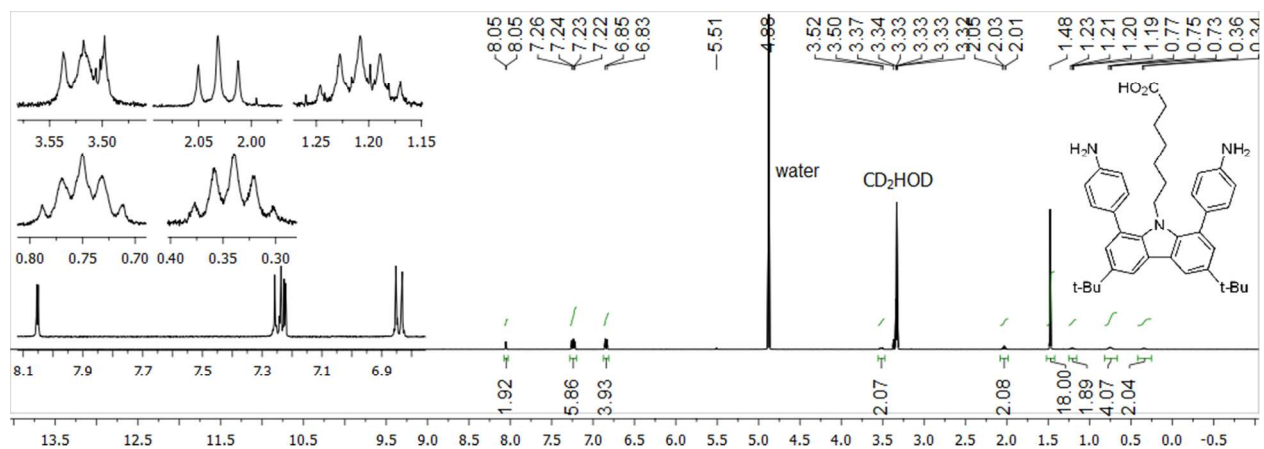


Figure S54. ^1H NMR spectrum of 7-(1,8-bis(4-aminophenyl)-3,6-di-*tert*-butyl-9*H*-carbazol-9-yl)heptanoic acid (**4d**).

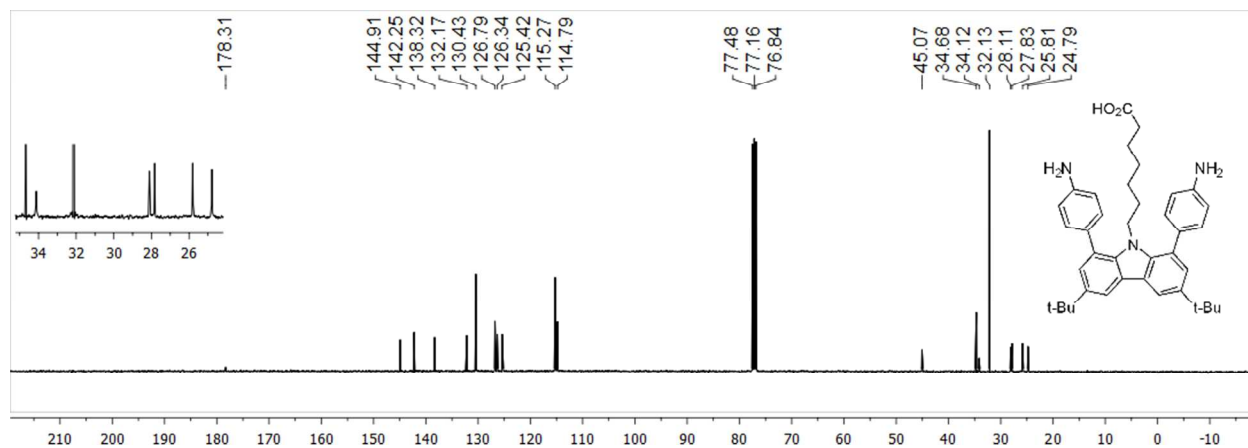


Figure S55. $^{13}\text{C}\{^1\text{H}\}$ NMR spectrum of 7-(1,8-bis(4-aminophenyl)-3,6-di-*tert*-butyl-9H-carbazol-9-yl)heptanoic acid (**4d**).

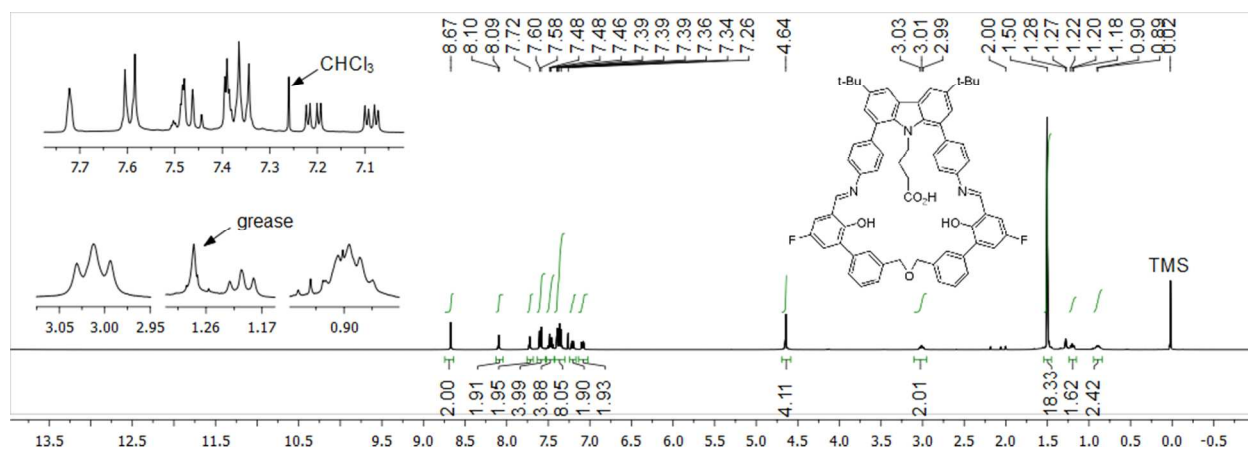


Figure S56. ^1H NMR spectrum of H₃PIMIC3.

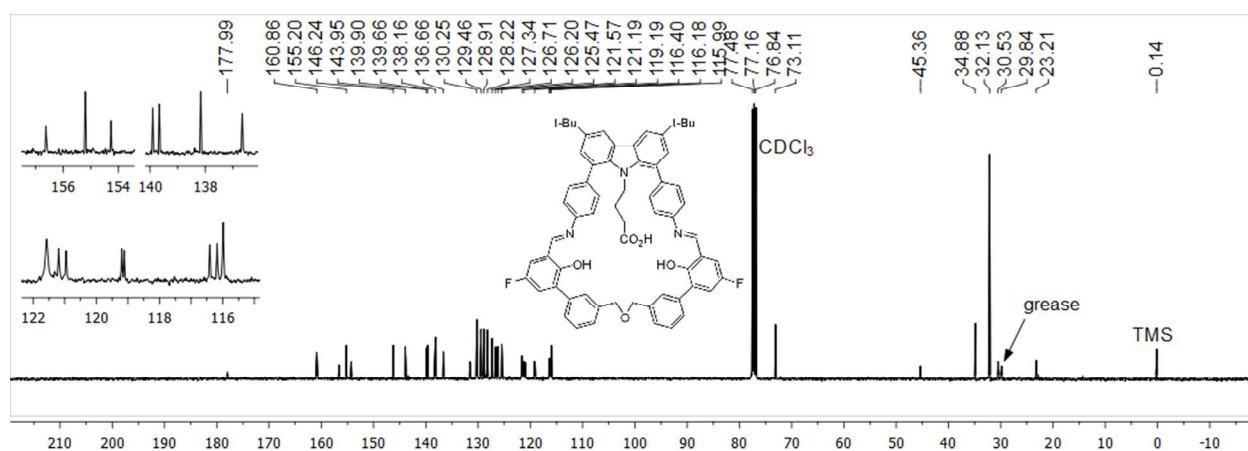


Figure S57. $^{13}\text{C}\{^1\text{H}\}$ NMR spectrum of H₃PIMIC3.

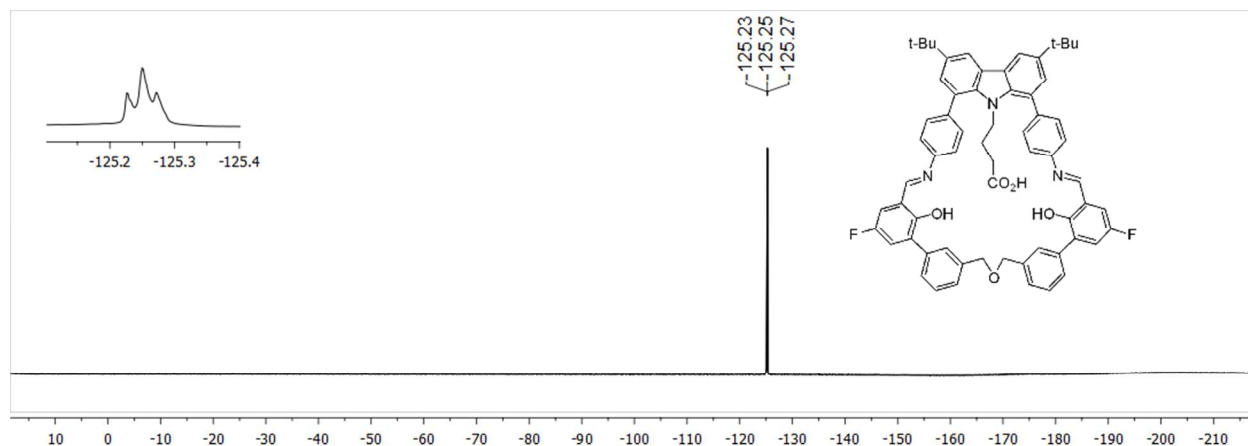


Figure S58. ^{19}F NMR spectrum of $\text{H}_3\text{PIMIC3}$.

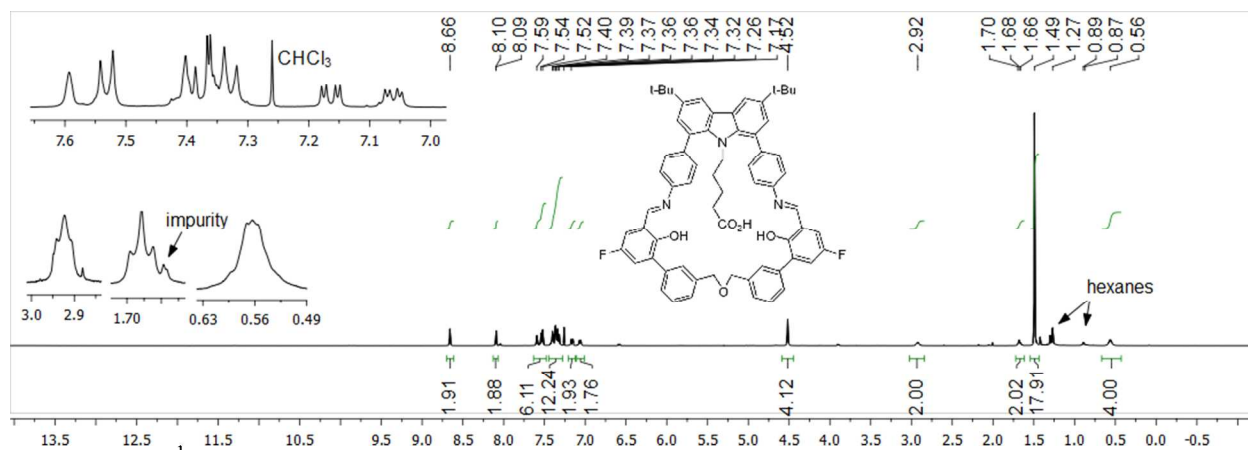


Figure S59. ^1H NMR spectrum of $\text{H}_3\text{PIMIC4}$.

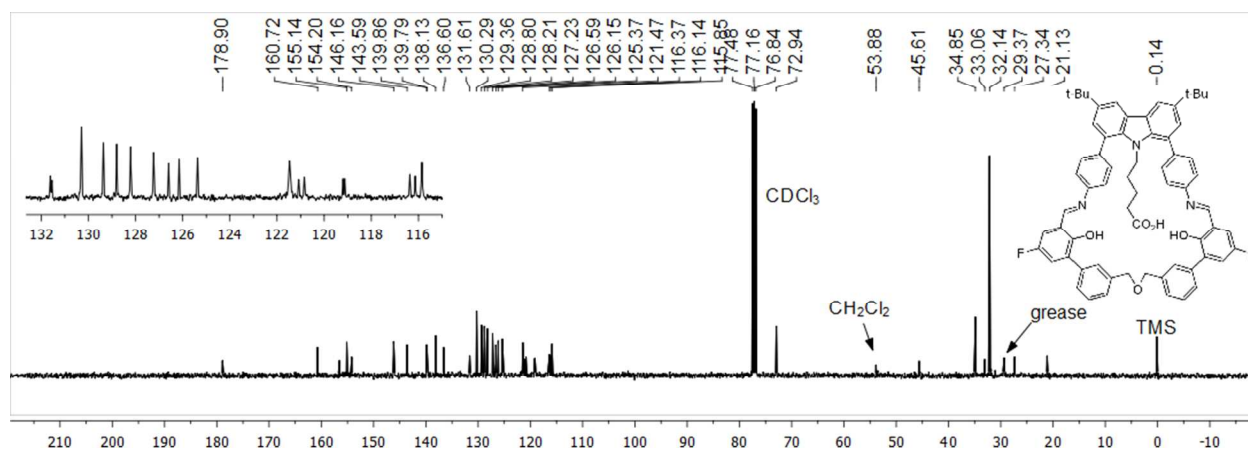


Figure S60. $^{13}\text{C}\{^1\text{H}\}$ NMR spectrum of $\text{H}_3\text{PIMIC4}$.

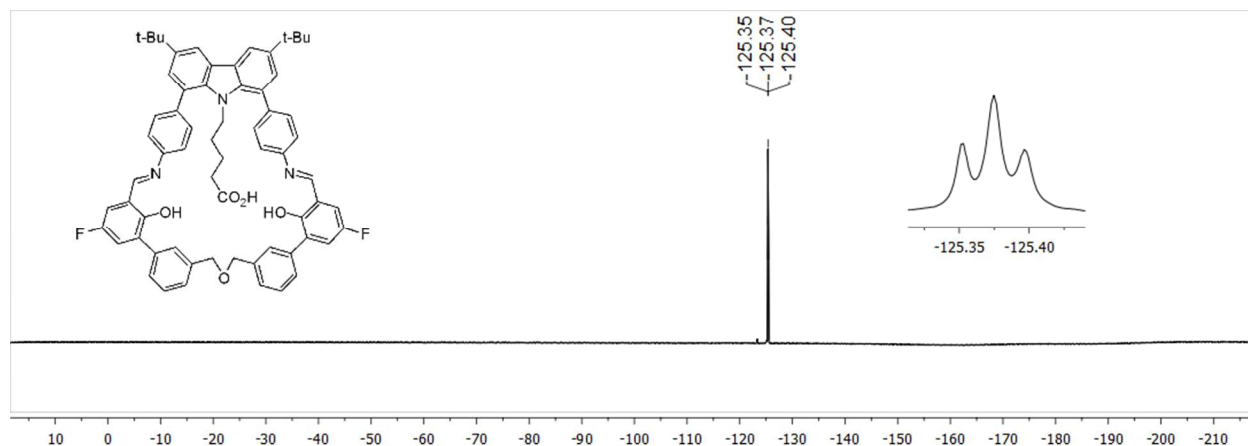


Figure S61. ^{19}F NMR spectrum of $\text{H}_3\text{PIMIC4}$.

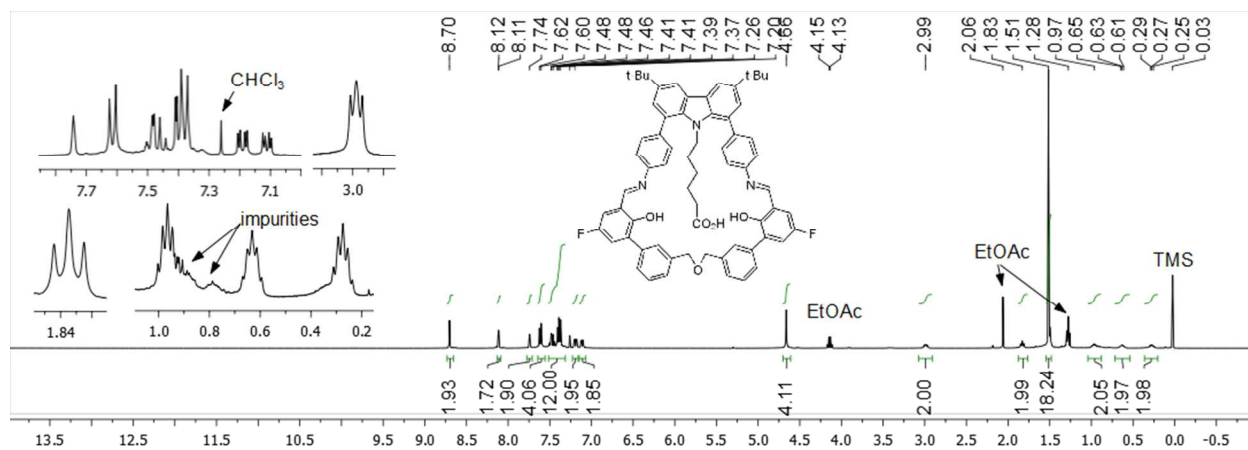


Figure S62. ^1H NMR spectrum of $\text{H}_3\text{PIMIC5}$.

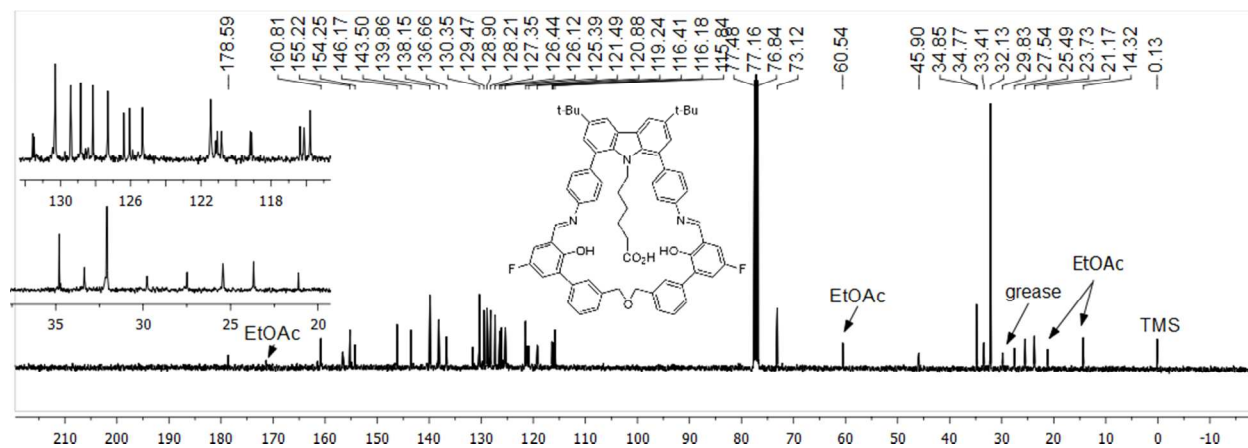


Figure S63. $^{13}\text{C}\{^1\text{H}\}$ NMR spectrum of $\text{H}_3\text{PIMIC5}$.

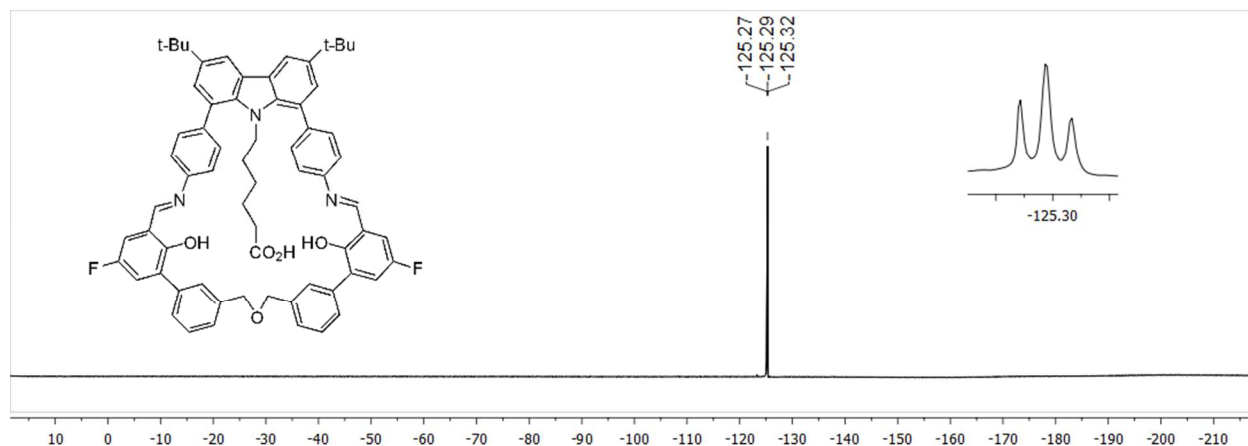


Figure S64. ^{19}F NMR spectrum of $\text{H}_3\text{PIMIC5}$.

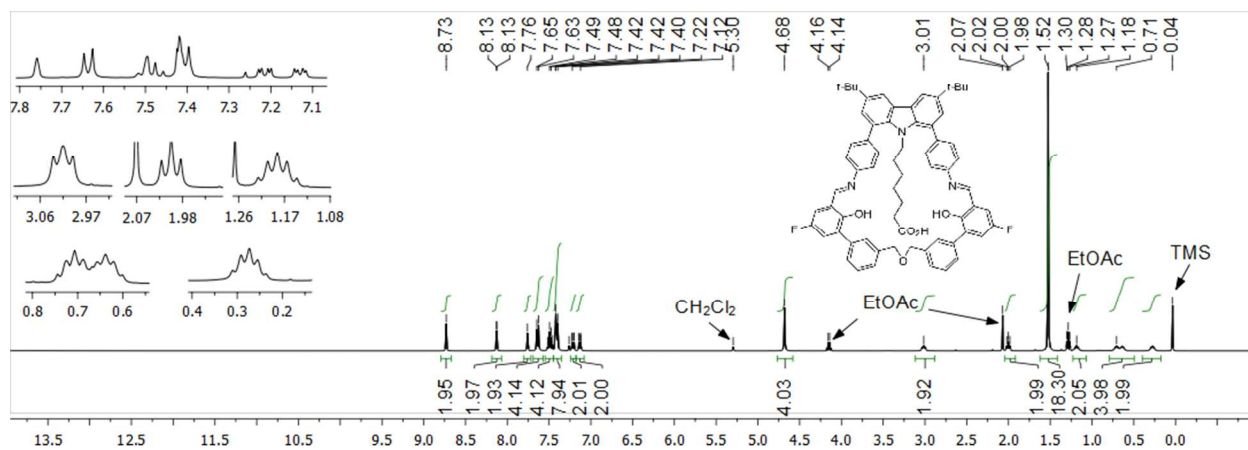


Figure S65. ^1H NMR spectrum of $\text{H}_3\text{PIMIC6}$.

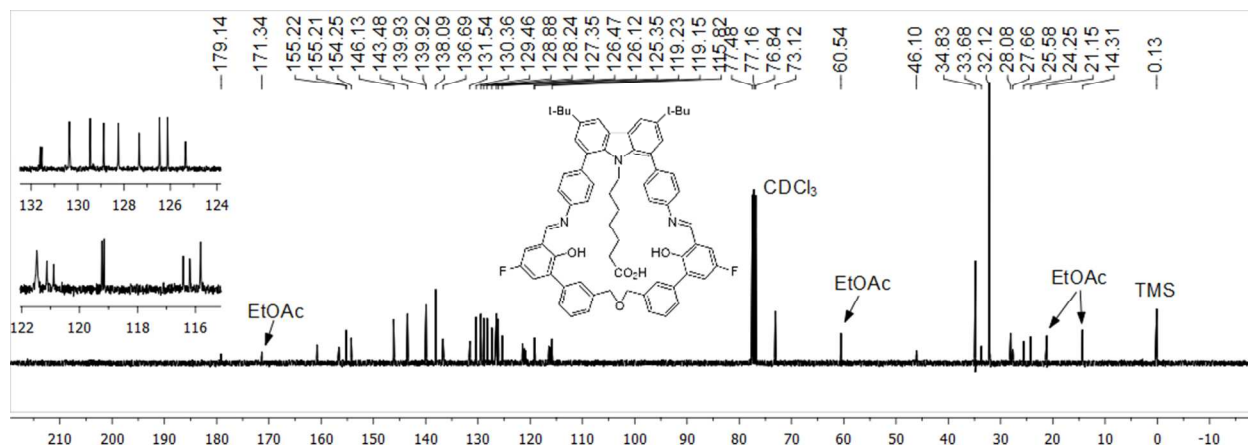


Figure S66. $^{13}\text{C}\{^1\text{H}\}$ NMR spectrum of $\text{H}_3\text{PIMIC6}$.

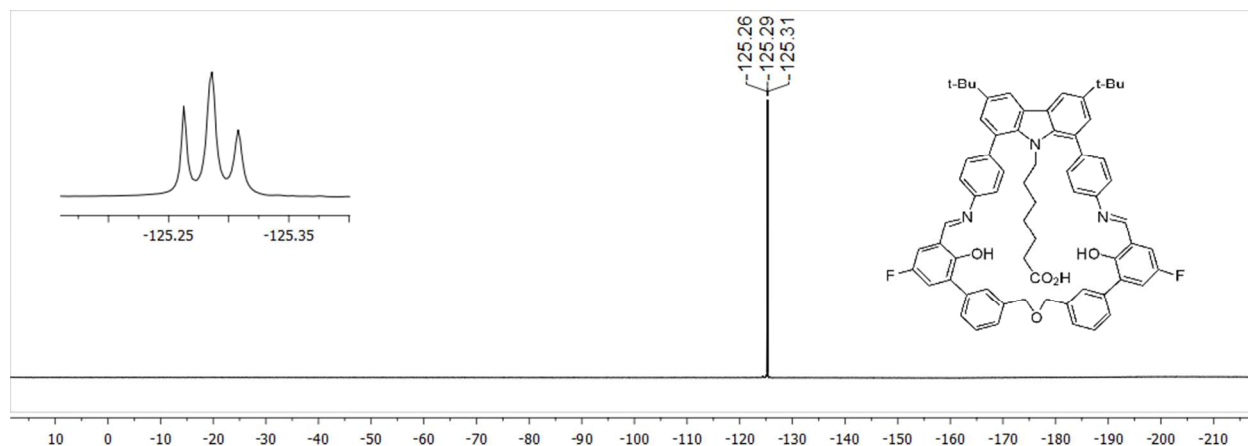


Figure S67. ^{19}F NMR spectrum of $\text{H}_3\text{PIMIC6}$.

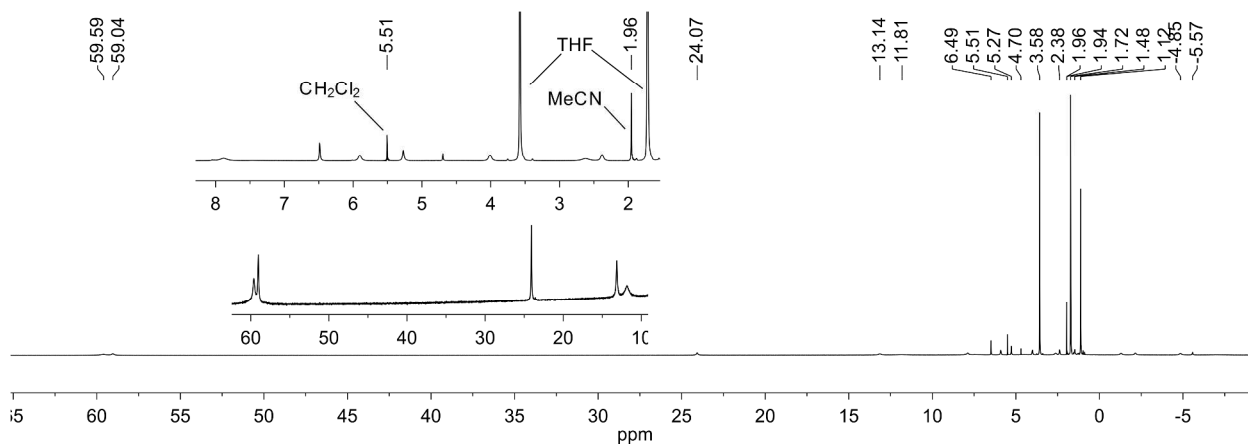


Figure S68. ^1H NMR spectrum of $[\text{Fe}_2(\text{PIMIC4})(\text{AnthCO}_2)(\text{MeCN})]$ (**7**) in $\text{THF-}d_8$. The signal at 5.51 ppm indicates the residual CH_2Cl_2 in the solid of **7**, which was also suggested by elemental analysis.

References

1. Minier, M. A.; Lippard, S. J., ^{19}F NMR Study of Ligand Dynamics in Carboxylate-Bridged Diiron(II) Complexes Supported by a Macrocyclic Ligand. *Dalton Trans.* **2015**, *44*, 18111-18121.
2. DeZutter, C. B.; Horner, J. H.; Newcomb, M., Rate Constants for 1,5- and 1,6-Hydrogen Atom Transfer Reactions of Mono-, Di-, and Tri-aryl-substituted Donors, Models for Hydrogen Atom Transfers in Polyunsaturated Fatty Acid Radicals. *J. Phys. Chem. A* **2008**, *112*, 1891-1896.
3. Lin, S.; Song, C.-X.; Cai, G.-X.; Wang, W.-H.; Shi, Z.-J., Intra/Intermolecular Direct Allylic Alkylation via Pd(II)-Catalyzed Allylic C–H Activation. *J. Am. Chem. Soc.* **2008**, *130*, 12901-12903.
4. Klose, A.; Solari, E.; Floriani, C.; Chiesi-Villa, A.; Rizzoli, C.; Re, N., Magnetic Properties Diagnostic for the Existence of Iron(II)-Iron(II) Bonds in Dinuclear Complexes Which Derive from Stepwise Insertion Reactions on Unsupported Iron–Aryl Bonds. *J. Am. Chem. Soc.* **1994**, *116*, 9123-9135.
5. Wang, X.; Zhao, L.; Shao, S.; Ding, J.; Wang, L.; Jing, X.; Wang, F., Poly(spirobifluorene)s Containing Nonconjugated Diphenylsulfone Moiety: Toward Blue Emission Through a Weak Charge Transfer Effect. *Macromolecules* **2014**, *47*, 2907-2914.
6. Liu, S.; Pestano, J. P. C.; Wolf, C., Regioselective Copper-Catalyzed C-N and C-S Bond Formation Using Amines, Thiols and Halobenzoic Acids. *Synthesis* **2007**, *2007*, 3519-3527.
7. Foster, T. L.; Caradonna, J. P., Fe^{2+} -Catalyzed Heterolytic RO–OH Bond Cleavage and Substrate Oxidation: A Functional Synthetic Non-Heme Iron Monooxygenase System. *J. Am. Chem. Soc.* **2003**, *125*, 3678-3679.
8. Rowe, G. T.; Rybak-Akimova, E. V.; Caradonna, J. P., Heterolytic Cleavage of Peroxide by a Diferrous Compound Generates Metal-Based Intermediates Identical to Those Observed with Reactions Utilizing Oxygen-Atom-Donor Molecules. *Chem. Eur. J.* **2008**, *14*, 8303-8311.
9. McGarrigle, E. M.; Murphy, D. M.; Gilheany, D. G., Ligand Tuning in the Chromium–Salen-Mediated Asymmetric Epoxidation of Alkenes. *Tetrahedron: Asymmetry* **2004**, *15*, 1343-1354.
10. *APEX2 v.4.0*, Bruker AXS, Inc.: Madison, WI, 2008.
11. *SAINTE: SAX Area-Detector Integration Program*, University of Göttingen: Göttingen, Germany, 2008.
12. Sheldrick, G. M. *SADABS: Area-Detector Absorption Correction*, University of Göttingen: Göttingen, Germany, 2008.
13. *XPREP 2nd Ed.*, Bruker AXS, Inc.: Madison, WI, 2008.
14. Sheldrick, G. M., SHELXT - Integrated Space-Group and Crystal-Structure Determination. *Acta Cryst. A* **2015**, *71*, 3-8.
15. Sheldrick, G., Crystal Structure Refinement with SHELXL. *Acta Cryst. C* **2015**, *71*, 3-8.
16. Spek, A. L. *PLATON: A Multipurpose Crystallographic Tool*, University of Utrecht: Utrecht, The Netherlands, 2008.
17. Kratzert, D.; Holstein, J. J.; Krossing, I., DSR: Enhanced Modelling and Refinement of Disordered Structures with SHELXL. *J. Appl. Cryst.* **2015**, *48*, 933-938.

18. Green, K., Improved Metalation of 2,4,6-Tribromoanisole: Synthesis of 2-Methoxyresorcinol. *J. Org. Chem.* **1991**, *56*, 4325-4326.
19. Macrae, C. F.; Edgington, P. R.; McCabe, P.; Pidcock, E.; Shields, G. P.; Taylor, R.; Towler, M.; van de Streek, J., Mercury: Visualization and Analysis of Crystal Structures. *J. Appl. Cryst.* **2006**, *39*, 453-457.
20. Sheldrick, G. M. *CELL NOW*, 2008/2; Bruker: 2008.
21. Do, L. H.; Lippard, S. J., Toward Functional Carboxylate-Bridged Diiron Protein Mimics: Achieving Structural Stability and Conformational Flexibility Using a Macrocyclic Ligand Framework. *J. Am. Chem. Soc.* **2011**, *133*, 10568-10581.
22. Thorp, H. H., Bond Valence Sum Analysis of Metal-Ligand Bond Lengths in Metalloenzymes and Model Complexes. *Inorg. Chem.* **1992**, *31*, 1585-1588.